ABSTRACT

ROLLINS, CHAD ERIC. Development of Multiphase Computational Fluid Dynamics Solver in OpenFOAM. (Under the direction of Hong Luo.)

From the viewpoint of an increase in energy demand, a shortage of fossil fuels and changes in the climate on the global scale, nuclear power has the ability to represent a part of the solution to the energy and environmental problems we are facing currently. However, there are still problems that need solutions regarding the management of the nuclear waste, public opinion of nuclear power and public safety surrounding nuclear power plants during accidents (as proved via the fairly recent Fukushima accident). The interest in improving the safety and reliability of nuclear power plants through researching and developing advancements to nuclear energy production is strong and still ongoing. In this context, the basic motivation for this work is based on the need to evaluate and improve the current strategies for CFD modeling of two-phase Eulerian flows in boiling channels. The modeling of these types of problems presents several challenges. The major challenge lies in the presence of the many closure models that are all tightly non-linearly coupled in the solution process. Other challenges are that many of the closure models are empirically determined using relatively small sets of flow conditions; thus, the sensitivity & accuracy of these closure models in the wide range of flow conditions that need to be modeled for a general multiphase CFD solver. Also, there is a distinct lack of detailed experimental results for quantities of interest at the operating conditions of a interest (i.e. high pressure boiling cases).

With these motivation and challenges in mind, the main objectives were to develop an existing CFD solver with phase change capabilities into a modular testing platform to potentially aid in identification and development of remedies for the numerical / modeling issues by allowing the testing of different numerical methods and then to validate both the functionality of the platform and of the underlying numerical methods within the solver against a wide range of numerical test cases. The main objectives aimed at setting up the testing platform to have the ability to address the various numerical and modeling issues, as well as, validating some of the base functionality of the solver through academic test problems, existing experiments and comparisons with commercial CFD software (e.g. Star-CCM+). The setup of the main objectives are to not only address and test the performance and stability of a particular method with our platform, but also, due to the use

of open-source code, have the added benefit of being able to include sensitivity analysis and uncertainty quantification techniques on quantities of interest in the simulation. The relevance of these first steps in the development, in terms of usage for accident scenarios for PWRâĂŹs which requires modeling the critical heat flux mechanism of departure from nucleate boiling, of the testing platform is that it gives users the ability to test all the closure and algorithm methods for stability and accuracy in a structured and efficient manner before the extreme case of DNB.

The finalized design of the modular testing platform and the user-definable functionality was completed during the course of this work. The design of the testing platform allowed the easy addition & testing of various closure models / numerical methods and the preliminary validation cases allowed the addressing & implementation of some improvements in the overall solution approach. The comparison of results with the commercial CFD package Star-CCM+ displayed favorable performance in academic & adiabatic bubbly flow problems with our solver; however, more study is required for boiling flow problems as the added complexity yields a large number of sources for the potential deviation of results & poor overall performance. A more in-depth study with the use of uncertainty quantification & sensitivity analysis tools, that are currently being developed, is necessary to track down the reasoning behind some of the observed behavior with the current solver methods and potentially further improve the overall solution method.

Development of Multiphase Computational Fluid Dynamics Solver in OpenFOAM

by
Chad Eric Rollins

A dissertation submitted to the Graduate Faculty of
North Carolina State University
in partial fulfillment of the
requirements for the Degree of
Doctor of Philosophy

Mechanical Engineering

Raleigh, North Carolina

2018

APPROVED BY:

Jack Edwards	Nam Dinh
Igor Bolotnov	Hong Luo Chair of Advisory Committee

DEDICATION

I would like to dedicate this work to my family because without your support this would not have been possible.

BIOGRAPHY

The author grew up in a small town in New Hampshire and attended Roger Williams University in Bristol, RI for college. He graduated valedictorian with a B.S. in engineering with a focus in Mechanical Engineering and a minor in Mathematics in 2008. He then went to work for Rist-Frost & Shumway P.C. in Laconia, NH after graduation and until he decided to return to school in late 2009. He started graduate school by attending North Carolina State University in Raleigh, NC where he worked under Dr. Joseph Micheal Doster until he graduated from the Nuclear Engineering program with a Masters degree in 2014. He then moved to the Mechanical & Aerospace Engineering program at North Carolina State University under Dr. Hong Luo for his studies towards his doctorate. His research interests include thermal hydraulics, computation fluid dynamics and applied mathematics.

ACKNOWLEDGEMENTS

Firstly, I would like to express my sincere gratitude to my advisor Prof. Hong Luo for the continuous support of my Ph.D study and related research, for his patience, motivation, and immense knowledge. His guidance helped me in all the time of research and writing of this thesis. I could not have imagined having a better advisor and mentor for my Ph.D study. Besides my advisor, I would like to thank the rest of my thesis committee: Prof. Jack Edwards, Prof. Nam Dinh, and Prof. Igor Bolotnov, for their insightful comments, encouragement, and their first class teaching that helped me progress in my research. I thank my fellow labmates in for the stimulating discussions, for the sleepless nights we were working together before deadlines, and for all the fun we have had in the last four years. Last but not the least, I would like to thank my family and friends for supporting me throughout writing this thesis and in my life in general.

TABLE OF CONTENTS

LIST OF TABLES

LIST OF FIGURES

Chapter 1

INTRODUCTION

1.1 Background

From the viewpoint of an increase in energy demands, a shortage of fossil fuels and changes in the climate on the global scale, nuclear power has the ablility to represent a part of the solution to the energy and environmental problems that we are facing currently. Some of the advantages of nuclear power are,

- Lack of greenhouse gas emissions into the atmosphere that contribute to the climate change.
- Low cost per kWh of electricity production.
- Small power plants (relatively) produce large amounts of electricity due to the high energy density of the nuclear fuel.
- Is a very mature and reliable technology (thousands of cumulative nuclear reactor years of comericial operation across dozens of countries in the world) in comparison to renewable energy sources that lack a consistancy of supply and also, in order to be used on a larger scale, require further developments and research.

Of course, the advantages are very convincing but nuclear power is not all sunshine and rainbows. There are still problems that need solutions regarding the management of the nuclear waste, public opinion of nuclear power and public safety surrounding nuclear power plants during accidents (as proved via the fairly recent Fukushima accident). The interest in improving the safety and reliability of nuclear power plants through reseraching

and developing advancements to nuclear energy production is strong and still ongoing. In this context, this thesis deals with the development and validation of an in-house two-phase computational fluid dynamics (CFD) solver with phase change capabilities (e.g. subcooled boiling) in OpenFoam.

1.2 Subcooled Boiling

Subcooled boiling refers to the evaporation of liquid at the heated walls while the bulk of the liquid is still at subcooled temperatures (e.g. the liquid temperature is below saturation conditions). The interest in studying and getting a better understanding of this phenomena in the nuclear industry lies in the fact that the water in a Light Water Reactor (LWR) enters the core subcooled (e.g. less than the saturation temperature) and the first stage in the boiling process is then subcooled boiling, as shown in Fig. 1.1. Hence the reason why the determination of the parameters in subcooled boiling (such as void fraction, bubble diameter, liquid and vapor velocity, wall temperature, etc.) with computational codes is important. It is also important in the perspective of improving the coupling of neutronic & thermo-hydraulic analysis and to determine the distribution and deposition of impurities along the axis of the core. Also, the study and development of computational codes for adiabatic and diabatic two-phase flows are of interest for many other industrial applications in the chemical, aerospace and power industry in order safely and optimally design processes involving these types of two-phase flows. As shown in Fig. 1.1 & 1.2, the heat transfer and boiling process in a vertical pipe with flow moving upward against gravity (or analogously in a nuclear reactor sub-channel) can be divided in different regimes. In the section of the vertical pipe when the liquid is subcooled throughout the channel and no boiling occurs, the heat transfer is governed by single-phase forced convection. At a certain point along the pipe, subcooled boiling will start with evaporation of liquid in nucleation sites (or micro-cavities in the material along the heated wall) at the heated walls. The generated bubbles along the wall will grow through continued evaportation; however, at the outside of these bubbles the liquid still may be subcooled; therefore, simulataneously there will be cooling and condensation of the growing bubble that affects its growth rate and then when the bubbles reach a critical size the bubbles will detach from the wall. However, since the bulk of the liquid is still subcooled, the bubbles will condensate in the bulk of the flow away from the wall, heating up the liquid phase and resulting in a high heat transfer

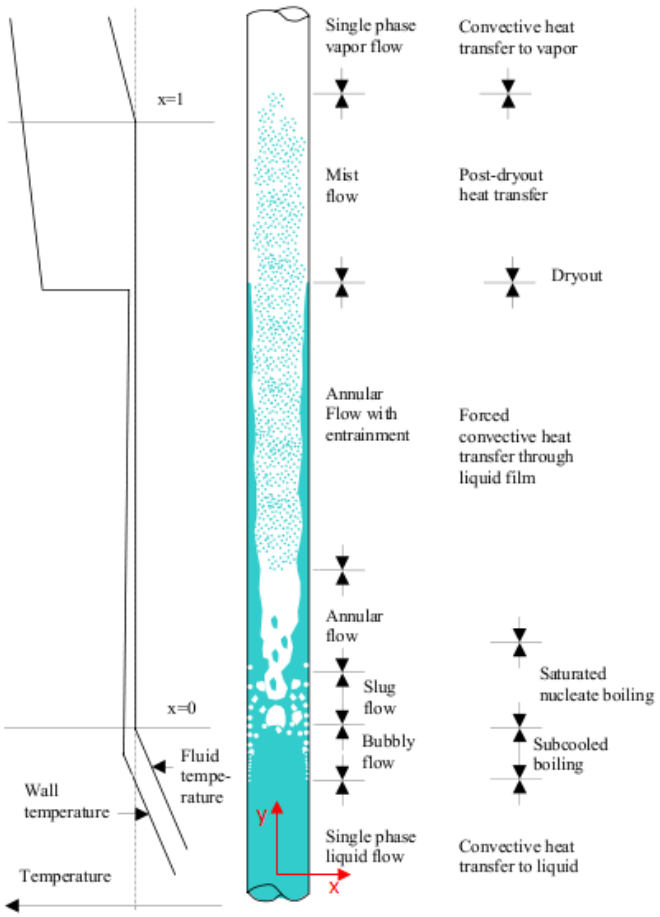

Figure 1.1 Flow patterns and heat transfer regimes in a vertical pipe with upward flow[5, 21, 41]

rate and coefficient. When the bulk of the liquid reaches the saturation temperature, the saturated nucleate boiling regime starts, during which many other different flow patterns can be observed (such as slug, churn and anular flow). Dry-out occurs when the liquid film along the wall of the heated channel during anular flow dissappears due to evaporation. This results in a high increase in wall temperature due to the deterioration of the heat transfer coefficient from the direct contact between the vapor and the heated walls. A different thermal crisis type is the so-called Departure from Nucleate Boiling (DNB) and this can occur with low mass flow rates or large heat fluxes so that the heat flux at the wall is larger than the Critical Heat Flux (CHF). During DNB the boiling mechanism changes from nucleate boiling (very high heat transfer coefficient) to film boiling where a vapor

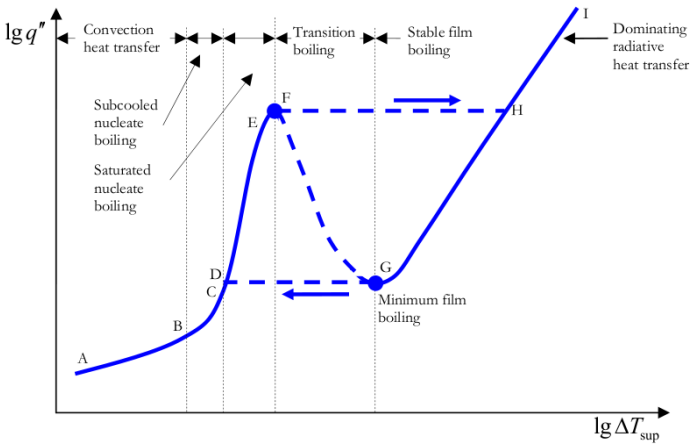

Figure 1.2 Boiling curve - Influence of wall heat flux on wall superheat [5, 21, 41]

layer prevents liquid from reaching the heated walls leading to a sudden decrease of the heat transfer coefficient. The sudden decrease in the heat transfer coefficient causes a massive spike in the wall temperature which can eventually cause fuel rods damage and, in a worst case scenario, it can cause a core melt-down. DNB is a CHF mechanism that occur both in Pressurized Water Reactors (PWR) and in the lower part of Boiling Water Reactors (BWR) during various accidents. Therefore, a clear understanding of two-phase flows, of the boiling mechanisms, and simulating both accurately and efficiently is of huge interest in the nuclear industry.

In fact, a correct modeling of subcooled boiling can be considered as a first step towards better CHF predictions in nuclear reactors during accidents. Furthermore, a more correct understanding and modeling of subcooled boiling can,

- Improve the simulation / prediction of deposition of impurities along the axis of the core that can cause an issue refered to as Axial Offset Anomaly (AOA) in PWR cores.
- Improve the coupled neutronic & thermal-hydraulic calculations because the raidal and axial distribution of void fractions directly influences the reactivity of the core which provides reactivity feedbacks that cannot be neglected.

The AOA in a PWR refers to deviations of the measured flux of neutrons located in the top half of the core from the predicted values. This is due to the presence of enhanced corrosion products and boron deposition on the cladding of the fuel rod surfaces caused

by subcooled boiling [26]. The solver described in this thesis is designed for dealing with both subcooled boiling flows and adiabatic bubbly flows.

1.3 CFD Methodology

In order to predict the parameters in two-phase flows and there multidimensional distributions, a Computational Fluid Dynamics (CFD) methodology is used in this study. The CFD methodology allows one to obtain approximate numerical solutions of fluid flows through discretization. Discretization is replacing the set of coupled differential equations describing the flow by a set of algebraic equations which can be solved by the use of a computer. The CFD methodology became more and more important with the increase of computational power and it now represents an significant engineering tool that allows one to not have to rely on the usage of experimental studies and empirical correlations for modeling fluid flow but, instead substituting them with more generally applicable methods. It is also a much cheaper way of solving some engineering problems. However, CFD models still require to be validated against experimental data before their usage can be defended and this is one of the purposes behind the work of this thesis.

CFD, much like any other numerical methodology, consists of a model (e.g. a mathematical representation of a physical phenomena that typically neglects the less important features to keep it as simple as possible) and a solution procedure in order to obtain an approximate numerical solution from the model. The modeling in CFD starts from the Navier-Stokes equations for fluid flows. These equations are valid for every flow regime (e.g. laminar or turbulent) but they are very difficult to solve numerically, especially for high Reynolds number flows which is one of the areas of interest in this study. Simplifications of the equations and modeling assumptions are required to reduce the complexity of the mathematical model as well as the computational cost of the simulations. If the Navier-Stokes equations are also solved without any manipulation it is by so-called Direct Numerical Simulation (DNS). DNS requires extremely high resolution modeling in order to resolve all the temporal and spatial scales. This is a huge computational effort. This means that the use of DNS is limited to the simulations of low Reynolds number flows and extremely small physical domains for any practical purposes.

Because turbulent flows are of particular interest in this study, the mathematical basis employ conservation equations using mean properties of the flow obtained from a suit-

able averaging procedure of the the microscopic governing equations (e.g. Navier-Stokes equations) that is described more in detail in [49, 64]. This suitable averaging procedure simplifies the complexity of the set of equations by significantly reducing the required computational effort; however, it also introduces additional terms in the averaged equations which require closure laws (e.g. the Reynolds stress in the momentum conservation equation). While the Navier-Stokes equations are well established, the closure laws especially for two-phase flows are not generally applicable to all situations, require further development and are still an object of much debate among scientists. This means that the validation of such models against experimental data is still necessary.

In this work a two-fluid model is used and both phases (continuous and dispersed phase) are modeled with Eulerian conservation equations (e.g. what is refered to as an Euler-Euler model). This means that each phase is treated as a continuum with the use of Reynolds Averaged Navier-Stokes (RANS) equations along with the introduction of the volume phase fractions in the equations. As previously mentioned, the averaging procedure introduces new terms in the momentum equations such as,

- The Reynolds stress which requires a two-phase turbulence model.
- The interfacial momentum transfer term which models the transfer of momentum between the phases (the formulation and modeling of this term needs to be improved since is not well established yet).
- The interfacial diameter term that models the bubble sizes and significantly affects the behavious of the momentum transfer terms.
- The wall heat flux partitioning schemes and the various mechanistic models used to model the volumetric mass and energy source terms.

These closure laws are the weak points of the two-fluid model approach and therefore will be a topic of future study from this work.

1.4 OpenFOAM

OpenFOAM is a free and open-source CFD software package produced by OpenCFD Ltd. The initial development was performed at the Imperial College in London in the 1980's and a commercial version was initially released in 2004. Since 2004, OpenFOAM has been

further developed and the number of users has increased drastically in recent years. This is thought to be due to three main advantages of using OpenFOAM,

- The software is obtained free of charge.
- The software is open-source, which means that the code can easily be modified in order to improve existing solvers as well as be reviewed by peers.
- The software is heavily object-oriented and this object-orientation allows users to introduce new models and solvers (user-selectable) without changing the main source code and independently from the discretization scheme used. This provides awesome flexibility and a simplicity of use.

The programming language is C++ and the software is designed to run on Linux systems. OpenFOAM uses Finite Volume Methodology (FVM) in order to discretize and solve complex fluid dynamics problems. The first step of any CFD discretization is to create a 3-D volume of interest and divide it into small volumes or cells. Thus, obtaining the so-called mesh. After the mesh is created the initial and boundary conditions necessary for solving the conservation equations are defined and applied to the geometry. After, OpenFOAM discretizes the modeled equations using the previously built mesh. In CFD there are three main discretization schems or approaches used,

- Finite Difference Method (FDM) - uses conservation equations in differential form discretized on a mesh that results in a single algebraic equation for each grid node.
- Finite Volume Method (FVM) - divides the domain into small control volumes (CVs) and applys the integral from of the conservation equations to each of the CVs. Considers the center of the CV as the computational node and obtains values at the faces of the CV through various interpolation methods / schemes. Quadrature formulas are used to adequately approximate the volume and surface integrals. This procedure results in the definition of one algebraic equation for each of the CVs. The benefit is that this method is a conservative method by construction which basically means that the obtained solution satisfies the conservation equations if evaluated on the entire problem domain. This is one of the more the commonly used methods in CFD codes.

- Finite Element Method (FEM) - is similar to the Finite Volume Method but test functions are used before integrating the equations and a polynomial representation of the solution is used.

OpenFOAM uses the Finite Volume Method over a collocated grid arrangement. The colocated arrangement means that OpenFOAM stores all dependent variables at the same location which is at the cell center. Also, the same CVs are used for all variables in order to minimize the computational effort. An alternative approach is refered to as a staggered grid arrangement where the different variables can be defined at different points of the grid or in other words on different grids. The collocated arrangement minimizes the computational effort over this arrangement since all variables are stored using the same CV and therefore more CFD codes have typically moved to adopt this arrangement. The arrangement does have difficulties; for example, the difficulties linked to the pressure-velocity coupling and the consequent checker-board instability (e.g. oscillations) in the pressure fields were solved through the Rhie and Chow cure [49]. The structure of OpenFOAM is presented in Fig. 1.3.

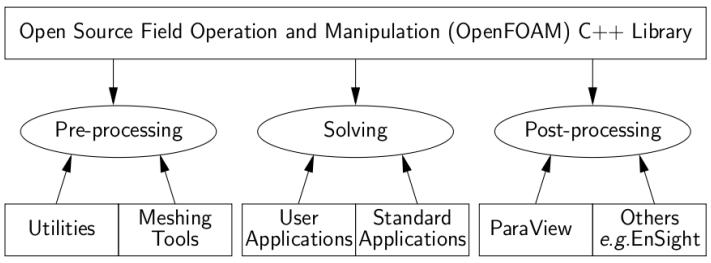

Figure 1.3 OpenFOAM Overall Structure

As with any other CFD software OpenFOAM has three main parts. It has a pre-processing tool where the user can define the mesh, the initial and boundary conditions and the fluid properties. It has a solver where the set of equations is specified and discretized and it has a post-processing tool (which is actually external to OpenFOAM) that is used to visualize and plot the results. OpenFOAM has the sample utility that can be used to obtain a raw set of results in a region of interest, so that they can be easily plotted and compared with experiments.

Another strength of OpenFOAM is the simplicity of adding governing equations to the solvers or a solver which is created by the user, since the equations' syntax in the code is

very similar to the mathematical one. Taking the example given in [21], the equation with the generic unknown x,

$$\frac{\partial x}{\partial t} + \nabla\cdot(\mathbf{U}x) - \nabla\cdot(\nu\nabla x) = 0 \tag{1.1}$$

is implemented in the code as,

```
solve
(
  fvm::ddt(x)
+ fvm::div(U, x)
- fvm::div(nu, div(x))
);
```

More details on OpenFOAM can be found in the User Guide [39] and the Programmers Guide [38]. In the present study, the versions of OpenFOAM that was utilized was OpenFOAM 2.2.x.

1.5 Motivation

The basic motivation for this work is based on the need to evaluate and improve the current strategies for CFD modeling of two-phase Eulerian flows in boiling channels. The modeling of these types of problems present several challenges. The major challenge lies in the presence of the many closure models that are all tightly non-linearly coupled in the solution process. Other challenges are that many of the closure models are empirically determined using relatively small sets of flow conditions; thus, the unreliability of these closure models in the wide range of flow conditions that need to be modeled for a general multiphase CFD solver. Also, there is a distinct lack of detailed experimental results for quantities of interest at the operating conditions of a interest (e.g. high pressure boiling cases).

With the motivation and challenges in mind, the main objectives behind this work were to develop an existing CFD solver with phase change capabilities into a modular testing platform to potentially aid in identification and development of remedies for the numerical / modeling issues by allowing the testing of different numerical methods and to validate functionality with various numerical test cases. This modular testing platform needed to have user-definable functionality, allow a user complete control and access to the source

code, and have the ability to test different numerical methods, discretization schemes, linear solvers, and forms of governing equations.

The second aspect of this work was to validate both the functionality of the platform and of the underlying numerical methods within the solver against a wide range of numerical test cases. This was done in an effort to improve the existing solver methods and create a more consistent numerical treatment for the wide range of validation cases.

In order to accomplish the objectives of my research, access to the source code of what ever CFD software being used was required. This lead to the need for an open-source CFD software program. OpenFOAM was chosen because it is free, has a fairly significant user support base and can be shown to achieve desirable results in comparison to commercial CFD software. It also has the added benefit of its heavily object oriented source code. This allows a relatively fast and general form of implementation of methods and models, without the need for the developer to create different coding for each type of spatial discretization, linear solver, etc. OpenFOAM has some disadvantages. It has a severe lack of documentation due to its open-source nature, different versions OpenFOAM are not backwards compatible, and there is a significant learning curve due to the high level C++ used in the source code of OpenFOAM. For any developer looking to make significant changes to source coding of the solver platform this is also an issue; however, the user-definable functionality of the the solver platform for this work was created in such as way that a basic understanding of C++ object orientation is generally all that is needed.

Chapter 2

GOVERNING EQUATIONS

2.1 Conservation of Mass

The mass conservation equation for a two-field (e.g. continuous & dispersed) two-fluid ($k = 1,2$) model for fluid k is given by

$$\frac{\partial\left(\alpha_k \rho_k\right)}{\partial t} + \nabla\cdot\left(\alpha_k \rho_k \mathbf{U}_k\right) = \Gamma_k \tag{2.1}$$

where Γ_k stands for the mass gained by the fluid k, and

- $k = 1$: dispersed fluid (e.g. steam, air, R12 vapor, etc)
- $k = 2$: continuous fluid (e.g. water, R12 refrigerant, etc)

The reason for not using a four-field two-fluid model is the simplification in the fact that there is no need to track the mass source of density of each field from other fields of the same fluid. α_k stands for the volume fraction of fluid k, ρ_k stands for the density of the fluid k, and $\mathbf{U}_k$ is the velocity vector for fluid k. Eq. 2.1 is for compressible flows and according to [64] can be manipulated, in order to avoid stability issues from large density ratios and to guarantee void fraction boundedness (e.g. always between 0 and 1), using the following applications of the product rule for the time derivative.

$$\frac{\partial\left(\alpha_k \rho_k\right)}{\partial t} = \rho_k \frac{\partial\left(\alpha_k\right)}{\partial t} + \alpha_k \frac{\partial\left(\rho_k\right)}{\partial t} \tag{2.2}$$

and the divergence term,

$$\nabla\cdot\left(\alpha_k\rho_k\mathbf{U}_k\right)=\rho_k\nabla\cdot(\alpha_k\mathbf{U}_k)+\alpha_k\mathbf{U}_K\cdot\nabla\left(\rho_k\right) \tag{2.3}$$

to yield the following result,

$$\rho_k\frac{\partial\left(\alpha_k\right)}{\partial t}+\alpha_k\frac{\partial\left(\rho_k\right)}{\partial t}+\rho_k\nabla\cdot(\alpha_k\mathbf{U}_k)+\alpha_k\mathbf{U}_K\cdot\nabla\left(\rho_k\right)=\Gamma_k \tag{2.4}$$

Eq. 2.4 can be further manipulated by dividing both sides of the equations by the density of the corresponding phase, ρ_k and then rearranging the equations using the following definitions of the material or substantive derivative of the phase density.

$$\frac{D\left(\rho_k\right)}{D\,t}=\frac{\partial\left(\rho_k\right)}{\partial t}+\mathbf{U}_k\cdot\nabla\left(\rho_k\right) \tag{2.5}$$

This yields the following result.

$$\frac{\partial\left(\alpha_k\right)}{\partial t}+\nabla\cdot(\alpha_k\mathbf{U}_k)+\frac{\alpha_k}{\rho_k}\frac{D\left(\rho_k\right)}{D\,t}=\frac{\Gamma_k}{\rho_k} \tag{2.6}$$

Now, Eq. 2.6, also according to [64] can be further manipulated by the introduction of two definitions of velocity that relate the two fluid or phase velocities. The first definition used is the relative velocity, $\mathbf{U}_r$, given by the following definition,

$$\mathbf{U}_r=\mathbf{U}_1-\mathbf{U}_2 \tag{2.7}$$

The second definition is used for the mixture velocity, $\mathbf{U}$, and is given by the following,

$$\mathbf{U}=\alpha_1\mathbf{U}_1+\alpha_2\mathbf{U}_2 \tag{2.8}$$

Now, using the two relationships given above, and performing some basic mathematical manipulation, the following two relationships can be obtained. These relationships give definitions for the individual phase / fluid velocities as functions of the relative velocity,

mixture velocity, and void fraction.

$$\begin{aligned}\mathbf{U}_1 &= \mathbf{U} + \alpha_2 \mathbf{U}_r \\ \mathbf{U}_2 &= \mathbf{U} - \alpha_1 \mathbf{U}_r\end{aligned} \tag{2.9}$$

Now, substituing Eq. 2.9 into Eq. 2.6, the following continuity or void fraction equations can be obtained for each phase / fluid.

$$\frac{\alpha_1}{\rho_1}\frac{D\left(\rho_1\right)}{Dt} + \frac{\partial\left(\alpha_1\right)}{\partial t} + \nabla\cdot(\alpha_1\mathbf{U}) + \nabla\cdot(\alpha_1\alpha_2\mathbf{U}_r) = \frac{\Gamma_1}{\rho_1} \tag{2.10}$$

$$\frac{\alpha_2}{\rho_2}\frac{D\left(\rho_2\right)}{Dt} + \frac{\partial\left(\alpha_2\right)}{\partial t} + \nabla\cdot(\alpha_2\mathbf{U}) - \nabla\cdot(\alpha_1\alpha_2\mathbf{U}_r) = \frac{\Gamma_2}{\rho_2} \tag{2.11}$$

where the Γ_k terms signify the mass gained or lossed by the respective fluid k. It is also important to note that due to conservation of mass principles any mass gained by one fluid has to be lost by the other fluid; thus $\Gamma_2 = -\Gamma_1$ or $\Gamma_1 = -\Gamma_2$. Now, according to [64], in order to both guarantee the boundedness of the void fraction as well as essentially estimate the compressibility of both phases and effect of mass transfer, a relationship must be derived from summing Eq. 2.10 and Eq. 2.11 together. This gives the following,

$$\nabla\cdot(\mathbf{U}) = \frac{\Gamma_1}{\rho_1} - \frac{\Gamma_1}{\rho_2} - \frac{\alpha_1}{\rho_1}\frac{D\left(\rho_1\right)}{Dt} - \frac{\alpha_2}{\rho_2}\frac{D\left(\rho_2\right)}{Dt} \tag{2.12}$$

where $\alpha_1 + \alpha_2 = 1$. Eq. 2.12 looks very similar to the divergence free or incompressibility constraint of $\nabla\cdot\mathbf{U} = 0$ for incompressible flows; however, in this case the right hand side of the equation takes into account the compressibility of both fluids and the mass transfer between them as previously stated. So substituting Eq. 2.12 into Eq. 2.10 and Eq. 2.11 and performing some rearrangement utilizing the following,

$$\nabla\cdot(\alpha_k\mathbf{U}) = \alpha_k\nabla\cdot(\mathbf{U}) + \mathbf{U}\cdot\nabla(\alpha_k) \tag{2.13}$$

This yields the following forms of the continuity or void fraction equations for both phases or fluids.

$$\frac{\partial(\alpha_1)}{\partial t}+\mathbf{U}\cdot\nabla(\alpha_1)+\nabla\cdot(\alpha_1\alpha_2\mathbf{U}_r)=$$
$$\alpha_1\alpha_2\left(\frac{1}{\rho_2}\frac{D(\rho_2)}{Dt}-\frac{1}{\rho_1}\frac{D(\rho_1)}{Dt}\right)+\alpha_1\left(\frac{\Gamma_1}{\rho_2}-\frac{\Gamma_1}{\rho_1}\right)+\frac{\Gamma_1}{\rho_1} \tag{2.14}$$

$$\frac{\partial(\alpha_2)}{\partial t}+\mathbf{U}\cdot\nabla(\alpha_2)-\nabla\cdot(\alpha_1\alpha_2\mathbf{U}_r)=$$
$$\alpha_1\alpha_2\left(\frac{1}{\rho_1}\frac{D(\rho_1)}{Dt}-\frac{1}{\rho_2}\frac{D(\rho_2)}{Dt}\right)+\alpha_2\left(\frac{\Gamma_1}{\rho_2}-\frac{\Gamma_1}{\rho_1}\right)-\frac{\Gamma_1}{\rho_2} \tag{2.15}$$

Now by manipulating the convection term using the following relationship,

$$\mathbf{U}\cdot\nabla(\alpha_k)=\nabla\cdot(\alpha_k\mathbf{U})-\alpha_k(\nabla\cdot\mathbf{U}) \tag{2.16}$$

the conservation of mass equations for each phase or fluid can be re-written into the following form.

$$\frac{\partial(\alpha_1)}{\partial t}+\nabla\cdot(\alpha_1\mathbf{U})-\alpha_1(\nabla\cdot\mathbf{U})+\nabla\cdot(\alpha_1\alpha_2\mathbf{U}_r)=$$
$$\alpha_1\alpha_2\left(\frac{1}{\rho_2}\frac{D(\rho_2)}{Dt}-\frac{1}{\rho_1}\frac{D(\rho_1)}{Dt}\right)+\alpha_1\left(\frac{\Gamma_1}{\rho_2}-\frac{\Gamma_1}{\rho_1}\right)+\frac{\Gamma_1}{\rho_1} \tag{2.17}$$

$$\frac{\partial(\alpha_2)}{\partial t}+\nabla\cdot(\alpha_2\mathbf{U})-\alpha_2(\nabla\cdot\mathbf{U})-\nabla\cdot(\alpha_1\alpha_2\mathbf{U}_r)=$$
$$\alpha_1\alpha_2\left(\frac{1}{\rho_1}\frac{D(\rho_1)}{Dt}-\frac{1}{\rho_2}\frac{D(\rho_2)}{Dt}\right)+\alpha_2\left(\frac{\Gamma_1}{\rho_2}-\frac{\Gamma_1}{\rho_1}\right)-\frac{\Gamma_1}{\rho_2} \tag{2.18}$$

The final form of the conservation of mass, continuity or void fraction equations for both phases or fluids is given by the following.

$$\frac{\partial(\alpha_1)}{\partial t}+\nabla\cdot(\alpha_1\mathbf{U})-\alpha_1\nabla\cdot(\mathbf{U})+\nabla\cdot(\alpha_1\alpha_2\mathbf{U}_r)= \\ \alpha_1\alpha_2\left(\frac{1}{\rho_2}\frac{D(\rho_2)}{Dt}-\frac{1}{\rho_1}\frac{D(\rho_1)}{Dt}\right)+\alpha_1(\Gamma_{12}-\Gamma_{21})\left(\frac{1}{\rho_2}-\frac{1}{\rho_1}\right)+\frac{\Gamma_{12}-\Gamma_{21}}{\rho_1} \tag{2.19}$$

$$\frac{\partial(\alpha_2)}{\partial t}+\nabla\cdot(\alpha_2\mathbf{U})-\alpha_2\nabla\cdot(\mathbf{U})-\nabla\cdot(\alpha_1\alpha_2\mathbf{U}_r)= \\ -\alpha_1\alpha_2\left(\frac{1}{\rho_2}\frac{D(\rho_2)}{Dt}-\frac{1}{\rho_1}\frac{D(\rho_1)}{Dt}\right)+\alpha_2(\Gamma_{12}-\Gamma_{21})\left(\frac{1}{\rho_2}-\frac{1}{\rho_1}\right)-\frac{\Gamma_{12}-\Gamma_{21}}{\rho_2} \tag{2.20}$$

where the notation for the mass transfer terms can be explained by the following

- Γ_{12} : is the mass transferred from fluid-2 to fluid-1 (e.g. evaporation rate where fluid-1 is the dispersed vapor & fluid-2 is the continuous liquid).
- Γ_{21} : is the mass transferred from fluid-1 to fluid-2 (e.g. condensation rate where fluid-1 is the dispersed vapor & fluid-2 is the continuous liquid).
- $\Gamma_1=\Gamma_{12}-\Gamma_{21}$: which means that $\Gamma_1>0$ for the case of evaporation, $\Gamma_1=0$ for adiabatic cases, and finally $\Gamma_1<0$ for condensation cases.

2.2 Conservation of Momentum

The momentum conservation equation for a two-field (e.g. continuous & dispersed) two-fluid ($k=1,2$) model for fluid k is given by the following.

$$\frac{\partial(\alpha_k\rho_k\mathbf{U}_k)}{\partial t}+\nabla\cdot(\alpha_k\rho_k\mathbf{U}_k\mathbf{U}_k)=-\nabla(\alpha_k p)+\nabla\cdot[\alpha_k(\tau_k+\tau_k^t)]+\alpha_k\rho_k\mathbf{g}+\Gamma_{jk}\mathbf{U}_{jk}-\Gamma_{kj}\mathbf{U}_{kj}+\mathbf{M}_k \tag{2.21}$$

where the subscripts k and j indicate the two fluids / phases (i.e. the dispersed and continuous fluids / phases or vice versa), $\tau_k+\tau_k^t$ are the combined Reynolds viscous and turbulent stress, $\mathbf{M}_k$ is the averaged interfacial momentum transfer term that needs accurate modeling, and $\Gamma_{jk}\mathbf{U}_{jk}-\Gamma_{kj}\mathbf{U}_{kj}$ accounts for the momentum tranfer during phase change, where

the velocities $\mathbf{U}_{jk}$ and $\mathbf{U}_{jk}$ are found using the following,

$$\mathbf{U}_{jk} = \begin{cases} \mathbf{U}_j, & \text{if } \Gamma_{jk} > 0 \\ \mathbf{U}_k, & \text{if } \Gamma_{jk} < 0 \end{cases} \tag{2.22}$$

$$\mathbf{U}_{kj} = \begin{cases} \mathbf{U}_k, & \text{if } \Gamma_{kj} > 0 \\ \mathbf{U}_j, & \text{if } \Gamma_{kj} < 0 \end{cases} \tag{2.23}$$

In order to model the Reynolds stress, the Boussinesq hypothesis for turbulent stress-strain relation is used. This hypothesis is valid only for Newtonian fluids and is represented by the following,

$$\begin{aligned} \tau_k^{eff} &= \tau_k + \tau_k^t \\ &= \rho_k \nu_k^{eff} \left[\nabla \mathbf{U}_k + (\nabla \mathbf{U}_k)^T - \frac{2}{3} \mathbf{I} \nabla \cdot \mathbf{U}_k \right] - \frac{2}{3} \mathbf{I} \rho_k k_k \end{aligned} \tag{2.24}$$

where the identity tensor is identified with $\mathbf{I}$, the turbulent kinetic energy is k_k, the effective kinematic viscosity is $\nu_k^{eff} = \nu_k + \nu_k^t$, ν_k^t is the turbulent kinematic viscosity and ν_k is the physical kinematic viscosity of fluid / phase k. The next step in the derivation process for many others is then to divide through by both the void fraction and the density to get the phase-intensive momentum equation. The benefits of this form of the momentum equations is the l.h.s. of the equation is essentially a single phase momentum equation which significantly simplifies the implementation, also this formulation prevents the momentum equation from becoming singular when the phase fraction approaches zero. However, dividing by the void fraction is a big disadvantage in the phase-intensive formulation and thus the phase-intensive formulation was not employed here. We simply use the chain rule to split the l.h.s. time derivative and convection term,

$$\begin{aligned} \rho_k \frac{\partial (\alpha_k \mathbf{U}_k)}{\partial t} + \rho_k \nabla \cdot (\alpha_k \mathbf{U}_k \mathbf{U}_k) + \alpha_k \mathbf{U}_k \frac{\partial \left(\rho_k\right)}{\partial t} + \alpha_k \mathbf{U}_k \mathbf{U}_k \cdot \nabla \left(\rho_k\right) = \\ -\nabla \left(\alpha_k p\right) + \nabla \cdot \left(\alpha_k \tau_k^{eff}\right) + \alpha_k \rho_k \mathbf{g} + \Gamma_{jk} \mathbf{U}_{jk} - \Gamma_{kj} \mathbf{U}_{kj} + \mathbf{M}_k \end{aligned} \tag{2.25}$$

and then divide through by the phase density to get the following.

$$\begin{aligned}\frac{\partial(\alpha_k\mathbf{U}_k)}{\partial t}+\nabla\cdot(\alpha_k\mathbf{U}_k\mathbf{U}_k)+\frac{\alpha_k\mathbf{U}_k}{\rho_k}\left[\frac{\partial(\rho_k)}{\partial t}+\mathbf{U}_k\cdot\nabla(\rho_k)\right]=\\ -\frac{\nabla(\alpha_k p)}{\rho_k}+\frac{\nabla\cdot\left(\alpha_k\tau_k^{eff}\right)}{\rho_k}+\alpha_k\mathbf{g}+\frac{\Gamma_{jk}\mathbf{U}_{jk}-\Gamma_{kj}\mathbf{U}_{kj}}{\rho_k}+\frac{\mathbf{M}_k}{\rho_k}\end{aligned} \tag{2.26}$$

where the substantive derivative of the density can be substituted in the following manner,

$$\begin{aligned}\frac{\partial(\alpha_k\mathbf{U}_k)}{\partial t}+\nabla\cdot(\alpha_k\mathbf{U}_k\mathbf{U}_k)+\frac{\alpha_k\mathbf{U}_k}{\rho_k}\frac{D(\rho_k)}{Dt}=\\ -\frac{\nabla(\alpha_k p)}{\rho_k}+\frac{\nabla\cdot\left(\alpha_k\tau_k^{eff}\right)}{\rho_k}+\alpha_k\mathbf{g}+\frac{\Gamma_{jk}\mathbf{U}_{jk}-\Gamma_{kj}\mathbf{U}_{kj}}{\rho_k}+\frac{\mathbf{M}_k}{\rho_k}\end{aligned} \tag{2.27}$$

Now according to Rusche [49], the viscous stress terms in the momentum equation can be decomposed, for numerical reason, into a diffusive component in a correction component in the following manner,

$$\begin{aligned}\mathbf{R}_k^{eff}&=-\frac{\tau_k^{eff}}{\rho_k}\\ &=\mathbf{R}_k^{eff,D}+\mathbf{R}_k^{eff,C}\end{aligned} \tag{2.28}$$

where

$$\begin{aligned}\mathbf{R}_k^{eff,D}&=-\nu_k^{eff}\nabla\mathbf{U}_k\\ \mathbf{R}_k^{eff,C}&=\mathbf{R}_k^{eff}-\mathbf{R}_k^{eff,D}\\ &=\mathbf{R}_k^{eff}+\frac{\tau_k^{eff}}{\rho_k}\\ &=\nu_k^{eff}\left[(\nabla\mathbf{U}_k)^T-\frac{2}{3}\mathbf{I}\nabla\cdot\mathbf{U}_k\right]-\frac{2}{3}\mathbf{I}k_k\end{aligned} \tag{2.29}$$

Now substituing in the diffusive and corrective component for the viscous stress terms yields the following formulation,

$$\frac{\partial(\alpha_k \mathbf{U}_k)}{\partial t} + \nabla\cdot(\alpha_k \mathbf{U}_k \mathbf{U}_k) + \frac{\alpha_k \mathbf{U}_k}{\rho_k}\frac{D(\rho_k)}{Dt} = -\frac{\nabla(\alpha_k p)}{\rho_k} + \nabla\cdot\left(\alpha_k \mathbf{R}_k^{eff,D}\right) + \nabla\cdot\left(\alpha_k \mathbf{R}_k^{eff,C}\right) + \alpha_k \mathbf{g} + \frac{\Gamma_{jk}\mathbf{U}_{jk} - \Gamma_{kj}\mathbf{U}_{kj}}{\rho_k} + \frac{\mathbf{M}_k}{\rho_k} \tag{2.30}$$

This is the final non-discrete formulation that is use for the momentum transport equations. The momentum equation linear systems are constructed; however, they are not solved directly, as according to Rusche [49], this was found that it can lead to instabilities. The approximate solutions of the momentum equations are calculated using the linear system coefficient matrix and r.h.s. matrix to give an approximation of the velocity field that does not obey the continuity equation. The velocity field is then corrected using the updated pressure field which obeys continuity. Then an iterative procedure is started in order to obtain a better approximation of the velocity field that satisfies both the momentum and continuity equation.

2.3 Conservation of Energy

The energy conservation equation for a two-field (e.g. continuous & dispersed) two-fluid ($k = 1,2$) model for fluid k is given by the following.

$$\frac{\partial(\alpha_k \rho_k E_k)}{\partial t} + \nabla\cdot(\alpha_k \rho_k E_k \mathbf{U}_k) + \nabla\cdot\left[\alpha_k\left(\mathbf{q}_k + \mathbf{q}_k^t\right)\right] = -\nabla\cdot(\alpha_k \mathbf{U}_k p) + h_{k,i}\Gamma_{k,i} + q''_{i,k}a_{i,k} + q'''_k \tag{2.31}$$

where q'''_k is the volumetric source, $q''_{k,i}a_{i,k}$ is the source from interfacial heat transfer, and $h_{k,i}\Gamma_{k,i}$ is the source from phase change. This equation does not include the mechanical source terms $\nabla\cdot(\tau_k\cdot\mathbf{U}_k)$ and $\rho_k\mathbf{g}\cdot\mathbf{U}_k$ that account for power and heat due to bulk motion and potential energy. The lack of use of a mechanical stress tensor could potentially affect the temperature or enthalpy distributions for highly compressible flows as well as transonic or supersonic flows as the rate of change of strain energy plays an important role in those situations. In general, this is not the aim of our solver so we do not include these terms. The first step in the formulation derivation is to use the chain rule and definition of a substantive

derivative to manupulate the first two terms on the l.h.s. in the following manner,

$$\begin{aligned}\frac{\partial\left(\alpha_k\rho_k E_k\right)}{\partial t}+\nabla\cdot\left(\alpha_k\rho_k E_k\mathbf{U}_k\right)&=\rho_k\left[\frac{\partial\left(\alpha_k E_k\right)}{\partial t}+\nabla\cdot\left(\alpha_k E_k\mathbf{U}_k\right)\right]+\alpha_k E_k\left[\frac{\partial\left(\rho_k\right)}{\partial t}+\nabla\cdot\left(\rho_k\mathbf{U}_k\right)\right]\\&=\rho_k\left[\frac{\partial\left(\alpha_k E_k\right)}{\partial t}+\nabla\cdot\left(\alpha_k E_k\mathbf{U}_k\right)\right]+\alpha_k E_k\frac{D\left(\rho_k\right)}{D t}\end{aligned} \tag{2.32}$$

Now we use the relation between internal energy and total energy, $E=e+\ \mathbf{U}^2 2=e+K$, and the definition of a substantive derivative, to get the following formulation for the above result,

$$\begin{aligned}&\rho_k\left[\frac{\partial\left(\alpha_k E_k\right)}{\partial t}+\nabla\cdot\left(\alpha_k E_k\mathbf{U}_k\right)\right]+\alpha_k E_k\frac{D\left(\rho_k\right)}{D t}\\&=\rho_k\left[\frac{\partial\left(\alpha_k e_k\right)}{\partial t}+\nabla\cdot\left(\alpha_k e_k\mathbf{U}_k\right)+\frac{\partial\left(\alpha_k K_k\right)}{\partial t}+\nabla\cdot\left(\alpha_k K_k\mathbf{U}_k\right)\right]+\alpha_k\left(e_k+K_k\right)\frac{D\left(\rho_k\right)}{D t}\end{aligned} \tag{2.33}$$

Now substituting this back into the original equation to get the total energy formulation in terms of internal energy,

$$\begin{aligned}&\rho_k\left[\frac{\partial\left(\alpha_k e_k\right)}{\partial t}+\nabla\cdot\left(\alpha_k e_k\mathbf{U}_k\right)+\frac{\partial\left(\alpha_k K_k\right)}{\partial t}+\nabla\cdot\left(\alpha_k K_k\mathbf{U}_k\right)\right]=\\&-\nabla\cdot\left[\alpha_k\left(\mathbf{q}_k+\mathbf{q}_k^t\right)\right]+\nabla\cdot\left(\alpha_k\mathbf{U}_k p\right)+h_{k,i}\Gamma_{k,i}+q''_{k,i}a_{i,k}+q'''_k+\alpha_k\left(e_k+K_k\right)\frac{D\left(\rho_k\right)}{D t}\end{aligned} \tag{2.34}$$

We can re-write this formulation for enthalpy, enthalpy is the sum of internal energy and kinematic pressure, $h=e+\ p\rho$,

$$\begin{aligned}&\rho_k\left[\frac{\partial\left(\alpha_k e_k\right)}{\partial t}+\nabla\cdot\left(\alpha_k e_k\mathbf{U}_k\right)+\frac{\partial\left(\alpha_k K_k\right)}{\partial t}+\nabla\cdot\left(\alpha_k K_k\mathbf{U}_k\right)\right]=\\&-\nabla\cdot\left[\alpha_k\left(\mathbf{q}_k+\mathbf{q}_k^t\right)\right]+\frac{\partial\left(\alpha_k p\right)}{\partial t}+h_{k,i}\Gamma_{k,i}+q''_{k,i}a_{i,k}+q'''_k+\alpha_k\left(e_k+K_k\right)\frac{D\left(\rho_k\right)}{D t}\end{aligned} \tag{2.35}$$

where the only difference between the two formulations is the second term on the r.h.s. of the equation. Now, using Fourier's law of conduction inside phase k, the molecular heat flux, $\mathbf{q}_k$, can be transformed,

$$\mathbf{q}_k=-\frac{\lambda_k}{C_{p,k}}\nabla h_k \tag{2.36}$$

where λ_k and $C_{p,k}$ are the phase or fluid k thermal conductivity and specific heat respectively. A similar transformation can be done for the turbulent heat flux, $\mathbf{q}_k^t$,

$$\mathbf{q}_k^t = -\frac{\lambda_k^t}{C_{p,k}} \nabla h_k \tag{2.37}$$

where λ_k^t is the turbulent thermal conductivity and can be obtained from the following relation,

$$\lambda_k^t = \frac{C_{p,k}\, \nu_k^t \rho_k}{Pr_k^t} \tag{2.38}$$

where Pr_k^t is the turbulent Prandlt number of phase k typically with a constant value of 0.9 of slightly less than 1, and ν_k^t is the turbulent kinematic viscosity of phase k. Therefore, for each phase k (e.g. the dispersed phase or continuous phase) the effective heat flux can be formulated as follows,

$$\begin{aligned} \mathbf{q}_k^{eff} &= -\left(\frac{\lambda_k}{C_{p,k}} + \frac{\lambda_k^t}{C_{p,k}} \right) \nabla h_k \\ &= -\left(\frac{\lambda_k}{C_{p,k}} + \frac{\nu_k^t \rho_k}{Pr_k^t} \right) \nabla h_k \end{aligned} \tag{2.39}$$

It is important to note that when solving for internal energy, these terms need to be multiplied by $\frac{C_{p,1}}{C_{v,1}}$ which is the ratio of specific heats. Taking this definition and substituting it into the energy equation formulation, as well as, dividing through by the density, yields the following energy equation formulation in terms of enthalpy,

$$\begin{aligned} &\frac{\partial (\alpha_k e_k)}{\partial t} + \nabla \cdot (\alpha_k e_k \mathbf{U}_k) + \frac{\partial (\alpha_k K_k)}{\partial t} + \nabla \cdot (\alpha_k K_k \mathbf{U}_k) = \\ &\qquad -\nabla \cdot \left(\frac{\alpha_k}{\rho_k} \mathbf{q}_k^{eff} \right) + \frac{1}{\rho_k} \frac{\partial \left(\alpha_k p \right)}{\partial t} + \frac{\Gamma_{jk} h_{jk} - \Gamma_{kj} h_{kj}}{\rho_k} + \frac{q''_{k,i} a_{i,k}}{\rho_k} + \frac{q'''_k}{\rho_k} + \frac{\alpha_k (e_k + K_k)}{\rho_k} \frac{D\left(\rho_k\right)}{Dt} \end{aligned} \tag{2.40}$$

where the subscripts k and j indicate the two fluids or phases (i.e. the dispersed and continuous fluids or phases or vice versa) and $\Gamma_{jk} h_{jk} - \Gamma_{kj} h_{kj}$ accounts for the energy source

during phase change, where the enthalpies h_{jk} and h_{jk} are found using the following,

$$h_{jk} = \begin{cases} h_j, & \text{if } \Gamma_{jk} > 0 \\ h_k, & \text{if } \Gamma_{jk} < 0 \end{cases} \tag{2.41}$$

$$h_{kj} = \begin{cases} h_k, & \text{if } \Gamma_{kj} > 0 \\ h_j, & \text{if } \Gamma_{kj} < 0 \end{cases} \tag{2.42}$$

Chapter 3

TURBULENCE CLOSURE MODELS

3.1 Continuous Phase Turbulence Model

In order to obtain the value of the turbulent kinematic viscosity, a fairly standard form of the $k-\epsilon$ turbulence model is currently employed in our solver. The turbulent viscosity is then used to model the effect of the turbulence on the Reynolds stresses in the momentum conservation equation. The $k-\epsilon$ model solves two differential transport equations in order to determine the turbulent kinetic energy, k, and the turbulent energy dissipation rate, ϵ, for the liquid or continuous phase. Using those two values the turbulent kinematic viscosity is the computed as,

$$\nu_2^t = \frac{C_\mu k_2^2}{\epsilon_2} \tag{3.1}$$

To account for enhanced turbulence in the continuous phase due to the presence of the dispersed phase, Sato & Sekoguchi's enhanced turbulence model [51],

$$\nu_2^D = \frac{1}{2} C_b \alpha_1 D_b \left|\mathbf{U}_1 - \mathbf{U}_2\right| \tag{3.2}$$

can be employed and added to the effective kinematic viscosity in the following manner,

$$\nu_2^{\text{eff}} = \nu_2 + \nu_2^t + \nu_2^D = \frac{\mu_2}{\rho_2} + \frac{C_\mu k_2^2}{\epsilon_2} + \nu_2^D \tag{3.3}$$

and the effective thermal diffusivity as,

$$\theta_2^{\text{eff}} = \frac{\lambda_2}{\rho_2 C_{p,2}} + \frac{\nu_2^t}{\text{Pr}_2^t} + \frac{\nu_2^D}{\text{Pr}_2^t} \tag{3.4}$$

where Pr_2^t is the turbulent prandlt number, assumed to be equal to 0.9, and the remaining coefficients are defined as $C_b = 1.2$ and $C_\mu = 0.09$. Our form of the $k-\epsilon$ model is loosely based off of the form developed by Yao & Morel [67]. Their form was developed in the frame of sub-cooled boiling modeling and had aditional source terms that were added to incorporate the effects of the dispersed phase on the liquid turbulence. Our model does not incorporate those additional terms as they are accounted for in a different manner, proposed by Sato & Sekoguchi [51]outside of the $k-\epsilon$ transport equations. Michta [41] employed a simplified form of the Yao & Morel model that is very similar to ours in that it does not take into account the additional terms and assumes the continuous or liquid phase is incompressible. The incompressibility assumption is a valid argument with the types of flows typically solved for, but our formulation does not include the incompressibility assumption to leave open the ability to simulate compressible problems. The equation for the turbulent kinetic energy of the liquid phase ($k = 2$), k_2, is given by the following,

$$\frac{\partial(\alpha_k k_k)}{\partial t} + \nabla\cdot(\alpha_k k_k \mathbf{U}_k) + \frac{\alpha_k k_k}{\rho_k}\frac{D(\rho_k)}{Dt} = \nabla\cdot\left[\alpha_k\left(\nu_k + \frac{\nu_k^t}{\sigma_k}\right)\nabla k_k\right] + \alpha_k G_k - \alpha_k \epsilon_k \tag{3.5}$$

and the equation for the energy dissipation rate of the liquid phase ($k = 2$), ϵ_2, is given by the following,

$$\frac{\partial(\alpha_k \epsilon_k)}{\partial t} + \nabla\cdot(\alpha_k \epsilon_k \mathbf{U}_k) + \frac{\alpha_k \epsilon_k}{\rho_k}\frac{D(\rho_k)}{Dt} = \nabla\cdot\left[\alpha_k\left(\nu_k + \frac{\nu_k^t}{\sigma_\epsilon}\right)\nabla \epsilon_k\right] + \frac{C_{\epsilon 1}\alpha_k G_k \epsilon_k}{k_k} - \frac{C_{\epsilon 2}\alpha_k \epsilon_k^2}{k_k} \tag{3.6}$$

where the coefficients are defined as $C_{\epsilon 1} = 1.44$, $C_{\epsilon 2} = 1.92$, $C_\mu = 0.09$, $\sigma_\epsilon = 1.3$ and $\sigma_k = 1.0$. The term G_k stands for the production of turbulent kinetic energy due to viscous forces and is given by the following relationship,

$$G_2 = \nu_2^t\left[\nabla\mathbf{U}_2 : \text{dev}\left(\nabla\mathbf{U}_2 + (\nabla\mathbf{U}_2)^T\right)\right] \tag{3.7}$$

where ":" stands for the double inner product and the operator "dev" takes the devatoric component of a rank 2 tensor **T** with the property of being traceless,

$$\text{dev}(\mathbf{T}) = \mathbf{T} - \frac{1}{3}\text{tr}(\mathbf{T})\mathbf{I} \tag{3.8}$$

where **I** is the identity matrix. According to Ghione [21], this formulation of the production of turbulent kinetic energy is not in agreement with the formulation in Rusche [49]. This is due to the fact that this form is missing a multiplying factor equal to 2 and ν_2^t is used instead of ν_2^{eff}; however, according to [44], the standard $k-\epsilon$ model contains a turbulent enery production term that can be expressed using tensorial notation as the following,

$$G = -\left\langle \mathbf{U}_i \mathbf{U}_j \right\rangle \frac{\partial (\mathbf{U}_i)}{\partial x_j} \tag{3.9}$$

where $\left\langle \mathbf{U}_i \mathbf{U}_j \right\rangle$ is the liquid Reynolds turbulent stress tensor that when expressed according to the Boussinesq hypothesis,

$$\tau_2 = -\left\langle \mathbf{U}_i \mathbf{U}_j \right\rangle = \nu_2^t \left(\nabla \mathbf{U}_2 + (\nabla \mathbf{U}_2)^T\right) - \frac{2}{3}\left(\nu_2^t \nabla \cdot \mathbf{U}_2\right)\mathbf{I} \tag{3.10}$$

it can be proven that the kinetic energy production term in our formulation is correct.

3.2 Dispersed Phase Turbulence Model

The turbulence of the dispersed or vapor phase in our solver is assumed to be depended on that of the liquid phase through the use of what is called a turbulence response coefficient, C_t. Rusche [49] states that this coefficient is defined as the ratio of the root mean square velocity fluctuations of the dispersed phase velocity, $\mathbf{U}_1'$ and of the continuous phase velocity, $\mathbf{U}_2'$,

$$C_t = \frac{\mathbf{U}_1'}{\mathbf{U}_2'} \tag{3.11}$$

According to experimental results, Rusche [49] found out that there is a dependancy between the turbulence response coefficient and the void fraction of the dispersed or vapor phase, α_1. This dependancy displays that for low void fraction (e.g. $\alpha_1 < 6$ %) the value of C_t is larger than 1, but for cases of void fraction greater than 6% the value of C_t reaches an almost constant value of 1.0. So this suggests that for a wide range of void fraction distributions, the

turbulence response coefficient, C_t, for the vapor or dispersed phase should have a value equal to 1.0 even though until recently the turbulence of the dispersed or vapor phase has been neglected and a turbulence response coefficient equal to 0.0 has been employed. The turbulence response coefficient is used to calculate the turbulent kinematic viscosity of the dispersed or vapor phase and this gives the following definition for the effective kinematic viscosity of the dispersed or vapor phase ($k = 1$),

$$\nu_1^{\text{eff}} = \nu_1 + \nu_1^t = \frac{\mu_1}{\rho_1} + C_t^2 \nu_2^t \tag{3.12}$$

where the turbulent kinetic energy of the vapor or dispersed phase (k=1) is given by the following,

$$k_1 = C_t^2 k_2 \tag{3.13}$$

and the effective thermal diffusivity as,

$$\theta_1^{eff} = \frac{\lambda_1}{\rho_1 C_{p,1}} + \frac{\nu_1^t}{\text{Pr}_1^t} \tag{3.14}$$

where Pr_1^t is the turbulent prandlt number and assumed to be equal to 0.9.

3.3 Wall Function Models

Wall functions within the $k-\epsilon$ model implementation are used in order to properly predict the phase velocity profile in regions close to the wall where in turbulent flows a viscous or laminar sub-layer and log-layer profile can be observed according to the law of the wall. The turbulent kinetic energy, k_k, equation can be solved on the whole domain (including the near-wall cells); however, for the turbulent energy dissipation rate, ϵ_k, equation it is not the case. Special values in the near-wall cells are set for the liquid turbulent kinematic viscosity. Before evaluating the energy dissipation rate equation the value of \epsilon_k in the near-wall cells is evaluated using the following,

$$\epsilon_2^{nw}\left(y^+\right) = \begin{cases} 0, & \text{if } y^+ < y_m^+ \\ \frac{C_\mu^{\frac{3}{4}} k_2^{\frac{3}{2}}}{\kappa y}, & \text{if } y^+ > y_m^+ \end{cases} \tag{3.15}$$

where the Von-Karman constant is $\kappa = 0.4187$, the non-dimensional distance from the wall where the transition from the log-layer to the outer layer of the boundary happens is , $y_m^+ = 11.225 - 11.6$, and the non-dimensional distance from the wall, y^+, is computed using the following,

$$y^+ = \frac{C_\mu^{\frac{1}{4}} k_2^{\frac{1}{2}}}{\nu_2} y \tag{3.16}$$

where y represents the distance from the nearest wall. The turbulent energy production term, G_k, must also be adjusted in the near-wall cells by calculating a dependence on the value of non-dimensional distance from the wall, y^+, using the following relationship,

$$G_2^{nw}\left(y^+\right) = \begin{cases} 0, & \text{if } y^+ < y_m^+ \\ \frac{\nu_2^t C_\mu^{\frac{1}{4}} k_2^{\frac{1}{2}}}{\kappa y} \nabla^\perp \mathbf{U}_2, & \text{if } y^+ > y_m^+ \end{cases} \tag{3.17}$$

Now given the solutions to the turbulent kinetic energy, k_2, equation and the turbulent energy dissipation rate, ϵ_2, equation for the liquid or continuous phase ($k = 2$), the turbulent liquid viscosity at the wall must be adjusted using a near-wall relationship given by the following,

$$\nu_2^{t,nw}\left(y^+\right) = \begin{cases} 0, & \text{if } y^+ < y_m^+ \\ \nu_2 \left[\frac{\kappa y^+}{\ln\left(E\, y^+\right)} - 1 \right], & \text{if } y^+ > y_m^+ \end{cases} \tag{3.18}$$

where $E = 9.8$ and $\mathrm{Pr}^t = 0.9$.

Chapter 4

INTERFACIAL MOMENTUM TRANSFER CLOSURE MODELS

In this section the closure laws for the interfacial momentum transfer source term on the r.h.s. of the momentum equation is discussed in detail. The interfacial momentum transfer is caused via forces acting at the interface between the two phases or fluids. For example, forces acting on a bubble are cause by the liquid which surrounds it. According to Newton's third law of motion,

$$\mathbf{M}_1 + \mathbf{M}_2 = 0 \tag{4.1}$$

where $\mathbf{M}_1$ and $\mathbf{M}_2$ are the averaged interfacial momentum transfer terms for phase 1 and phase 2 respectively. The bubble / droplet is subjected to different kinds of forces that require specific modeling. The implemented forces for our solver are interfacial drag, lift, wall lubrication, virtual mass, and turbulence dispersion. The application of these forces to the averaged interfacial momentum transfer term can be summarized by the following

$$\mathbf{M}_1 = \mathbf{M}_1^{drag} + \mathbf{M}_1^{lift} + \mathbf{M}_1^{walll} + \mathbf{M}_1^{tdisp} + \mathbf{M}_1^{vmass} \tag{4.2}$$

Under fully developed flow conditions, the drag force determines the terminal velocity of the bubble through a balance with the bouyancy force, conversely the balance of the lateral forces acting on the bubble influences the void fraction profile and in general, acts as in the following manner: the wall lubrication force drives bubble away from the walls, the lift force pushes "small" bubbles towards the wall and "large" bubbles towards the centerline, and the turbulence dispersion force evens out gradients in the void fraction

distribution. Weller [64] suggested a mixture model for the modeling of the drag, lift, and virtual mass force. This model represented the use of a numerical trick to allow the solver to handle phase separation and annular flow with entrained droplets (e.g. the continuous phase becomes the dispersed phase), however, these sorts of situations are outside our desired range of applicability (sub-cooled boiling) where the only possible dispersed phase is the vapor phase. Therefore, this approach was abandoned and the following standard implementation for the dispersed / vapor phase $k = 1$ and the continuous / liquid phase $k = 2$ was implemented in our solver,

$$\mathbf{M}_1 = -\frac{3}{4}\frac{C_d}{d_b}\rho_2\,\alpha_a\,|\mathbf{U}_r|\,\mathbf{U}_r - C_l\,\rho_2\,\alpha_1\,\mathbf{U}_r \times \nabla \times \mathbf{U}_2 - C_{vm}\,\rho_2\,\alpha_1\left(\frac{D(\mathbf{U}_1)}{Dt} - \frac{D(\mathbf{U}_2)}{Dt}\right) + \mathbf{M}_1^{wall} + \mathbf{M}_1^{tdisp} \tag{4.3}$$

In the following sections, the models for the different forces acting on the bubble are introduced and briefly discussed.

4.1 Interfacial Drag Models

This force represents the resistant opposed to the bubble motion in the fluid, or in a more general sense, the resistance of the relative motion between the two phases. The drag force depends on the bubble, droplet or particulate size; for example, a larger bubble will experience a larger drag force than a smaller bubble. Also, the drag force depends on the relative velocity between the two phases or fluids.

$$\mathbf{U}_r = \mathbf{U}_1 - \mathbf{U}_2 \tag{4.4}$$

The form of the drag force in the momentum equations is given by the following,

$$\mathbf{M}_1^{drag} = -\mathbf{M}_2^{drag} = -\frac{3}{4}\frac{C_d}{D_b}\rho_2\,\alpha_1\,|\mathbf{U}_r|\,\mathbf{U}_r = -\frac{3}{4}\frac{C_d}{D_b}\rho_2\,\alpha_1\,|\mathbf{U}_1 - \mathbf{U}_2|\,\mathbf{U}_1 - \mathbf{U}_2 \tag{4.5}$$

where D_b is the mean Sauter bubble diameter, defined as the diameter of a sphere that has the same volume-to-surface ration of the bubble and C_d is the drag coefficient which needs careful modeling. The drag coefficient is usually deduced from experiments, and many models have been developed over the years to match various experimental data sets. Rusche [49] performed a very complete literature study on interfacial force modeling and many of the conclusions drawn where applied to our work. The following sections will

cover the different drag force models that are implemented in the solver.

4.1.1 Constant Drag Model

This model is used to test the functionality and stability / sensitivity of the drag force model in the solver. The drag coefficient C_d is user defined and constant.

4.1.2 Schiller & Naumann Drag Model

This formulation for the drag coefficient, given in [52], is valid only for solid sphereical particles with $\mathrm{Re}_b < 1000$, so for $\mathrm{Re}_b > 1000$ the drag coefficient for solid particles can be approximated to be constant and equal to a value of 0.44 according to [49]. Therefore, the following numerical model was implemented.

$$C_d = \max\left(\frac{24}{\mathrm{Re}_b}\left(1.0 + 0.15\mathrm{Re}_b^{0.687}\right), 0.44\right) \tag{4.6}$$

where the bubble Reynolds number is given by the following definition

$$\mathrm{Re}_b = \frac{\rho_2 \left|\mathbf{U}_1 - \mathbf{U}_2\right| D_b}{\mu_2} \tag{4.7}$$

4.1.3 Ishii & Zuber Drag Model

The model given by Ishii & Zuber [30] is similar to the Schiller & Naumann drag coefficient in that it is valid only for solid particles in the undistorted regime. It has a form that is very similar to Schiller & Naumann, which is given by the following

$$C_d = \max\left(\frac{24}{\mathrm{Re}_{bm}}\left(1.0 + 0.15\mathrm{Re}_{bm}^{0.687}\right), 0.44\right) \tag{4.8}$$

where the bubble Reynolds number is given by the following definition, which is slightly different than Schiller & Naumann's definition because it uses a "mixture" dynamic viscosity, whose definition is also given below.

$$\mathrm{Re}_{bm} = \frac{\rho_2 \left|\mathbf{U}_1 - \mathbf{U}_2\right| D_b}{\mu_m} \tag{4.9}$$

$$\mu_m = \mu_2 \left(1 - \frac{\alpha_1}{\alpha_{max}}\right)^{\frac{-2.5\,\alpha_{max}}{\mu^*}} \tag{4.10}$$

$$\mu^* = \frac{\mu_1 + 0.4\mu_2}{\mu_1 + \mu_2} \tag{4.11}$$

where α_{max} is the maximum phase fraction and depends on the maximum packing value considered. There are several options for this term's value.

- $\alpha_{max} = 0.74048$ from Ghione [21] which is equal to the maximum possible packing for solid spheres as used in [19].
- $\alpha_{max} = 0.62$ from Rusche [49] for solid particles and $\alpha_{max} = 1.0$ for fluid particles only if the Ishii & Zuber model that is valid for bubbles is used.
- $\alpha_{max} = 0.52$ from Michta [41]

4.1.4 Ergun Drag Model

This model was developed by Ergun [17] as a general correlation for the pressure drop per unit length over a fixed fluidized bed. Many researchers [23] assume the Ergun equation to be valid under fluidization conditions for $\alpha_2 < 0.8$ so that the equation can be re-written as a drag function applicable to a two-fluid model. The correlation has the following form

$$\frac{3}{4}\frac{C_d}{D_b}\rho_2\,\alpha_1\,|\mathbf{U}_r| = \frac{150\,\alpha_1^2\mu_2}{\alpha_2^2\,D_b^2} + \frac{1.75\,\rho_2\,\alpha_1\,|\mathbf{U}_r|}{\alpha_2\,D_b} \tag{4.12}$$

which gives the following form for the drag coefficient C_d

$$C_d = 150\,\frac{4}{3}\frac{\alpha_1}{\alpha_2^2\,\mathrm{Re}_b} + 1.75\,\frac{4}{3}\frac{1}{\alpha_2} \tag{4.13}$$

where the bubble Reynolds number is given by the following definition

$$\mathrm{Re}_b = \frac{\rho_2\,|\mathbf{U}_1 - \mathbf{U}_2|\,D_b}{\mu_2} \tag{4.14}$$

4.1.5 Gibilaro Drag Model

This model was developed by Gibilaro et al. [22] by introducing a correlation for pressure drop per unit length for fluidized beds, covering the whole range of possible values for the

voidage function. The correlation states the following relationship

$$\frac{3}{4}\frac{C_d}{D_b}\rho_2\,\alpha_1\,|\mathbf{U}_r| = \left[\frac{17.3}{\mathrm{Re}_b}+0.336\right]\frac{\rho_2\,\alpha_1\,|\mathbf{U}_r|\,\alpha_2^{-1.8}}{D_b} \tag{4.15}$$

where the bubble Reynolds number is given by the following definition

$$\mathrm{Re}_b = \frac{\rho_2\,\alpha_2\,|\mathbf{U}_1-\mathbf{U}_2|\,D_b}{\mu_2} \tag{4.16}$$

which gives the following form for the drag coefficient C_d

$$C_d = \frac{4}{3}\left[\frac{17.3}{\mathrm{Re}_b}+0.336\right]\alpha_2^{-1.8} \tag{4.17}$$

4.1.6 Gidaspow Drag Model

This model was developed by Gidaspow [23] and is essentially the same formulation as Wen & Yu's drag force coefficient model except that it has a slight difference in the estimation of the bubble Reynolds number. The formulation is given by the following

$$C_d = \max\left(\frac{24}{\mathrm{Re}_b}\left(1.0+0.15\mathrm{Re}_b^{0.687}\right),0.44\right)\alpha_2^{-1.7} \tag{4.18}$$

where the bubble Reynolds number is given by the following definition

$$\mathrm{Re}_b = \frac{\rho_2\,\alpha_2\,|\mathbf{U}_1-\mathbf{U}_2|\,D_b}{\mu_2} \tag{4.19}$$

The different recommended values for the liquid phase or continuous fluid void fraction α_2 are listed below.

- CFX [6]- α_2^e where $e=-1.65$
- Rusche [49] - α_2^e where $e=-1.7$
- Original Formulation [65] - α_2^e where $e=-2.65$

This model is only valid for a $\alpha_2 > 0.8$ or basically cases of maximum void fraction of the dispersed phase being less than 20%.

4.1.7 Syamlal & O'Brien Drag Model

This model was developed by Syamlal & O'Brien [16, 55, 56] and this correlation for the drag force coefficient has been used for both circulation and bubbling fluidized beds [53, 54]. They derived this correlation, given by the following, by converting terminal velocity correlations from experimental data to drag correlations, as opposed to most other drag correlations which are developed from high void fraction cases and pressure drop relations.

$$\mathbf{M}_1^{drag} = -\frac{3}{4}\frac{C_d}{D_b}\frac{\rho_2\,\alpha_1\,\alpha_2}{V_{rb}^2}\,|\mathbf{U}_r|\,\mathbf{U}_r \tag{4.20}$$

where V_{rb} is the terminal velocity correlation for bubble, droplet, or particulate which has a closed form from Garside and Al-Dibouni [20] given by the following

$$V_{rb} = 0.5\left[A - 0.06\mathrm{Re}_b + \sqrt{(0.06\mathrm{Re}_b)^2 + 0.12\mathrm{Re}_b\,(2B - A) + A^2}\right] \tag{4.21}$$

where

$$A = \alpha_2^{4.14} \tag{4.22}$$

$$B = \begin{cases} 0.8 & \text{if } \alpha_2 \leq 0.85 \\ \alpha_2^{2.656} & \text{if } \alpha_2 > 0.85 \end{cases} \tag{4.23}$$

Also, where the bubble Reynolds number is given by the following definition

$$\mathrm{Re}_b = \frac{\rho_2\,|\mathbf{U}_1 - \mathbf{U}_2|\,D_b}{\mu_2} \tag{4.24}$$

and the C_d drag coefficient is defined by the following single sphere drag function from Dalla Valle [62], which is one of the simplest expressions, out of the many possibilities, for this quantity.

$$C_d\left(\frac{\mathrm{Re}_b}{V_{rb}}\right) = \left(0.63 + \frac{4.8}{\sqrt{\frac{\mathrm{Re}_b}{V_{rb}}}}\right)^2 \tag{4.25}$$

4.1.8 Wen & Yu Drag Model

This model was developed by Wen & Yu [65] and is again only valid for solid particles. There are many different implementations that can be found in literature. In particular Rushce

[49] and the CFX Theory Guide [6] have the improved version of this model that was done by Gidaspow where there is a slight discrepancy in the exponent of the liquid phase volume fraction. The original form of the drag coefficient model is given by the following

$$C_d = \max\left(\frac{24}{\mathrm{Re}_b}\left(1.0+0.15\mathrm{Re}_b^{0.687}\right), 0.44\right)\alpha_2^{-2.65} \tag{4.26}$$

where the bubble Reynolds number is given by the following definition

$$\mathrm{Re}_b = \frac{\rho_2 \left|\mathbf{U}_1 - \mathbf{U}_2\right| D_b}{\mu_2} \tag{4.27}$$

The different recommended values for the liquid phase or continuous fluid void fraction α_2 are listed below.

- CFX [6]- α_2^e where $e = -1.65$
- Rusche [49] - α_2^e where $e = -1.7$
- Original Formulation [65] - α_2^e where $e = -2.65$

4.1.9 Tomiyama Drag Model

The Tomiyama drag formulation was built for systems involving bubbles specifically. It has the benefits of being applicable over a wider range of conditions while also accounting for varying degrees of contamination of the system [60, 61]. According to Gilman [24], the Tomiyama model is typically used for a drag model when simulating flow boiling and the contaminated drag coefficient correlation is employed since most experiments do not use liquid of high purity. The model is given by the following,

$$C_d = \max\left(\frac{24}{\mathrm{Re}_b}\left(1.0+0.15\mathrm{Re}_b^{0.687}\right), \frac{8\mathrm{Eo}}{3(\mathrm{Eo}+4)}\right) \tag{4.28}$$

where the bubble Reynolds number is given by the following definition

$$\mathrm{Re}_b = \frac{\rho_2 \left|\mathbf{U}_1 - \mathbf{U}_2\right| D_b}{\mu_2} \tag{4.29}$$

and the Eotvos number is given by the following definition

$$\mathrm{Eo} = \frac{\left(\rho_2 - \rho_1\right) g\, D_b^2}{\sigma} \tag{4.30}$$

4.2 Interfacial Lift Models

According to Ghione [21], the lift force plays an important role on the radial distribution of the void fraction. The lift force consists of a lateral force acting on bubbles that can push bubbles towards the wall (positive lift force) or push bubbles towards the pipe or domain centerline (negative lift force). The sign of the lift force or direction of "pushing" depends on the bubble size or mean Sauter diameter of the bubble. The following is the formulation of the lift force interfacial term in the momentum equations

$$\mathbf{M}_1^{lift} = -\mathbf{M}_2^{lift} = -C_l\, \rho_2\, \alpha_1\, \mathbf{U}_r \times \nabla \times \mathbf{U}_2 \tag{4.31}$$

For a spherical bubble, the lift coefficient C_l should always be positive so that the lift force acts towards the pipe wall. This phenomena can be explained by remembering for viscous flow there is a non-uniform / non-constant pressure gradient / distribution over the bubble surface [40]. In fact assuming a spherical solid particle rising in a pipe, the relative velocity between the two phases is larger at the side with the lower liquid velocity (at the side closer to the wall when considering a turbulent liquid velocity profile) which causes a lower pressure at the same side and that pushes the bubbles towards the pipe wall. For deformed larger bubbles more complicated phenomena arises and an inversion of sign for the lift coefficient C_l is observed in experiments. Studies that have been performed in order to explain this phenomena and explanations have been related to the deformed bubble wake and the corresponding vorticity generated at the bubble surface [40]. However, this phenomena is still not well understood and research and development of better models is on-going with this topic.

4.2.1 Constant Lift Model

This model is used to test the functionality and stability / sensitivity of the lift force model in the solver. The lift coefficient C_l is user defined and constant.

4.2.2 Rusche Lift Model

This model was developed by Rusche [49] and its formulation depends directly on the void fraction; however, it was deduced from a very small data set so that the extension and usage for a wide variety of flow conditions is of doubtful certainty. Furthermore, this formulation leads to an always positive lift coefficient which is contrary to experimental findings on systems containing large bubble sizes. The correlation is given by the following

$$C_l = 6.51 \times 10^{-4} \alpha_1^{-1.2} \tag{4.32}$$

4.2.3 Tomiyama Lift Model

Tomiyama [59] developed the following lift coefficient correlation.

$$C_l = \begin{cases} \min\left(0.288 \tanh\left(0.121 \mathrm{Re}_b\right), f\left(\mathrm{Eo}_d\right)\right) & \text{if } \mathrm{Eo}_d < 4 \\ f\left(\mathrm{Eo}_d\right) & \text{if } 4 < \mathrm{Eo}_d < 10 \\ -0.27 & \text{if } \mathrm{Eo}_d > 10 \end{cases} \tag{4.33}$$

where the bubble Reynolds number is given by the following definition

$$\mathrm{Re}_b = \frac{\rho_2 \left|\mathbf{U}_1 - \mathbf{U}_2\right| D_b}{\mu_2} \tag{4.34}$$

and where the Eotvos number Eo_d is based on the Wellek [2] horizontal diameter of the bubble D_h

$$\mathrm{Eo} = \frac{\left(\rho_2 - \rho_1\right) g D_b^2}{\sigma} \tag{4.35}$$

$$D_h = D_b \left(1.0 + 0.163 \mathrm{Eo}^{0.757}\right)^{\frac{1}{3}} \tag{4.36}$$

$$\mathrm{Eo}_d = \frac{\left(\rho_2 - \rho_1\right) g D_h^2}{\sigma} \tag{4.37}$$

In this formulation the lift coefficient changes sign at a mean Sauter diameter, D_b, of $D_b > 5.8$ mm, so that large bubbles are moved towards the centerline as shown in experiments. This model was obtained by fitting experimental data on single bubbles in a laminar shear flow with $3.7 < Re < 210$ (e.g. very low Reynolds number or low speed flow) using a solution of glycerol-water (e.g. a highly viscous system. This models use with high Reynolds number

flows with water-air solutions means the validity, is not guaranteed. However, in [40] Lucas states that this correlation leads to satisfactory results if compared with experiments.

4.3 Interfacial Wall Lubrication Models

The interfacial wall lubrication force was first proposed by Antal et al. [7]. This force is used to predict the near-wall peak of void fraction. Experimentally it was found that the void fraction is often concentrated close to the wall but not directly touching the wall (e.g. wall-peaked void fraction distribution). The use of the wall force allows a good prediction of the experimental results while avoiding the concentration of all bubbles right on the wall as highlighted by Rzehak [50]. According to Frank [18] the implemented model for wall lubrication force is given by the following

$$\mathbf{M}_1^{wall} = -\mathbf{M}_2^{wall} = C_w \rho_2 \alpha_1 |\mathbf{U}_r - (\mathbf{U}_r \cdot \mathbf{n}_w)\mathbf{n}_w|^2 (-\mathbf{n}_w) \tag{4.38}$$

where $\mathbf{n}_w$ is the vector normal to the wall and $\mathbf{U}_r - (\mathbf{U}_r \cdot \mathbf{n}_w)\mathbf{n}_w$ is the projection of the relative velocity parallel to the wall. The wall lubrication coefficient depends on the distance to the wall and should be always positive so that the bubbles are pushed away from the wall.

4.3.1 Constant Wall Lubrication Model

This model is used to test the functionality and stability / sensitivity of the wall lubrication force model in the solver. The term C_{wl} is user defined and then the wall lubrication coefficient is defined using the following constant value of C_{wl}

$$C_w = \frac{1}{2} C_{wl} D_b \left(\frac{1}{y_w^2} - \frac{1}{\left(D_{pipe} - y_w\right)^2} \right) \tag{4.39}$$

4.3.2 Antal Wall Lubrication Model

This model was developed by Antal et al. [7] to model the wall lubrication force and it has the following form for the wall lubrication coefficient C_{wl}

$$C_w = \max\left(0, \frac{C_{w1}}{D_b} + \frac{C_{w2}}{y_w}\right) \tag{4.40}$$

where the coefficients have the following values $C_{w1} = -0.01$ and $C_{w2} = 0.05$. This force is only active in a very thing layer adjacent to the wall; it is only active up to a cut off distance of

$$y_w \leq -\left(\frac{C_{w2}}{C_{w1}}\right) D_b \tag{4.41}$$

Therefore, for the default values the force only acts in a region of $y_w \leq 5D_b$ which means that for larger domains and small bubbles a fine mesh is required when using this model.

4.3.3 Frank Wall Lubrication Model

This model was developed by Frank [18] and it has the following form

$$C_w = C_{wl} \max\left(0, \frac{1}{C_{wl}} \frac{1 - \frac{y_w}{C_{wc} D_b}}{C_{wd}\, y_w \left(\frac{y_w}{C_{wc} D_b}\right)^{p-1}}\right) \tag{4.42}$$

where the coefficients have the following values $C_{wc} = 10.0$, $C_{wd} = 6.8$, $p = 1.7$, and C_{wl} is defined the same way as the Tomiyama Model.

$$C_{wl} = \begin{cases} 0.47 & \text{if Eo} < 1 \\ \exp(-0.933\,\text{Eo} + 0.179) & \text{if } 1 < \text{Eo} < 5 \\ 0.00599\,\text{Eo} - 0.0187 & \text{if } 5 < \text{Eo} < 33 \\ 0.179 & \text{if Eo} > 33 \end{cases} \tag{4.43}$$

where the Eotvos number is calculated by the following

$$\text{Eo} = \frac{\left(\rho_2 - \rho_1\right) g\, D_b^2}{\sigma} \tag{4.44}$$

4.3.4 Hosokawa Wall Lubrication Model

This correlation for the wall lubrication coefficient is given in [29] and was developed when Hosokawa investigated a larger range of Morton numbers always with glycerol-water solutions, and deduced the following form for the wall lubrication coefficient C_{wl}

$$C_{wl} = 0.0217\,\text{Eo} \tag{4.45}$$

where the Eotvos number is calculated by the following

$$\mathrm{Eo} = \frac{\left(\rho_2 - \rho_1\right) g\, D_b^2}{\sigma} \tag{4.46}$$

According to Rzehak [50] this model shows better performance in modeling air-water flows compared with the Tomiyama wall lubrication force model.

4.3.5 Tomiyama Wall Lubrication Model

Tomiyama [59] developed this correlation for the wall lubrication coefficient. It has the following form

$$C_w = \frac{1}{2} C_{wl}\, D_b \left(\frac{1}{y_w^2} - \frac{1}{\left(D_{pipe} - y_w\right)^2} \right) \tag{4.47}$$

where

$$C_{wl} = \begin{cases} 0.47 & \text{if } \mathrm{Eo} < 1 \\ \exp\left(-0.933\,\mathrm{Eo} + 0.179\right) & \text{if } 1 < \mathrm{Eo} < 5 \\ 0.00599\,\mathrm{Eo} - 0.0187 & \text{if } 5 < \mathrm{Eo} < 33 \\ 0.179 & \text{if } \mathrm{Eo} > 33 \end{cases} \tag{4.48}$$

where the Eotvos number is calculated as follows

$$\mathrm{Eo} = \frac{\left(\rho_2 - \rho_1\right) g\, D_b^2}{\sigma} \tag{4.49}$$

This formulation is based on experimental results for single bubbles in laminar flow of a glycerol-water solution [50]. The Morton number, given in the following, in the experiments was equal to $\log_{10} Mo = -2.8$ while the range of interest for many air-water systems is around $\log_{10} Mo = -10.6$.

$$\mathrm{Mo} = \frac{g\, \mu_2^4 \left(\rho_2 - \rho_1\right)}{\rho_2^2\, \sigma^3} \tag{4.50}$$

Therefore, the applicability of this model cannot be guaranteed since it can be out of the range of its original design. However, it is also important to note that this model is one of the most widely used models in two-phase flow CFD simulations as it has proved to be efficient in many different works.

4.4 Interfacial Turbulence Dispersion Models

The turbulence dispersion force accounts for the turbulent fluctuations of liquid velocity and the effect that has on the gas bubbles. This force influences the sharpness of the wall peak of the void fraction. For example, a reduction in the turbulence dispersion force will lead to a sharper near-wall peak of the void fraction distribution and vice versa. The characterizing feature of this force is that it is proportional to the void fraction gradient. Considering this, according to Ghione [21], it could generate unstable results. For this force there is no uniformly suggested formulation for its implementation into the momentum equations, thus the following just shows that the relationship between the two phases turbulence dispersion force is equal and opposite.

$$\mathbf{M}_1^{tdisp} = -\mathbf{M}_2^{tdisp} \tag{4.51}$$

4.4.1 Burns Turbulence Dispersion Model

Burns [57] derived the following expression for the turbulence dispersion force through a favre averaging of the drag force. It has the following form

$$\mathbf{M}_1^{tdisp} = -\mathbf{M}_2^{tdisp} = -\frac{3}{4}\frac{\rho_2\,\nu_2^t}{D_b\,\sigma_t}\,|\mathbf{U}_r|\,\alpha_1\left(\frac{1}{\alpha_1}+\frac{1}{\alpha_2}\right)\nabla\alpha_1 \tag{4.52}$$

where $\sigma_t = 0.9$ but is user defined, and C_d is the drag coefficient that corresponds with the model used during the simulations. This form can be simplified into the following form

$$\mathbf{M}_1^{tdisp} = -\mathbf{M}_2^{tdisp} = -\frac{3}{4}\frac{\rho_2\,\nu_2^t}{D_b\,\sigma_t}\,|\mathbf{U}_r|\left(\frac{1}{1-\alpha_1}\right)\nabla\alpha_1 \tag{4.53}$$

4.4.2 Gosman Turbulence Dispersion Model

This model was developed by Gosman [25] and it has the following form.

$$\mathbf{M}_1^{tdisp} = -\mathbf{M}_2^{tdisp} = -\frac{3}{4}\frac{\rho_2\,\nu_2^t}{D_b\,\sigma_t}\,|\mathbf{U}_r|\,\nabla\alpha_1 \tag{4.54}$$

where ν_2^t is the turbulent viscosity and the parameter σ_t is a modeling parameter which Ghione [21] takes to be 0.9. Also, according to Ghione [21], the drag coefficient C_d is calcu-

lated using the Schiller & Naumann drag model given by the following

$$C_d = \max\left(\frac{24}{\mathrm{Re}_b}\left(1.0 + 0.15\mathrm{Re}_b^{0.687}\right), 0.44\right) \tag{4.55}$$

where the bubble Reynolds number is given by the following definition

$$\mathrm{Re}_b = \frac{\rho_2 \left|\mathbf{U}_1 - \mathbf{U}_2\right| D_b}{\mu_2} \tag{4.56}$$

4.4.3 Lopez De Bertodano Turbulence Dispersion Model

This model was developed at RPI by Lopez de Bertodano [9] and has the following form.

$$\mathbf{M}_1^{tdisp} = -\mathbf{M}_2^{tdisp} = -\rho_2 C_{td} k_2 \nabla \alpha_1 \tag{4.57}$$

where k_2 is the continuous or liquid phase turbulent kinetic energy and the turbulence dispersion coefficient C_{td} is user defined and has a typical / default setting of 1.0. This model is one of the simplest available turbulent dispersion force models and also, fairly stable in its performance according to Ghione [21].

4.5 Interfacial Virtual Mass Models

The virtual mass or added mass force represents the inertia added to the system due to the fact that a accelerating or deccelerating bubble must move the surrounding fluids as it moves through it. The form of its implementation in the momentum equation is given by the following

$$\mathbf{M}_1^{vmass} = -\mathbf{M}_2^{vmass} = -C_{vm} \rho_2 \alpha_1 \left(\frac{D(\mathbf{U}_1)}{Dt} - \frac{D(\mathbf{U}_2)}{Dt}\right) \tag{4.58}$$

It should be noted that according to [21] the virtual mass force hass little influence on the final solution of steady state problems (e.g. fully developed flows) because the acceleration terms trend towards zero. However, it is useful for prediction of more exact / accurate transient flow evolutions and can also have a stabilizing effect on the overall solution.

4.5.1 Constant Virtual Mass Model

This model is used to test the functionality and stability / sensitivity of the virtual mass force model in the solver. The virtual mass coefficient C_{vm} is user defined, but has a typical value of 0.5.

Chapter 5

INTERFACIAL DIAMETER CLOSURE MODELS

The interfacial diameter closure models account for modeling the diameter of the dispersed or vapor phase in the bulk of the flow.

5.1 Constant Diameter Model

The simplest model is to set the dispersed phase or bubble diameter, D_b, to be a constant user-definable value. This model is used for simple problems where there is not a large variation in bubble size or it can be used to test the functionality and stability / sensitivity of the solver to variations in bubble diameter size.

5.2 Thermal Diameter Model

The next model is using a thermal diameter model. This model is given by the following form

$$D_b(T_{sub}) = \begin{cases} D_{min} & T_{sub} < T_{min} \\ \frac{D_{min}(T_{sub}-T_{max})+D_{max}(T_{min}-T_{sub})}{T_{min}-T_{max}} & T_{min} < T_{sub} < T_{max} \\ D_{max} & T_{sub} > T_{max} \end{cases} \tag{5.1}$$

This model employs user-definable maximum and minimum diameters, D_{max} and D_{min} respectively, that are related to user-definable maximum and minimum temperatures of

sub-cooling, T_{max} and T_{min} respectively and uses linear interpolation when the sub-cooling is between the maximum and minimum temperatures.

5.3 Iso-thermal Diameter Model

The third diameter closure model employed in our solver is the iso-thermal diameter model. This model is given by the following formulation,

$$D_b = D_{ref}\left(\frac{p_{ref}}{p}\right)^{\frac{1}{3}} \tag{5.2}$$

This formulation bases the bubble diameter off of the pressure using user-definable parameters for reference pressure, p_{ref} and diameter, D_{ref}.

5.4 Interfacial Area Concentration Model

The fourth model option, and most complicated, uses the interfacial area concentration transport equation developed by Hibiki & Ishii [27] to model the evolution of interfacial area concentration in space and time. This model takes into account the convection, condensation & expansion due to compressibility of the interfacial area concentration. It can also take into account the break-up of bubbles, coalescence of bubbles and nucleation (e.g. evaporation) of bubbles through the use of addittional closure models. The interfacial area concentration corresponds to the area of the gas / dispersed phase bubbles per unit volume and for spherical bubbles can be defined as the following,

$$A_{i,1} = \frac{6\,\alpha_1}{D_b} \tag{5.3}$$

where D_b is the mean Sauter bubble diameter. The interfacial area concentration transport equation is used to evaluate the mean Sauter bubble diameter that is used in the calculation of the drag, lift, and turbulent dispersion forces and has the following form,

$$\frac{\partial\left(A_{i,1}\right)}{\partial t} + \nabla\cdot\left(A_{i,1}\mathbf{U}_1\right) = \frac{2}{3}\frac{A_{i,1}}{\alpha_1}\left(\frac{\partial\left(\alpha_1\right)}{\partial t} + \nabla\cdot\left(\alpha_1\mathbf{U}_1\right)\right) + \phi_{BK} + \phi_{NUC} + \phi_{CO} \tag{5.4}$$

where after substituting the continuity equation for the first term on the r.h.s. you get the following,

$$\frac{\partial\left(A_{i,1}\right)}{\partial t}+\nabla\cdot\left(A_{i,1}\mathbf{U}_1\right)=\frac{2}{3}\frac{A_{i,1}}{\alpha_1}\left(\frac{\Gamma_{12}-\Gamma_{21}}{\rho_1}-\frac{\alpha_1}{\rho_1}\frac{D\left(\rho_1\right)}{Dt}\right)+\phi_{BK}+\phi_{NUC}+\phi_{CO} \tag{5.5}$$

where the volumetric mass transfer term for the dispersed phase is given by,

$$\Gamma_1=\Gamma_{12}-\Gamma_{21} \tag{5.6}$$

and the substantial derivative of the dispersed phase density is given by,

$$\frac{D\left(\rho_1\right)}{Dt}=\frac{\partial\left(\rho_1\right)}{\partial t}+\mathbf{U}_1\cdot\nabla\rho_1 \tag{5.7}$$

This equation was developed by Hibiki & Ishii [27] for a one-dimensional geometry and one-group bubble diameter, and it was extended to three-dimensional geometry. The first term on the r.h.s. of the equation refers to the contribution of phase change (e.g. condensation and evaporation) and expansion due to a change in pressure. The last three terms are ϕ_{BK} which a sink term that accounts for the break-up of bubbles due to turbulent impacts, ϕ_{CO} which a source term that accounts for the coalescence of bubbles due to random collisions, and ϕ_{NUC} which is the source term that accounts for nucleate boiling when running sub-cooled boiling test cases. There are several models used to numerically estimate the break-up and coalescence terms and one will be described in detail in the following sections. Hibiki & Ishii [27] stated that bubble coalescence due to wake entrainment is unlikely to occur in bubbly flow, as it plays an important role between pairs of large cap bubbles when the flow regimes is near the bubbly to slug flow transition boundary, and in the slug flow regime when the fluid is sufficiently viscous to maintain a laminar bubble wake. Alali [4] states that for highly turbulent flows, the bubble captured in the wake region will easily leave it before any coalescence can take place. Hence, Hibiki & Ishii focused on the development of models for breakup due to turbulent impact and for coalescence due to random collisions driven by liquid turbulence and thus those will also be the only models implemented here as well.

5.4.1 Break-up Source Term

This is the source term in the interfacial area concentration transport equation that deals with the breaking up of bubbles into smaller bubbles due to a turbulent eddy collision. Generally speaking, the models are of the following form

$$\phi_{BK} = -12\,\pi \left(\frac{\alpha_1}{A_{i,1}} \right)^2 f_{BK}\, N\, \eta_{BK} \tag{5.8}$$

where f_{BK} is the bubble-eddy collision frequency which depends on the Weber number which is the ratio of the turbulent inertial energy to surface energy and given by the following definition

$$\mathrm{We} = \frac{\rho_2\, U_{rms}^2\, D_b}{\sigma} \tag{5.9}$$

where the velocity $U_{rms} = (\epsilon_2\, D_b)^{\frac{1}{3}}$ is the root-mean-square velocity difference between the two points separated by a length D_b. This term works off of the balance between the cohesive and disruptive forces [63]. Therefore, bubble breakup caused by turbulent eddie impacts occurs when the turbulent eddies have enough energy to overcome the surface tension force. Also, the term η_{BK} is called the break-up efficiency which is defined as the probability for a bubble to collide with an eddy that has sufficient energy to break the bubble. Finally, the term N represents the bubble number density.

5.4.1.1 Hibiki & Ishii Break-up Model

The Hibiki & Ishii [27] break-up model was developed on adiabatic air-water bubbly flow experiments and is of the following form.

$$\phi_{BK} = -\Gamma_B \frac{\alpha_1\,(1-\alpha_1)\,\epsilon_2^{\frac{1}{3}}}{d_b^{\frac{5}{3}}\,(\alpha_{max}-\alpha_1)} \exp\left(-K_B \frac{\sigma}{D_b^{\frac{5}{3}}\,\rho_2\,\epsilon_2^{\frac{2}{3}}} \right) \tag{5.10}$$

where the term α_{max} has the following values

- $\alpha_{max} = 0.74$ - from [21, 27].
- $\alpha_{max} = 0.52$ - from [3, 4].

and Γ_B has the following constant values

- $\Gamma_B = 0.0209$ - from [21].
- $\Gamma_B = 0.00733$ - from [4].

or the term can have the following functional form

$$\Gamma_B = 5.02 \times 10^{-8} \alpha_1 \tilde{\epsilon} \tag{5.11}$$

where

$$\tilde{\epsilon} = \frac{\epsilon_2 \mathrm{Lo}^4}{\nu_2^3} \tag{5.12}$$

and

$$\mathrm{Lo} = \sqrt{\frac{\sigma}{g\left(\rho_2 - \rho_1\right)}} \tag{5.13}$$

Finally, K_B has the following constant values

- $K_B = 1.59$ - from [21].
- $K_B = 1.37$ - from [4].

5.4.1.2 Wu et al. Break-up Model

The Wu et al. model [1] for the break-up source term of the interfacial area concentration equation is given by the following,

$$\phi_{BK} = \frac{6\alpha_1 \epsilon_2^{\frac{1}{3}} \Gamma_B}{\pi D_b^{\frac{11}{3}} \alpha_{max}^{\frac{1}{3}} \left(\alpha_{max}^{\frac{1}{3}} - \alpha_1^{\frac{1}{3}}\right)} \left[1 - \frac{\mathrm{We}_{cr}}{\mathrm{We}}\right] \exp\left(-\frac{\mathrm{We}_{cr}}{\mathrm{We}}\right) \tag{5.14}$$

where the critical Weber number is defined as $\mathrm{We}_{cr} = 2.0$, the maximum void fraction is defined as $\alpha_{max} = 0.8$, $\Gamma_B = 0.18$ and the Weber number which is the ratio of the turbulent inertial energy to surface energy and given by the following definition,

$$\mathrm{We} = \frac{\rho_2 U_{rms}^2 D_b}{\sigma} \tag{5.15}$$

5.4.1.3 Yao & Morel Break-up Model

The Yao & Morel model [67] for the break-up source term of the interfacial area concentration equation is given by the following,

$$\phi_{BK} = \frac{\alpha_1 \epsilon_2^{\frac{1}{3}} \Gamma_B}{D_b^{\frac{11}{3}}} \left[\frac{(1-\alpha_1)}{1+K_B(1-\alpha_1)\sqrt{\frac{\mathrm{We}}{\mathrm{We}_{cr}}}} \right] \exp\left(-\frac{\mathrm{We}_{cr}}{\mathrm{We}}\right) \tag{5.16}$$

where the critical Weber number is defined as $\mathrm{We}_{cr} = 1.24$, $K_B = 0.42$, $\Gamma_B = 1.6$ and the Weber number which is the ratio of the turbulent inertial energy to surface energy and given by the following definition,

$$\mathrm{We} = \frac{\rho_2 U_{rms}^2 D_b}{\sigma} \tag{5.17}$$

5.4.1.4 Nguyen et al. Break-up Model

The Nguyen et al. model [43] for the break-up source term of the interfacial area concentration equation is given by the following,

$$\phi_{BK} = \frac{\epsilon_2^{\frac{1}{3}}}{D_b^{\frac{11}{3}}} \left[\frac{\Gamma_B(1-\alpha_1)}{1+K_{B1}(1-\alpha_1)\sqrt{\frac{\mathrm{We}}{\mathrm{We}_{cr}}}} \right] \exp\left(-\frac{K_{B2}}{(1-c_3)}\frac{2}{\mathrm{We}}\right) \tag{5.18}$$

where the constants are defined as $K_{B1} = 0.42$, $K_{B1} = 1.59$, $\Gamma_B = 1.6$ and the Weber number which is the ratio of the turbulent inertial energy to surface energy and given by the following definition,

$$\mathrm{We} = \frac{\rho_2 U_{rms}^2 D_b}{\sigma} \tag{5.19}$$

5.4.2 Coalescence Source Term

This is the source term in the interfacial area concentration transport equation that deals with the joining / coalescence of bubbles into larger bubbles due to a random turbulent bubble-to-bubble collisions. Generally speaking, the models are of the following form

$$\phi_{CO} = -12\,\pi \left(\frac{\alpha_1}{A_{i,1}}\right)^2 f_{CO}\, N\, \eta_{CO} \tag{5.20}$$

where f_{CO} is the bubble-to-bubble collision frequency which is assumed to only happen between neighboring bubbles. This term works off of the probability that the bubbles are traveling so a collision can occur and also that they have sufficiently low speed at the time of collision not to just bounce off of each other [4]. Therefore, bubble coalescence caused by turbulent impacts occurs when the turbulent eddies have low enough energy to avoid bouncing back or break-up. Also, the term η_{CO} is called the coalescence efficiency which is defined as the probability for a bubble to collide with another bubble that has sufficiently small energy to not break the bubble or bounce off. Finally, the term N is the bubble number density.

5.4.2.1 Hibiki & Ishii Coalescence Model

The Hibiki & Ishii [27] coalescence model was developed on adiabatic air-water bubbly flow experiments and is of the following form.

$$\phi_{CO} = -\Gamma_C \frac{\alpha_1^2 \epsilon_2^{\frac{1}{3}}}{D_b^{\frac{5}{3}} (\alpha_{max} - \alpha_1)} \exp\left(-K_C \frac{D_b^{\frac{5}{6}} \rho_2^{\frac{1}{2}} \epsilon_2^{\frac{1}{3}}}{\sigma^{\frac{1}{2}}} \right) \tag{5.21}$$

where the term α_{max} has the following values

- $\alpha_{max} = 0.74$ - from [21, 27].
- $\alpha_{max} = 0.52$ - from [3, 4].

and Γ_C has the following constant values

- $\Gamma_C = 0.0314$ - from [21].
- $\Gamma_C = 0.005236$ - from [4].

or the term can have the following functional form

$$\Gamma_C = 1.82 \times 10^{-8} \alpha_1 \tilde{\epsilon} \tag{5.22}$$

where

$$\tilde{\epsilon} = \frac{\epsilon_2 \mathrm{Lo}^4}{\nu_2^3} \tag{5.23}$$

and

$$\mathrm{Lo} = \sqrt{\frac{\sigma}{g\left(\rho_2 - \rho_1\right)}} \tag{5.24}$$

Finally, K_C has a constant value of 1.29 [4, 21].

5.4.2.2 Wu et al. Coalescence Model

The Wu et al. model [1] for the coalescence source term of the interfacial area concentration equation is given by the following,

$$\phi_{CO} = \frac{36\alpha_1 \epsilon_2^{\frac{1}{3}} \Gamma_C}{\pi^2 D_b^{\frac{11}{3}} \alpha_{max}^{\frac{1}{3}} \left(\alpha_{max}^{\frac{1}{3}} - \alpha_1^{\frac{1}{3}}\right)} \left[1 - \exp\left(-K_C \frac{\alpha_{max}^{\frac{1}{3}} \alpha_1^{\frac{1}{3}}}{\alpha_{max}^{\frac{1}{3}} - \alpha_1^{\frac{1}{3}}}\right)\right] \tag{5.25}$$

where the coefficients are defined as $K_C = 3.0$, the maximum void fraction $\alpha_{max} = 0.8$ and $\Gamma_C = 0.0565$.

5.4.2.3 Yao & Morel Coalescence Model

The Yao & Morel model [67] for the coalescence source term of the interfacial area concentration equation is given by the following,

$$\phi_{CO} = \frac{\epsilon_2^{\frac{1}{3}} \Gamma_C}{D_b^{\frac{11}{3}}} \left[\frac{\alpha_1^2 \alpha_{max}^{\frac{1}{3}}}{\left(\alpha_{max}^{\frac{1}{3}} - \alpha_1^{\frac{1}{3}}\right) + K_{C1} \alpha_1 \alpha_{max}^{\frac{1}{3}} \sqrt{\frac{\mathrm{We}}{\mathrm{We}_{cr}}}}\right] \exp\left(-K_{C2} \sqrt{\frac{\mathrm{We}_{cr}}{\mathrm{We}}}\right) \tag{5.26}$$

where the critical Weber number is defined as $\mathrm{We}_{cr} = 1.24$, the maximum void fraction $\alpha_{max} = 0.52$, $K_{C1} = 1.922$, $K_{C2} = 1.017$, $\Gamma_C = 2.86$ and the Weber number which is the ratio of the turbulent inertial energy to surface energy and given by the following definition,

$$\mathrm{We} = \frac{\rho_2 U_{rms}^2 D_b}{\sigma} \tag{5.27}$$

5.4.2.4 Nguyen et al. Coalescence Model

The Nguyen et al. model [43] for the coalescence source term of the interfacial area concentration equation is given by the following,

$$\phi_{CO} = \frac{\epsilon_2^{\frac{1}{3}}}{D_b^{\frac{11}{3}}} \left[\frac{\Gamma_C \alpha_1^2 \alpha_{max}^{\frac{1}{3}}}{\left(\alpha_{max}^{\frac{1}{3}} - \alpha_1^{\frac{1}{3}}\right) + K_{C1}\alpha_1 \alpha_{max}^{\frac{1}{3}} \sqrt{\frac{\mathrm{We}}{\mathrm{We}_{cr}}}} \right] \exp\left(-\frac{K_{C2}}{c^{\frac{2}{3}}} \sqrt{\frac{\mathrm{We}}{2}} \right) \tag{5.28}$$

where the critical Weber number is defined as $\mathrm{We}_{cr} = 1.24$, the maximum void fraction $\alpha_{max} = 0.52$, $K_{C1} = 1.922$, $K_{C2} = 0.913$, $\Gamma_C = 2.86$ and the Weber number which is the ratio of the turbulent inertial energy to surface energy and given by the following definition,

$$\mathrm{We} = \frac{\rho_2 U_{rms}^2 D_b}{\sigma} \tag{5.29}$$

and

$$c = \frac{11}{3} \sqrt{\frac{2.24(1-c_3)\left(c_1^{\frac{2}{3}} - c_2^{\frac{2}{3}}\right)}{\left(c_2^{-3} - c_1^{-3}\right)}} \tag{5.30}$$

Chapter 6

PHASE CHANGE CLOSURE MODELS

This section is going to cover a discussion of the present state of the phase change closure models. The phase change closure models consist of methods to calculate the interfacial heat transfer, condensation mass transfer rate, evaporation mass transfer rate, wall heat flux, and interfacial area concentration nucleation source terms.

6.1 Interfacial Heat Transfer Coefficient Closure Models

The interfacial heat transfer takes into account the heat transfer between the phases in the bulk of the flow domain and is dependent on the relative velocity, interfacial area, and thermo-physical properties of both phases. It is modeled by using a closure model for the interfacial heat transfer coefficient and the general form involves the estimation of a Nusselt number and is given by the following,

$$h_{c,21} = \frac{\mathrm{Nu}\lambda_2}{D_b} \tag{6.1}$$

In the solver there are three options that are given in this section to estimate the Nusselt number, Nu.

6.1.1 Ranz & Marshall Model

Ranz & Marshall [47, 48] model is of the following form,

$$\mathrm{Nu} = 2 + 0.6\mathrm{Re}_b^{0.5}\mathrm{Pr}_2^{0.3} \tag{6.2}$$

where Re_b is the relative Reynolds number based on the dispersed or vapor phase (k=1) diameter and the relative velocity, $|\mathbf{U}_1 - \mathbf{U}_2|$, given in the following relationship,

$$\mathrm{Re}_b = \frac{\rho_2 |\mathbf{U}_1 - \mathbf{U}_2| D_b}{\mu_2} \tag{6.3}$$

and the Prandlt number is defined as follows,

$$\mathrm{Pr}_2 = \frac{C_{p,2}\mu_2}{\lambda_2} \tag{6.4}$$

6.1.2 Chen & Mayinger Model

According to [24], the Chen & Mayinger model [11] is often used in place of Ranz & Marshall's model in the standard cases because it was developed using a larger range of liquid Prandtl numbers, $2 < \mathrm{Pr}_2 < 15$, and Jakob numbers, $1 < \mathrm{Ja} < 120$, and is more applicable for higher pressure cases. The definition of the Jakob number, Ja, is shown in the following,

$$\mathrm{Ja} = \frac{\rho_2 C_{p,2} \Delta T_{sub}}{\rho_1 h_{fg}} \tag{6.5}$$

Chen and Mayinger looked at the heat transfer at the vapor-liquid interface for both departing bubbles and attached bubbles using ethanol, propanol, R113, and water as fluids during the experiments. As discussed previously, the Nusselt number is used to calculate the interfacial heat transfer coefficient, $h_{c,21}$, and the formulation for the Nusselt number model is given by the following,

$$\mathrm{Nu} = 0.185 \mathrm{Re}_b^{0.7} \mathrm{Pr}_2^{0.5} \tag{6.6}$$

where Re_b is the relative Reynolds number based on the dispersed or vapor phase (k=1) diameter and the relative velocity, $|\mathbf{U}_1 - \mathbf{U}_2|$, given in the following relationship,

$$\mathrm{Re}_b = \frac{\rho_2 |\mathbf{U}_1 - \mathbf{U}_2| D_b}{\mu_2} \tag{6.7}$$

and the Prandlt number is defined as follows,

$$\mathrm{Pr}_2 = \frac{C_{p,2}\mu_2}{\lambda_2} \tag{6.8}$$

6.1.3 Wolfert et al. Model

The Wolfert et al. model [66] is different than the two previous implementations as it does not consist of an estimation of the Nusselt number rather it employs a direct model of the interfacial heat transfer coefficient. Assuming the vapor phase bubbles are at saturation, the model is given by the following,

$$h_{c,21} = \rho_2 C_{p,2} \sqrt{\frac{\pi}{4} \frac{|\mathbf{U}_r|}{D_b} \frac{\lambda_2}{\rho_2 C_{p,2}} \frac{1}{1+\frac{\lambda_2^t}{\lambda_2}}} \tag{6.9}$$

6.2 Condensation Closure Model

The condensation closure model accounts for the mass transfer between phase in situations when vapor bubbles, that are created via boiling at the wall, are moved towards the centerline and are surrounded by subcooled liquid water and condense. In the case of subcooled nucleate boiling simulations, condensation is the only possible physical phase change at the interface for cells which are not in direct contact with the wall. The interfacial mass transfer related to condensation of vapor bubbles in the bulk coolant is found as,

$$\Gamma_{21} = \max\left[\frac{h_{c,21}(T_1 - T_2)A_{i,1}}{h_{fg}}, 0\right] \tag{6.10}$$

The interfacial heat transfer coefficient, phase temperature difference, latent heat, and interfacial area concentration are employed to estimate the condensation rate.

6.3 Wall Heat Flux Partitioning Closure Model

This section will deal with the wall heat flux partitioning closure model and all mechanistic boiling models which are related to it. The wall heat flux partitioning model currently employed in the solver is basically just the classic RPI Model [35] extended slightly to include heat transfer to the vapor phase. Subcooled boiling starts when the wall temperature achieves a temperature that is sufficiently large to initiate the activation of wall nucleation sites. This activation temperature is typically a few degrees above the saturation temperature. However, most of the time at this stage the temperature of the fluid / liquid in the vicinity

of the heated walls is still well below the saturation temperature for the given pressure of the system, hence the naming convention of subcooled boiling regime.

The process of evaporation along the heated walls starts in the microscopic cavities and crevices that are always present on solid surfaces. The liquid / fluid phase becomes supersaturated locally in these crevices / deformitites along the solid wall surface (e.g. nucleation sites) and this leads to the growth of vapor bubbles at the site via phase change. The bubbles become detached from the site when they become sufficiently large that external forces (e.g. intertial, gravitational, or turbulent) exceed the surface tension forces that keep them attached to the wall. As the bubbles depart from the wall, they are displaced by superheated liquid in the vicinity of the nucleation sites, after which the nucleation site is free to create another bubble and begin the process all over again. In regions of the wall not affected by bubble formation and growth (e.g. boiling), the wall heat transfer to the liquid is strictly described by single phase convective heat transfer.

It is both clear and been found that the detailed physics of bubble growth is very complex and occurs on a very small length scale in the vicinity of the all. For the purposes of CFD modeling it is unrealistic to model the detailed physics in a phase-average eulerian multi-phase model. On top of that, it is also unrealistic to resolve the small length scales with ultra-fine meshes. The models which are presented in this work are what are referred to as mechanistic models. These models have the aim of representing the important physical sub-processes using engineering correlations. The model is what is called a sub-grid scale model, in the sense that the complex physics is assummed to take place in a vicinity very close to the wall that is smaller than the mesh resolution at the wall.

The first and most well known model of this kind was formulated by Kurul & Podowski (1991) [35] and is generally known as the RPI model. In this model, a number of the sub-models of the overall mechanistic model were taken from correlations originally developed for exploitation in one-dimensional thermo-hydraulic simulation methods. The model can be implemented and run with near-wall distance taking the place of the centerline wall distance in the one-dimensional models. However, this unfortunately leads to results that were strongly mesh dependent (according to [6, 34]).

Egorov & Menter [15] formulated modifications of the one-dimensional corellations with the aim of restoring mesh independence to the solution and results. There are also other methods being developed that employ a different heat flux partitioning scheme, as well as different mechanistic models for the correlations in order to increase accuracy,

range of applicability, and mesh independence. These modifications of the RPI model will also be discussed in the following sections.

6.3.1 Wall Heat Flux Partitioning

One of the fundamental features of the mechanistic model of subcooled boiling is the algorithm for deciding the method of partitioning the wall heat flux amongst the separated physical processes of evaporation and sensible heating of the two phases. In areas of the wall that are not influenced by nucleation sites (i.e. boiling) [6], it is sufficient to consider the wall heat flux as contributing solely to single-phase convective heat transfer. However, in the vicinity of the nucleation sites (i.e. boiling), a portion of the heat contributes to vapor production (i.e. evaporation), and the remainder of the heat contributes to the heating of the liquid phase as it displaces the rising bubbles. This latter process is often referred to as quenching. The mechanistic heat partitioning first splits the wall heat flux into three terms,

- Heat flux to account for the heating of the subcooled liquid
- Heat flux to account for evaporation
- Heat flux to account for the super heating of the vapor

The heat flux to account for the heating of the subcooled liquid is further assumed to be partitioned into two sub-process,

- Heat flux corresponding to single-phase convective heat transfer to the liquid phase
- Heat flux corresponding to heating of the liquid phase as it displaces the rising bubbles along the wall (i.e. quenching)

In the standard model the vapor phase is assumed to be saturated everywhere and no part of the wall heat flux contributes to super heating the vapor phase; however, our model formulation has the ability to take this into account but, the stability of the energy equation is a on-going issue. Therefore, the discussion will be presented in this section but, the actual implementation is always done so in such a way to avoid actual contributions to this term.

The heat partitioning model considers the whole wall surface as being first separated into two fractions,

- Fraction A_f is the total wall area fraction that accounts for heat transfer to the liquid phase and produces boiling

- Fraction $A_g = 1 - A_f$ is the remaining wall surface. This is the wall area fraction that accounts for single-phase convective heat transfer directly to the vapor phase

After the initial partitioning of the wall area, the fraction of the total wall area that accounts for heat transfer to the liquid, A_f, is further divided into two fractions,

- Fraction $A_{f,1\phi}$ is the area fraction for single-phase convective heat transfer to the liquid phase

- Fraction $A_{f,2\phi} = 1 - A_{f,1\phi}$ is the remaining area that accounts for the area influenced by the nucleation sites (i.e. quenching heat transfer) of the fraction of the wall that accounts for the heat transfer to the liquid phase

For the areas of the wall that see single-phase convective heat transfer, the heat flux is modeled using the following relationship,

$$q''_{k,1\phi} = h^{(k)}_{c,1\phi}\left(T_w - T_{k,nw}\right) \tag{6.11}$$

where T_w is the temperature of the solid wall, $T_{k,nw}$ is the temperature of phase k at the wall, and $h^{(k)}_{c,1\phi}$ is the heat transfer coefficient and the index $k = f$ for single-phase convective heat transfer to fluid or continuous phase and $k = g$ for single-phase convective heat transfer to vapor or dispersed phase. The heat transfer coefficient requires closure modeling and it depends on the velocity field and on the near-wall grid cell size [6]. In our solver we currently have two methods of computation of the single-phase convective heat transfer coefficient (given in the following sections), on used by Kurul and Podowski (1991) [35] that models the convective heat transfer coefficient using a one-dimensional Stanton number correlation developed by Anglart [5] and another developed by Egorov and Menter (2004) [15].

The phase change or evapoartion heat flux contribution to the partitioning scheme is formulated using the following,

$$q''_{fg} = \rho_1 f_b N''_a \left(\frac{\pi D^3_{b,w}}{6}\right)\left(h_{1,sat} - h_2\right) \tag{6.12}$$

where $\rho_1 f_b N''_a \left(\frac{\pi D^3_{b,w}}{6}\right)$ is the evapoartion mass transfer rate per unit wall area and $h_{1,sat}$ and h_2 are the enthalpies of the saturated vapor and subcooled liquid respectively. The terms

f_b, N_a'' and $D_{b,w}$ are terms which require closure modeling and will be discussed in detail later in this section. As discussed previously, a part of the heat flux to the liquid occurs between the bubble departure and the next bubble formation at each nucleation site and this additional mechanism of liquid heating is often referred to as quenching. Quenching is modeled using the following formulation,

$$q''_{f,2\phi} = h^{(f)}_{c,2\phi}\left(T_w - T_{f,nw}\right) \tag{6.13}$$

where $h^{(f)}_{c,2\phi}$ is the two-phase (quenching) heat transfer coefficient that requires closure modeling and will be discussed in detail later in the section. The total wall heat flux partitioning closure model currently employed in the solver has the following form,

$$q''_w = A_f\left[A_{f,1}q''_{f,1\phi} + A_{f,2\phi}\left(q''_{f,2\phi} + q''_{fg}\right)\right] + A_g q''_{g,1\phi} \tag{6.14}$$

where $q''_{1\phi}$ is the single-phase force convection heat flux to the liquid, $q''_{f,2\phi}$ is the two-phase (quenching) heat flux, q''_{fg} is the phase change (evaporation) heat flux and $q''_{g,1\phi}$ is the single-phase forced convection heat flux to the vapor. The first and last terms on the r.h.s, of the equation account for being in regions along the heated wall with no boiling which allows heat to be transferred directly to the liquid / vapor through single phase forced convection. The second and third terms on the r.h.s. of the equation account for being in regions along the heated wall with boiling occurring. The quenching component accounts for enhanced heat transfer to the liquid from "cool" liquid coming into contact with the heated wall after bubble departure at the nucleation site, and the phase change / evaporation component accounts for the necessary heat to produce a modeled number of spherical bubbles of a modeled diameter at a modeled frequency with given thermo-physical properties.

It is important to note that the two most important parameters governing the heat partitioning model are the nucleation site density N_a'' and the bubble departure diameter $D_{b,w}$. In the wall-boiling model they are generally correlated to the wall superheat $\Delta T_{sup} = T_w - T_{sat}$ and to the near-wall liquid sub-cooling $\Delta T_{sub} = T_{sat} - T_{2,nw}$, respectively. Currently the method our solver employs to solve this non-linear equation for the wall temperature, which is the only non-modeled unknown in the wall heat flux partitioning scheme, is the bi-section algorithm. This is done because of the ease of implementation and the lack of need for a Jacobian formulation or estimation for each model when employing a newton iteration scheme.

6.3.2 Wall Area Fraction Models

The area fraction values A_f, A_g, $A_{f,1\phi}$ and $A_{f,2\phi}$ play an important role in the heat-partitioning model. They are related to the amount of void fraction near the wall, the nucleation site density per unit wall area and to the influence area of a single bubble forming at the wall nucleation site. The former value is the basic wall dryout area fraction model and is given by the following,

$$A_g = 1 - A_f = \beta^2 \left(3 - 2\beta\right) \tag{6.15}$$

where this model is only employed above a dryout breakpoint and the β term is defined by the following,

$$\beta = \frac{\alpha_1 - \alpha_{dry}}{1 - \alpha_{dry}} \tag{6.16}$$

As mentioned previously, this is employed to specify the amount of heat flux applied at the wall is directed into the vapor convection instead of the convection, quenching, and evaporation of the liquid. Dryout only occurs when the vapor volume fraction near the wall reaches a high enough value that the vapor prevents the liquid from coming into contact with the wall. The point at which this happens is often referred to as the wall dryout breakpoint. The wall dryout breakpoint α_{dry} is often set at a value of 0.9 so that once this vapor volume is reached, heat transfer to the vapor phase occurs and the wall boiling formulation is modified to include this effect. However, our implementation due to stability issues sets the breakpoint at $\alpha_{dry} = 1.0$ so that the model is effectively shut off for the time being until better strategies can be made with regards to stability issues of the dispersed or vapor phase energy equation.

Now, the other area fraction model mentioned previously is related to the nucleation site density per unit wall area and to the influence area of a single bubble format at the wall nucleation site and its “Unlimited” form is given by the following formulation,

$$A_{f,2\phi} = \frac{a\,\pi D_{b,w}^2}{4} N_a'' \tag{6.17}$$

where the bubble influence area factor a will be discussed in the following section. This model has two options, the previous given “Unlimited” formulation and one which is referred to as the “Limited” method that does not take into account the affect of nucleation

sites overlapping and operating out of phase, and is given by the following,

$$A_{f,2\phi} = \min\left(\frac{a\,\pi D_{b,w}^2}{4} N_a'', 1\right) \tag{6.18}$$

where the single-phase liquid convective heat transfer is always limited from below by a small value, so its actual form is the following,

$$A_{f,1\phi} = \min\left(10^{-4}, 1 - A_{f,2\phi}\right) \tag{6.19}$$

6.3.3 Bubble Area Influence Factor Model

In the previous discussion, the influence area of a single bubble forming at the wall nucleation site, is modeled by introducing the bubble departure diameter value $D_{b,w}$, which can generally serve as a length scale of the wall boiling mechanism. According to [6], the RPI model [35] assumes that the diameter of the bubble influence zone is twice as large as the value of $D_{b,w}$, therefore the non-dimensional area fraction of the bubble influence is

$$A_{f,2\phi} = \frac{a\,\pi D_{b,w}^2}{4} N_a'' \tag{6.20}$$

where $a = 4$. However, we left this parameter user modifiable in order to give the ability to change the implementation in the future and see the affects.

6.3.4 Bubble Departure/Detachment Diameter Model

The determination of the bubble detachment diameter is a key characteristic in the modeling of subcooled nucleate boiling. It models the size of the bubble detaching from the heated wall at a nucleation site. The Tolubinksy & Kostanchuk model [58] is given by the following,

$$D_{b,w} = \min\left[D_{b,0}\exp\left(\frac{\Delta T_{sub,f}}{\Delta T_{sub,0}}\right), D_{b,\max}\right] \tag{6.21}$$

The parameters of the model are dimensional ($D_{b,0} = 0.6$[mm], $D_{b,\max} = 1.4$[mm] and $\Delta T_{sub,0} = 45$[°C]) and are chosen to fit pressurized water data [6]. Hence the model is clearly not universal. The exists the possibility for negative liquid subcooling, where it means onset of the bulk boiling, therefore, limiting the bubble departure diameter applies to

this situation and prevents the diameter from growing too high. Note that the model is strongly dependent on a liquid temperature scale [6]. In the original experimental data [58], this was taken as the pipe center-line temperature. Most initial implementations used the cell-center value in near wall cells, however, this proved to give mesh-dependent results. Egorov and Menter [15] restored mesh independence by using the logarithmic form of the wall function to estimate the liquid temperature at a fixed value of $y^+ = 250$. Our solver uses this method but with a user-modifiable value of y^+.

6.3.5 Bubble Departure Frequency Model

During subcooled nucleate boiling the growth of the bubble is controlle by inertial effects and it can be analytically proben the $f_b^2 D_{b,w}$ is constant at a constant wall heat flux [41]. The computation of the evaporation rate requires the frequency of the bubble detachment from the nucleation site. The model adopted by Kurul and Podowski is that due to Cole (1960) [12],

$$f_b = \sqrt{\frac{4}{3}\frac{g\left(\rho_f - \rho_g\right)}{C_D D_{b,w} \rho_f}} \tag{6.22}$$

It can be observed on examination of this formulation that due to its dependence on gravity, this correlation is obviously taken from a study on pool boiling. It is simply estimated as the bubble rise velocity divided by the bubble departure diameter. The drag coefficient factor C_D was taken to be unity by Ceumern-Lindenstjerna (1977) [10] and that is the form that is actually implemented in our solver.

6.3.6 Single-phase Heat Transfer Coefficient Model

As previously discussed, the heat transfer coefficient requires closure modeling and it depends on the velocity field and on the near-wall grid cell size. Kurul and Podowski (1991) [35] modeled the convective heat transfer coefficient using a one-dimensional Stanton number correlation given by the following,

$$h_{c,1\phi}^{(k)} = \mathrm{St}_k \rho_k C_{p,k} ||\mathbf{U}_k|| \tag{6.23}$$

where St_k is the Stanton number for phase k and is linked to the Fanning friction factor, C_f, through the following mono-dimensional correlation,

$$\mathrm{St}_k = \frac{C_f^2}{1 - 1.783\, C_f} \tag{6.24}$$

where the friction factor is calculated through the non-linear realation given by the following,

$$C_f = \frac{1}{\frac{\ln\left(\widetilde{\mathrm{Re}} C_f\right)}{0.435} + 5.05} \tag{6.25}$$

where

$$\widetilde{\mathrm{Re}} = \frac{3.2586 \times 10^{-4} \left|\left| \mathbf{U}_k^b \right|\right|}{\nu_k} \tag{6.26}$$

where $\mathbf{U}_k^b$ represents the bulk velocity of phase k. Egorov and Menter (2004) [15] modeled the convective heat transfer coefficient using a turbulent wall function approach given by the following,

$$h_{c,1\phi}^{(k)} = \frac{\rho_k C_{p,k} \mathbf{U}_{\tau,k}}{T_k^+} \tag{6.27}$$

where $\mathbf{U}_{\tau,k}$ is the friction velocity of phase k and the non-dimensional temperature, T_k^+, for phase k is evalued from the temperature wall function $T^+\left(y^+\right)$ from Kader (1981) [31]. Just to re-iterate, currently the solver does not model any heat transfer to the vapor phase due to instabilities in the vapor phase energy equation because of the large density ratios; therefore, the calculations are indeed performed for both phases but only the liquid phase ($k = 2$ or $k = f$) values are actually used in the calculation process.

6.3.7 Two-phase Heat Transfer Coefficient Model

As discussed in the partitioning of the wall heat flux section of this work, the quenching heat transfer to the liquid phase in the in the area of influence of the nucleation sites requires a modeling of the two-phase heat transfer coefficient related to quenching. This value depends on the waiting time between the bubble departure and the next bubble formation. Using the waiting time, the quenching heat transfer coefficient can be correlated using the following formulation,

$$h_{c,2\phi}^{(f)} = 2 f_b \sqrt{\frac{\rho_2 C_{p,2} t_w \lambda_f}{\pi}} \tag{6.28}$$

This model was developed by Mikic and Rohsenow (1969) [42] and Del Valle and Kenning (1985)[14]. Currently this is the only model employed in our solver.

6.3.8 Nucleation Site Density Models

The nucleation site density model depends mostly on the properties of the wall and the wall superheat, which is defined as the temperature difference between the wall temperature and the saturation temperature of the liquid. The model for wall nucleation site density adopted in the RPI model is that of Lemmert and Chawla (1977) [36] and is given by the following,

$$N_a'' = \left[m \, \Delta T_{sup} \right]^p \tag{6.29}$$

where $m = 210$ and $p = 1.805$. It is important to note that the wall superheat, ΔT_{sup}, in the above equation cannot be negative because it would mean that the wall temperature drops below the saturation temperature. This would indicate that there is no boiling occuring and thus the wall heat flux partitioning scheme would not be used as all wall heat transfer would be directly conveyed to the fluid via the single-phase convection.

Some implementations of this model use a default value of $m = 185$ which gives an an overall correction factor of 0.8. The CFX Theory manual [6] states that Egorov and Menter (2004) [15], conjectured that this was a deliberate alteration by the RPI group, related to the corresponding factor in the bubble waiting time model. Egorov and Menter [15]also reformulated the correlation as follows,

$$N_a'' = N_{ref}'' \left[\frac{\Delta T_{sup}}{\Delta T_{ref}} \right]^p \tag{6.30}$$

where $N_{ref}'' = 0.8 \cdot 9.922 \times 10^{-5} \left[\mathrm{m}^{-2} \right]$ and $\Delta T_{ref} = 10$ [°K]. This formulation avoids fractional powers of physical physical dimensions and its implementation is therefore more amenable to the use of different unit systems. Both of these methods have been employed in our solver, as well as another developed by Hibiki and Ishii CITATION. According to [24, 28], this active nucleation site density model provides good predictions over a very wide range of flow conditions and can also account for different boiling surfaces by including a dependence on the contact angle. Studies have been performed in order to illustrate that the large spread of data on the active nucleation site density can be captured in the nucleation site density models through the inclusion of a dependence on the contact angle of the fluid

on the heated material [24, 32]. The Hibiki-Ishii model is also dependent on the system pressure, which is also known to affect the nucleation site density. This model is shown in the following formulation,

$$N_a'' = N_{ref}'' \left[1 - \exp\left(-\frac{\theta^2}{8\mu^2}\right)\right]\left[\exp\left(f\left(\rho^+\right)\frac{\lambda'}{R_c}\right) - 1\right] \tag{6.31}$$

where $N_{ref}'' = 4.72 \times 10^5 \left[\text{sites} \cdot \text{m}^{-2}\right]$, μ is a fixed reference value for the contact angle set to 0.722 rad, and λ' is the cavity length scale and is set equal to 2.50×10^6 [m]. The minimum cavity radius, R_c, is given in the following relationship,

$$R_c = \frac{2\sigma\left[1 + \left(\frac{\rho_1}{\rho_2}\right)\right]}{p\left[\exp\left(\frac{h_{fg}\Delta T_{sup}}{R_g T_w T_{sat}}\right) - 1\right]} \tag{6.32}$$

where R_g is the gas constant based on the molecular weight of the fluid. The density function, $f\left(\rho^+\right)$, is given by the following relationship,

$$f\left(\rho^+\right) = -0.01064 + 0.48246\rho^+ - 0.22712\left(\rho^+\right)^2 + 0.05468\left(\rho^+\right)^3 \tag{6.33}$$

where ρ^+ is defined by the following,

$$\rho^+ = \log\left(\frac{\rho_2 - \rho_1}{\rho_1}\right) \tag{6.34}$$

Due to the fact that many of the systems of interest (i.e. high pressure boiling simulations) are at pressures above atmospheric the Hibiki and Ishii model for active nucleation site density model was included in the solver.

6.3.9 Bubble Wait Time Model

Accodring to [6], Kurul and Podowski (1991) [35] employed the model of Tolubinski and Kostanchuk (1970) [58] and the use of this model fixes the waiting time between departures of consecutive bubbles at 80% of the bubble detachment period. This would mean a form of the model given by the following,

$$t_w = \frac{C_{tw}}{f_b} \tag{6.35}$$

where $C_{tw} = 0.8$, t_w is the bubble waiting time, and f_b is the bubble departure frequency. Our solver implements this method with C_{tw} being user-modifiable.

6.4 Evaporation Closure Model

The closure model for the evaporation mass transfer rate occurs along the heated wall only and is easily deduced since the evaporation heat flux contribution is known from the previous section. The evaporation rate per unit volume is expressed as the following,

$$\Gamma_{12} = \rho_1 f_b N_a'' \left(\frac{\pi D_{b,w}^3}{6} \right) \frac{A_w}{V_w} \tag{6.36}$$

where f_b is the bubble departure frequency, N_a'' is the nucleation site density, $D_{b,w}$ is the bubble departure / detachment diamter, A_w is the area of the wall experiencing boiling and V_w is the volume of the near-wall cell. There is one drawback to this formulation of the evaporation closure model and that is it is grid dependent. If the user increases the axial number of cells in the problem but, keeps the number of radial cells similar than there will be a higher value for the same constant heat flux. Possible avenues of future modeling could be to replace the $\frac{A_w}{V_w}$ term with a division by some factor of bubble diamter.

6.5 Volumetric Heat Source Closure Model

The closure model for the volumetric heat source terms which appear in the source term for the phase energy conservation equations again only occur along the heat wall and are easily deduced since the single phase forced convection heat flux for both phases and the quenching heat flux contributions are known from a previous section. The volumetric heat source terms for the vapor phase ($k = 1$) and the liquid phase ($k = 2$) are given by the following respectively,

$$q_1''' = q_g''' = \left(A_g q_{g,1\phi}'' \right) \frac{A_w}{V_w} \tag{6.37}$$

$$q_2''' = q_f''' = A_f \left[A_{f,1} q_{1\phi}'' + A_{f,2\phi} q_{f,2\phi}'' \right] \frac{A_w}{V_w} \tag{6.38}$$

where A_f is the total wall area fraction that accounts for heat transfer to the liquid phase and produces boiling, $A_g = 1 - A_f$ is the total wall area fraction that accounts for the rest of the wall or really just the fraction of the wall that accounts for heat transfer directly to the vapor phase, $A_{f,1\phi}$ is the area fraction for single-phase forced convection of the fraction of the wall that accounts for the heat transfer to the liquid phase, $A_{f,2\phi} = 1 - A_{f,1\phi}$ is the area fraction for boiling of the fraction of the wall that accounts for the heat transfer to the liquid phase, $q''_{1\phi}$ is the single-phase force convection heat flux to the liquid, $q''_{f,2\phi}$ is the two-phase (quenching) heat flux, $q''_{g,1\phi}$ is the single-phase forced convection heat flux to the vapor, A_w is the area of the wall experiencing boiling and V_w is the volume of the near-wall cell.

Chapter 7

NUMERICS

7.1 Description

Now to give a brief description of the numerics and closure modeling of the solver. The method, which can be deduced from the discussion in the previous sections, is a two-phase six equation pressure based method for quasi-compressible flows with interpenetrating continua that employs a PIMPLE solution algorithm. The quasi-compressibility is evident from the substantial derivatives of phase density present in the various transport equations and the estimation of the compressibility present in the pressure equation (given later in the document). The PIMPLE solution algorithm essentially resembles the combination of two segregated solution algorithms for pressure-based methods. The first is the SIMPLE algorithm that is typically used in the simulation of steady state flow problems and the second is the PISO algorithm that is typically used to simulate transient flow problems. The solver contains closure modeling for

- The turbulent affects on both phases
- The enhanced turbulence in the continuous phase due to the presence of the dispersed phase
- The various interfacial momentum terms (e.g. drag, lift, wall lubrication, turbulence dispersion and virtual mass)
- The various mono-dispersed diameter models (e.g. thermal, iso-thermal, constant and IAC)

- The phase change and mass transfer modeling
- The various standard and user-defined thermo-physical models

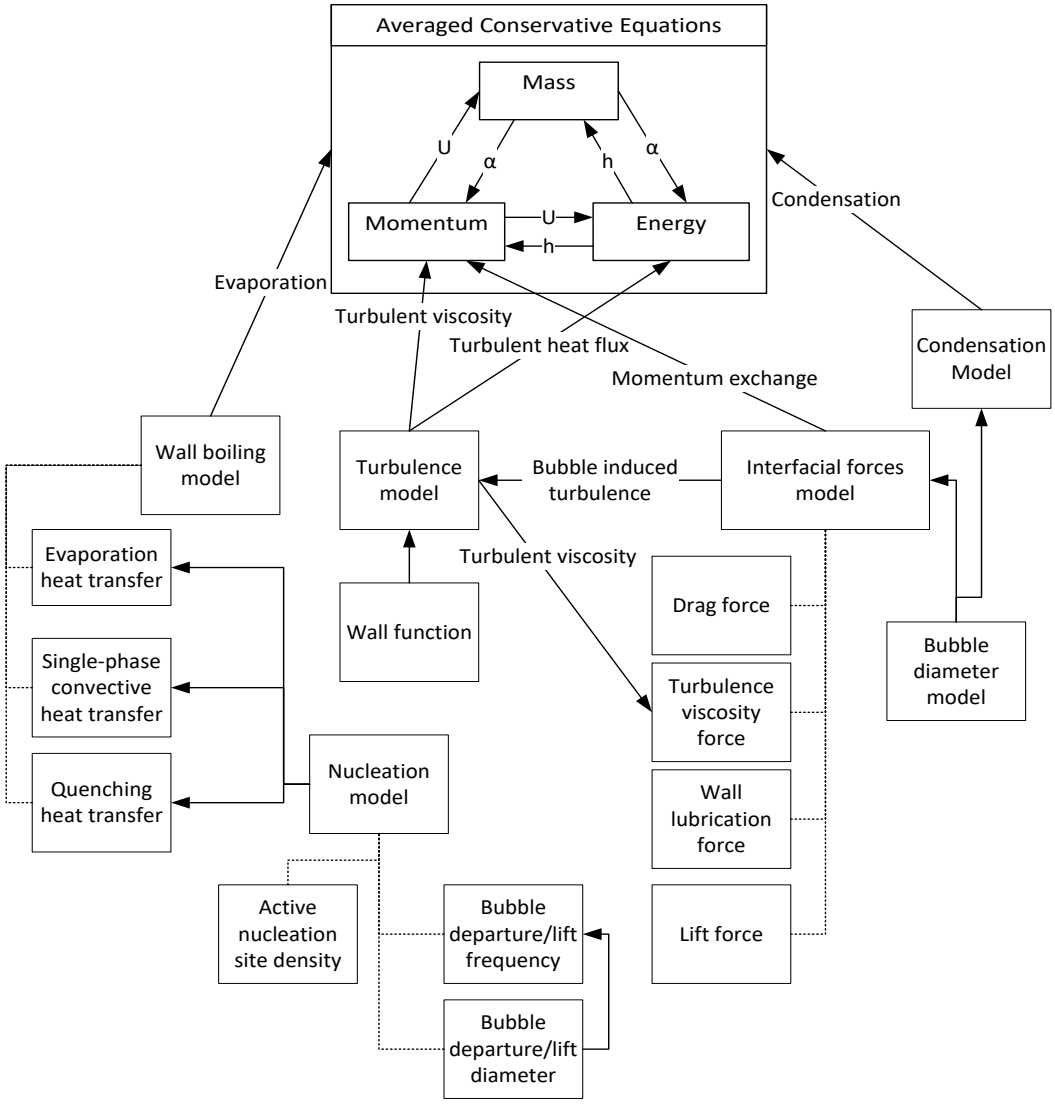

Figure 7.1 Closure Model Network

Fig. 7.1 is provided to give a good representation of the full network of closure models required for modeling multiphase boiling flows with constant wall heat fluxes and the

inter-connectivity relationships between the closure models, other closure models, and the governing conservation equations.

The solver also contains functionality for many different forms of spatial and temporal discretizations which are part of OpenFOAM, for details on the different options for the spatial and termporal discretization methods Rusche [49], the OpenFOAM Programmer's and User's Guides [38, 39] and `https://cfd.direct/openfoam/` are all good resources. The descriptions are not given in this work as they are not part of the stated objectives. All numerical results were achieved using the same discretization for both space and time and the input files which govern those options can be seen in Appendix A. The schemes chosen are first order accurate in time and first or second order in space with some upwinding and limiting performed as well.

7.2 PISO Algorithm & Pressure-Velocity Coupling

The pressure equation (and the PISO algorithm) deals with the pressure-velocity coupling and corrects the fluxes and velocities with an updated pressure field so that continuity is obeyed. This section will describe this process that is loosely based on the process given in [21] and derive the equations. The first step in the process is the velocity prediction through the use of a Jacobi Iteration scheme.

The Jacobi iteration scheme for solving linear sets of coupled equations states that if $\mathbf{A}x = \mathbf{R}$, where $\mathbf{A}$ is the coefficient matrix and $\mathbf{R}$ is the source vector, then the approximate solution to this linear system can be found through iterating,

$$x \simeq \mathbf{A}_D^{-1}\mathbf{A}_H \tag{7.1}$$

where $\mathbf{A}_D$ is the matrix with only the diagonal components of $\mathbf{A}$ (as its very easy to compute the inverse of a diagonal matrix), and $\mathbf{A}_H$ is defined as the following,

$$\mathbf{A}_H = \mathbf{R} - \mathbf{A}_N x \tag{7.2}$$

where $\mathbf{A}_N$ refers to the coefficient matrix with only the off diagonal components. The typical Jacobia solution procedure can be summarized in four steps : (1) Make an initial guess x_0 taken from the previous time step; (2) Calculate $\mathbf{A}_H = \mathbf{R} - \mathbf{A}_N x_0$; (3) Evaluate approximate solution $x_j \simeq \mathbf{A}_D^{-1}\mathbf{A}_H$; (4) Repetition of step 2 and 3 until $x_j - x_{j-1} \leq$ tolerance. So using

the aforementioned Jacobi iteration, the velocity, $\mathbf{U}_k^*$ and consequenty the flux, ϕ_k^*, are predicted using the following,

$$\mathbf{U}_k^* = \mathbf{A}_{D,k}^{-1}\mathbf{A}_{H,k} \tag{7.3}$$

$$\phi_k^* = \mathbf{S}\cdot\mathbf{U}_{k,f}^* = \mathbf{S}\cdot\left(\mathbf{A}_{D,k}^{-1}\mathbf{A}_{H,k}\right)_f \tag{7.4}$$

where $\mathbf{A}$ is the system of linear algebraic equations generated from the discretization of the phase momentum equation, $\mathbf{S}$ represents the face area vector and $\mathbf{U}_{k,f}^*$ represents the velocity of phase k interpolated on the cell face. It is important to note that $\mathbf{A}$ typically will be missing some terms for numerical reasons (e.g. gravity terms, pressure gradient, explicit drag force, lift force, turbulence dispersion force, etc) depending on the method employed; however, whatever term is not accounted for in the momentum equations (except for the pressure gradient terms) must be accounted for in correcting the predicted flux, as follows for the gravity term,

$$\phi_k^{**} = \phi_k^* + (\mathbf{g}\cdot\mathbf{S})\left(\alpha_k\mathbf{A}_{D,k}^{-1}\right)_f \tag{7.5}$$

the explicit drag force term,

$$\phi_k^{**} = \phi_k^* + \left(\frac{K^d\mathbf{A}_{D,k}^{-1}}{\rho_k}\right)_f \phi_j \tag{7.6}$$

where $K^d = -\frac{3}{4}\left(C_d D_b\right)\rho_2\alpha_1|\mathbf{U}_r|$ is the drag force coefficient and the subscript j denotes the other phase. The lift force is added in the following manner,

$$\phi_k^{**} = \phi_k^* + \pm\left(\frac{\mathbf{A}_{D,k}^{-1}}{\rho_k}\right)_f (\alpha_1)_f\left[\left(K^l\right)_f\cdot\mathbf{S}\right] \tag{7.7}$$

where $K^l = C_l\,\rho_2\mathbf{U}_r\times(\nabla\times\mathbf{U}_2)$ is the lift force coefficient and the sign is positive for $k=2$ and negative for $k=1$. Finally the turbulence dispersion force term can be added in the following manner as well,

$$\phi_k^{**} = \phi_k^* \pm\left(\frac{\mathbf{A}_{D,k}^{-1}}{\rho_k}\right)_f K^{td}\,|\mathbf{S}|\,\nabla_f^{\perp}\alpha_1 \tag{7.8}$$

where $K^{td} = \mathbf{M}_k^{td}\nabla\alpha_1$ is the turubulence dispersion force coefficient and the sign is positive

for $k=1$ and negative for $k=2$. The mixture flux is defined by the following,

$$\phi^{**} = (\alpha_1)_f \, \phi_1^{**} + (\alpha_2)_f \, \phi_2^{**} \tag{7.9}$$

and analagously the mixture velocity is given by the following,

$$\mathbf{U}^{**} = (\alpha_1)_f \, \mathbf{U}_1^{**} + (\alpha_2)_f \, \mathbf{U}_2^{**} \tag{7.10}$$

where for the explicit drag force term,

$$\mathbf{U}_k^* = \mathbf{U}_k^* + \left(\frac{K^d \mathbf{A}_k^{-1}}{\rho_k} \right) \mathbf{U}_j \tag{7.11}$$

the lift force term,

$$\mathbf{U}_k^* = \mathbf{U}_k^* \pm \left(\frac{\mathbf{A}_k^{-1}}{\rho_k} \right) \alpha_1 K^l \tag{7.12}$$

and the turbulence dispersion force term,

$$\mathbf{U}_k^* = \mathbf{U}_k^* \pm \left(\frac{\mathbf{A}_k^{-1}}{\rho_k} \right) K^{td} \nabla \alpha_1 \tag{7.13}$$

much like the flux corrections previously discussed. Now the solver constructs and solves the pressure equation. The pressure equation is obtained from the mommentum and continuity equation in order to attempt to find a unique pressure field for when both phases are present or not. This is accomplished by use of the mixture flux equation and according to Weller [64] the continuity constraint can be used in terms of mixture flux.

$$\nabla \cdot \phi = \frac{\Gamma_1}{\rho_1} - \frac{\Gamma_1}{\rho_2} - \frac{\alpha_1}{\rho_1} \frac{D\left(\rho_1\right)}{Dt} - \frac{\alpha_2}{\rho_2} \frac{D\left(\rho_2\right)}{Dt} \tag{7.14}$$

The total flux including the pressure gradient correction can be written as the following,

$$\phi_k = \phi_k^{**} - \left(\frac{1}{\rho_k \mathbf{A}_{D,k}} \right)_f S_f \nabla_f^{\perp} p \tag{7.15}$$

So by substituting Eq. 7.15 and Eq. 7.9 into Eq. 7.14 you get the following,

$$\nabla\cdot\phi^{**}-\nabla\cdot\left[\left(\alpha_{1,f}\left(\frac{\mathbf{A}_{D,1}^{-1}}{\rho_1}\right)_f+\alpha_{2,f}\left(\frac{\mathbf{A}_{D,2}^{-1}}{\rho_2}\right)_f\right)\nabla_f^{\perp}p\right]=\frac{\Gamma_1}{\rho_1}-\frac{\Gamma_1}{\rho_2}-\frac{\alpha_1}{\rho_1}\frac{D\left(\rho_1\right)}{Dt}-\frac{\alpha_2}{\rho_2}\frac{D\left(\rho_2\right)}{Dt} \quad (7.16)$$

In the solver the pressure equation is constructed using the flux prediction that has been correct with gravity (e.g. ϕ_k^{**}), while the calculation of the total derivatives of the phase densities inside the compressibility terms are performed using the fluxes evaluated at the previous iteration (e.g. before the flux prediction that was previously described). This process is used in accordance with Weller [64]. The substantive derivatives for the density can be re-written by substitution of the following constitutive law that linearly correlates the pressure and density.

$$\rho_k=\Psi_k p \quad (7.17)$$

where Ψ_k stands for the compressibility of phase / fluid k. Using this relation the substantive derivatives have the following form,

$$\begin{aligned}\frac{D\left(\rho_k\right)}{Dt}&=\frac{\partial\left(\rho_k\right)}{\partial t}+\mathbf{U}_k\cdot\nabla\left(\rho_k\right)\\&=\frac{\partial\left(\rho_k\right)}{\partial t}+\nabla\cdot\left(\rho_k\mathbf{U}_k\right)+\rho_k\nabla\cdot\left(\mathbf{U}_k\right)\\&=\frac{\partial\left(\Psi_k p\right)}{\partial t}+\nabla\cdot\left(\Psi_k p\,\mathbf{U}_k\right)+\Psi_k p\nabla\cdot\left(\mathbf{U}_k\right)\end{aligned} \quad (7.18)$$

So, substituting this in for the substantive derivates in the pressure equations gives the final form,

$$\begin{aligned}\nabla\cdot\phi^{**}-\nabla\cdot\left[\left(\alpha_{1,f}\left(\frac{\mathbf{A}_{D,1}^{-1}}{\rho_1}\right)_f+\alpha_{2,f}\left(\frac{\mathbf{A}_{D,2}^{-1}}{\rho_2}\right)_f\right)\nabla_f^{\perp}p\right]&=\frac{\Gamma_1}{\rho_1}-\frac{\Gamma_1}{\rho_2}\\-\frac{\alpha_1}{\rho_1}\left(\frac{\partial\left(\Psi_1 p\right)}{\partial t}+\nabla\cdot\left(\Psi_1 p\,\mathbf{U}_1\right)+\Psi_1 p\nabla\cdot\left(\mathbf{U}_1\right)\right)&\\-\frac{\alpha_2}{\rho_2}\left(\frac{\partial\left(\Psi_2 p\right)}{\partial t}+\nabla\cdot\left(\Psi_2 p\,\mathbf{U}_2\right)+\Psi_2 p\nabla\cdot\left(\mathbf{U}_2\right)\right)&\end{aligned} \quad (7.19)$$

Once the pressure equation is solver, both the velocity fields and the fluxes are corrected, using pressure gradient and gravity term which are reconstructed from the fluxes computed

with the updated pressure field,

$$\mathbf{U}_k = \mathbf{U}_k^* + \text{reconstruct}\left[(\mathbf{g}\cdot\mathbf{S})\left(\alpha_k \mathbf{A}_{D,k}^{-1}\right)_f - \left(\frac{1}{\rho_k \mathbf{A}_{D,k}}\right)_f S_f \nabla_f^{\perp} p\right] \tag{7.20}$$

where the operator "reconstruct" produces an approximate velocity vector with a reconstruction procedure from the volumetric flow rate [21].

7.3 Solution Algorithm

This section is going to briefly discuss the current solver's solution algorithm in detail. Fig. 7.2 displays a fairly detailed step-by-step description of the overall solution algorithm and what variables are solved for at which point in the code. It also highlights the portions of the code where the closure models are applied. The outer-most loop is the time stepping loop, then there is the outer PIMPLE loop (or reall just the SIMPLE like functionality of the PIMPLE loop). The next step is applying the enhanced turbulence closure model, then phase change closure models. After that the mass conservation governing equation is solved and if interfacial area concentration equation diameter model is chosen by the user it is then updated. Following this the turbulence for both phases is solved for via the closure modeling previously discussed. Once that is accomplished the Energy conservation equations are solved, then the thermo-physical properties are updated for the new temperature. Also, if the thermal diameter model is used it is updated at this point as well. The phase momentum equation linear systems are then calculated. At this point we then move into the PIMPLE Corrector loop (or really just the PISO algorithm portion of the PIMPLE loop) where the pressure equation is solved, the velocities are corrected, then the thermo-physical properties are updated for the new pressure. Also, if the iso-thermal diameter model is chosen by the user then it is updated at this point. Compressibility source terms are updated, acceleration terms used in the virtual mass closure model are updated, and the pressure work terms used in the energy equations are updated. This gives a very brief walk through the solution process used in our solver.

■ **Begin: Time Loop** $t^n < t_{\text{final}}$

→ Set: Δt & $t^{n+1} = t^n + \Delta t$

→ **Begin: PIMPLE Outer Loop (SIMPLE)** $i = 1, N_{\text{outer}}$

- Bubble Induced Turbulence: $\left(\nu_2^D\right)^{(i+1)}$
- Phase Change Closure: $\Gamma_{12}^{(i+1)}$, $\Gamma_{21}^{(i+1)}$, $\left(\phi^{nuc}\right)^{(i+1)}$, $\left(q_k'''\right)^{(i+1)}$
- **Mass Conservation:** $\alpha_k^{(i+1)}$, $\left(\alpha_k \mathbf{U}_k\right)|_f^{(i+1)}$, $\rho^{(i+1/2)}$
  - Interfacial Area Concentration Diameter: $a_{i,1}^{(i+1)}$, $D_b^{(i+1)}$
- Turbulence: $k_k^{(i+1)}$, $\epsilon_k^{(i+1)}$, $\left(\nu_k^t\right)^{(i+1)}$
- **Energy Conservation:** $T_k^{(i+1)}$, $h_k^{(i+1)}$
  - Update thermo-physical properties: $\rho_k^{(i+1/2)}$, $\mu_k^{(i+1/2)}$, $c_{p,k}^{(i+1/2)}$, $\lambda_k^{(i+1/2)}$, ...
  - Thermal Diameter: $D_b^{(i+1)}$
- **Momentum Conservation:** $\mathbf{A}_k^{(i+1)}$, $\mathbf{R}_k^{(i+1)}$, $\mathbf{M}_k^{(i+1)}$
- **Begin: PIMPLE Corrector Loop (PISO)** $j = 1, N_{\text{corrector}}$
  - Pressure Equation: $\phi_k^{(j+1)}$, $\mathbf{U}_k^{(j+1)}$, $p^{(j+1)}$
    - Update thermo-physical properties: $\rho_k^{(j+1)}$, $\mu_k^{(j+1)}$, $c_{p,k}^{(j+1)}$, $\lambda_k^{(j+1)}$, ...
    - Iso-thermal Diameter: $D_b^{(j+1)}$
  - Compressibility Terms: $\left(\frac{\mathrm{D}(\rho_k)}{\mathrm{Dt}}\right)^{(j+1)}$
  - Acceleration Terms: $\left(\frac{\mathrm{D}(\mathbf{U}_k)}{\mathrm{Dt}}\right)^{(j+1)}$
  - Pressure Work Terms: $\left(\alpha_k \frac{\partial(p)}{\partial t}\right)^{(j+1)}$
- **End: PIMPLE Corrector Loop (PISO)**

→ **End: PIMPLE Outer Loop (SIMPLE)**

■ **End: Time Loop**

Figure 7.2 Solution Algorithm

7.4 Testing Platform

Now to give a description of what is being referred to with the term “testing platform” and what coding changes were made to the solver from the initial form. The platform initially consisted of a solver where the only things that could be switched via input files, aside from the standard OpenFOAM functionality, were the interfacial momentum terms (e.g. drag, lift, wall lubrication, turbulence dispersion, virtual mass, bubble diameter) and the base thermo-physical modeling. All other aspects were “hard coded” to certain values. This was not ideal. In order to have an effective modular testing platform it was decided that the solver needed to posses the ability to control all aspects of the solver via input files and a user-definable like functionality which allows the changing of methods simply and locally (e.g. without the need to add in different function calls, change the source code, etc.).

The platform consists mainly of a solver that heavily employs the use of a inheritance. This allowed the development of a base class for all closure models, equations of state, governing equations, etc. to be defined and then all the methods were implemented via child-class definitions of the corresponding base-class. This gives the solver a user-definable like functionality for all of the closure models, thermo-physical properties, post-processing and governing equations.

The library of OpenFOAM is basically a toolkit that gives the same top-level coding functionality for spatial discretization schemes, time discretization schemes, linear solvers, etc. So the development of the platform was really just an extension of the OpenFOAM-like functionality in order to give a user the ability to add new closure models, add/change governing equations, add/change spatial and time discretization schemes and essentially control all aspects of the code, except for the over-all order of the solution algorithm, via control files. The addition/testing of these closure models, methods, etc. can be done with practice in a very short amount of time which allows developers to test a wide variety of methods efficiently. This basically allows the code to be developed to be useful for not only a wide variety of governing equations and flow scenarios, but also allows, because of direct access to the source code, the implementation of a Sensitivity Analysis (SA) & Uncertainty Quantification (UQ) framework for any potential generation of boiling models, implementation of interfacial forces, turbulence closure, bubble diameter modeling, etc. The beginings of the SA & UQ implementation is being performed by another in the group and will soon will be published.

Chapter 8

NUMERICAL RESULTS

8.1 Ransom's Faucet Problem

This numerical test case is a very simple problem. The Ransom faucet problem [46] is a very famous scenario that simulates a free-falling column of water, surrounded by initially stagnant vapor. Thus, the problem is concerned with the properties of a gravity wave moving through water that has a non-zero initial vertical velocity. This problem is useful because it tests our solvers treatment of the body force term. When this problem is treated with no diffusion term, as it is here, it also provides a manner by which to observe the numerical dissipation generated by the numerical model.

The Faucet problem deals with a water jet injected with a $10\,\frac{\mathrm{m}}{\mathrm{s}}$ velocity and accelerated by gravity downward (and hence, narrowed according to the mass conservation law) surrounded by stationary air, in a 12 m length tube. This is a one-dimensional problem and has the initial conditions given in Table 8.1. For this problem, the same values of initial conditions (see previous table) are applied as boundary conditions at the inlet, except for the pressure which is extrapolated from the interior cell (e.g. zero gradient); whereas, the pressure at the outlet is specified as the value supplied (see previous table) and all the other variables are extrapolated from the interior cells (e.g. zero gradient). Gravity is given the standard $g = 9.81\,\frac{\mathrm{m}}{\mathrm{s}}$ value in the positive x direction (which is taken to be the downward direction). In this problem, there are no interfacial forces, wall heating, or turbulence modeled. This problem has exact solutions for both the void fraction and velocity and was used to test our solver's ability to run transient simulations, capture discontinuities, handle

Table 8.1 Ransom's Faucet Problem Initial Conditions

Parameter	**Variable**	**Value**
Pressure	p	0.1 MPa
Gas Void Fraction	α_1	0.2
Liquid Void Fraction	α_2	0.8
Gas Velocity	$\mathbf{U}_1$	$0\,\frac{\mathrm{m}}{\mathrm{s}}$
Liquid Velocity	$\mathbf{U}_2$	$10\,\frac{\mathrm{m}}{\mathrm{s}}$
Gas Temperature	T_1	300 K°
Liquid Temperature	T_2	300 K°

compressibility, and run inviscid problems. The exact solutions are given by the following,

$$u(x,t) = \begin{cases} \sqrt{u_2 + 2\,g\,x} & \text{if } x \leq u_2\,t + \frac{g\,t^2}{2} \\ u_2 + g\,t & \text{otherwise} \end{cases} \tag{8.1}$$

$$\alpha(x,t) = \begin{cases} \frac{1-(1-\alpha_1)u_2}{\sqrt{u_2+2\,g\,x}} & \text{if } x \leq u_2\,t + \frac{g\,t^2}{2} \\ \alpha_1 & \text{otherwise} \end{cases} \tag{8.2}$$

Now lets move onto the results achieved. It is important to note that all the results achieved with our solver were performed using the same time & space discretization schemes in OpenFOAM, the same initial conditions and boundary conditions, and the only things that differ between the cases are those which are stated. The first set of cases that were executed were a grid refinement of the PISO algorithm. This was done to see the affect that progressively refining the grid has on numerical dissipation, the presence of oscillations in the solution, the ability to capture the discontinuity and the sharpness of discontinuity, and the time accuracy of the PISO algorithm. The results are given in Fig. 8.1 & Fig. 8.2. Fig. 8.1 gives the numerical results for a CFL = 0.01 (which was chosen in order to ensure time accuracy) with various grid sizes using just the PISO algorithm loop portion of the PIMPLE algorithm. As can be seen by inspection of the void fraction comparison figure significant oscillations appear in the solution. These oscillations occur for all values of refinement; however, they are significantly more pronounced for the more refined cases. The more refined cases do capture the sharpness of the discontinuity but have significant

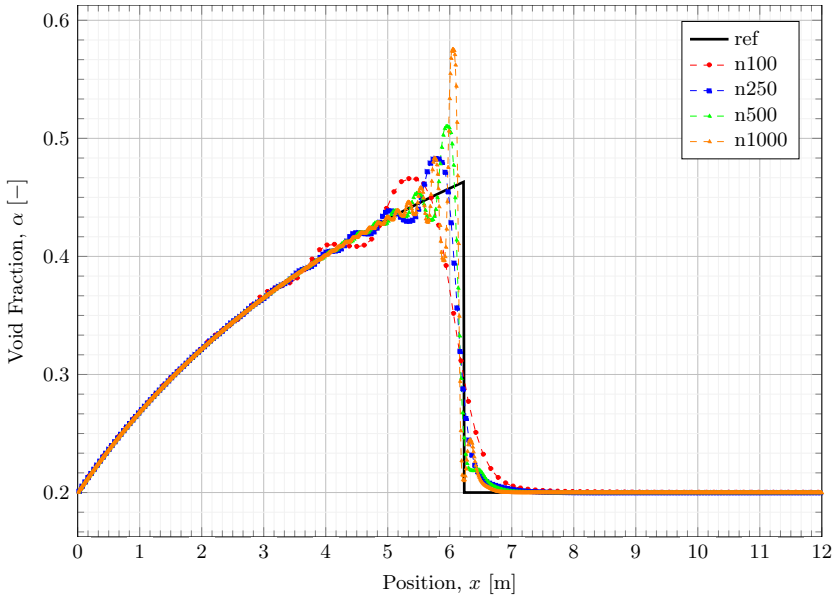

Figure 8.1 Ransom's Faucet Problem PISO Algorithm Grid Refinement - Void Fraction Comparison

overshoots which are not desirable as they can lead to instabilities in the more complicated problems. For the velocity comparison in Fig. 8.2 the oscillations increase in amplitude with an increase in grid refinement much like the void fraction case; however, it is harder to see as the amplitudes are very small in comparison to the magnitude of the velocity.

After testing the PISO algorithm our aim was to test the PIMPLE aglorithm and use the outer iterations as quasi-time steps to come to a steady-state solution for each actual time step in order to both keep time accuracy but more strongly couple the governing equations. Again, this was done to see the affect that progressively refining the grid has on numerical dissipation, the presence of oscillations in the solution, the ability to capture the discontinuity and the sharpness of discontinuity, and the time accuracy of the PIMPLE algorithm. The results are given in Fig. 8.3 & Fig. 8.4. Fig. 8.3 gives the numerical results using a CFL = 0.5 which can be larger due to the outer iterations (e.g. SIMPLE algorithm iterations) in the PIMPLE algorithm solution process and the stronger coupling of the segregated solution method that it results in. This stronger coupling along with solution relaxation allows oscillations to be damped, larger time steps to be employed, and generally results in a much better solution than the PISO algorithm being employed by itself. There are some drawbacks, the use of the outer iterations significantly affects the performance of

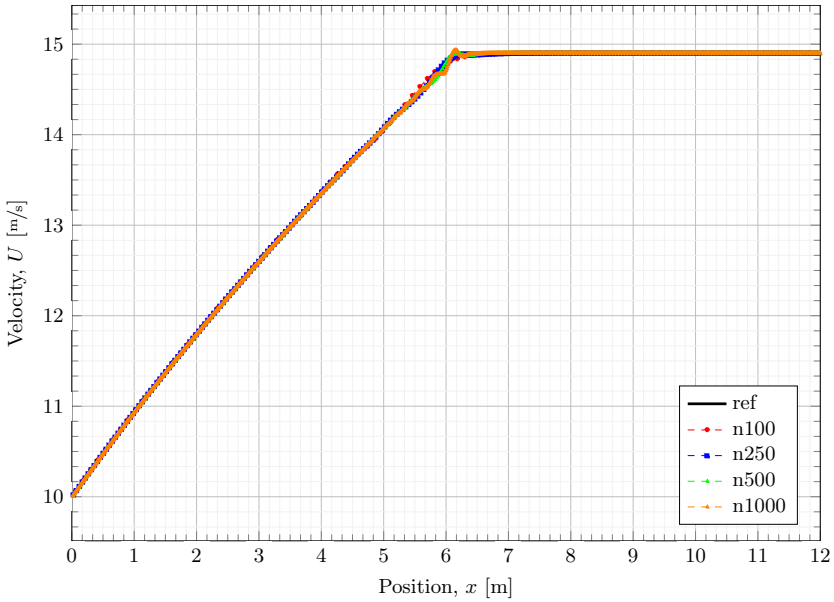

Figure 8.2 Ransom's Faucet Problem PISO Algorithm Grid Refinement - Velocity Comparison

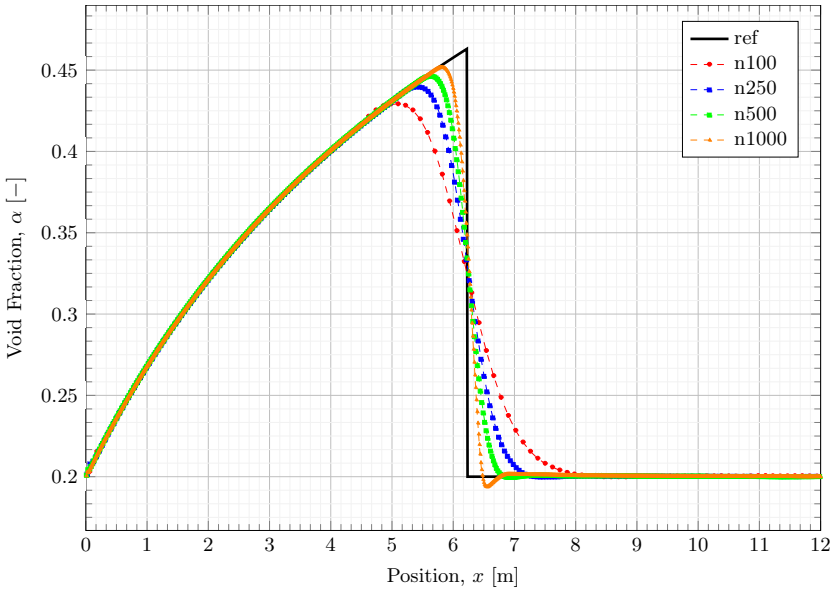

Figure 8.3 Ransom's Faucet Problem PIMPLE Algorithm Grid Refinement - Void Fraction Comparison

the code as during harsh transients hundreds of outer iterations may be employed to satisfy the convergence criteria for a single time step; however, outside of those harsh transients very few outer iterations can be employed to achieve the same convergence criteria. The

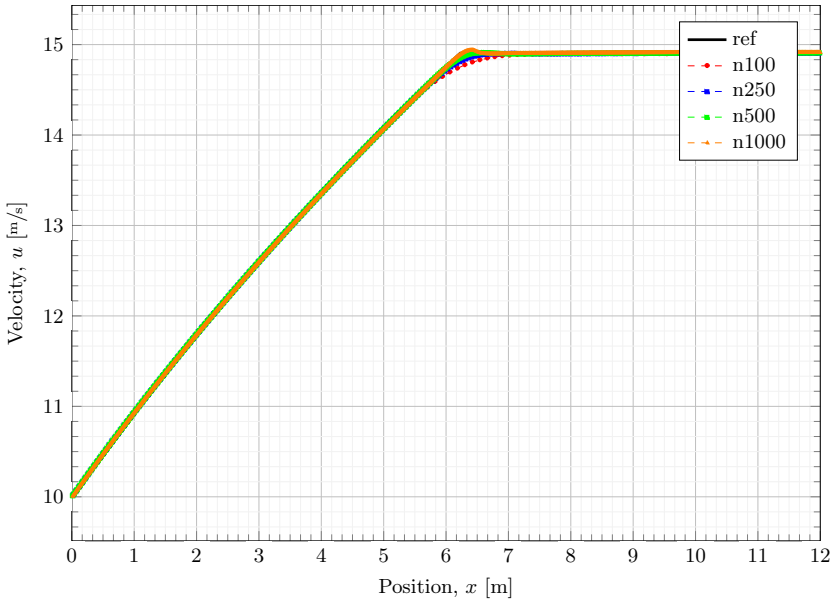

Figure 8.4 Ransom's Faucet Problem PIMPLE Algorithm Grid Refinement - Velocity Comparison

use of the SIMPLE outer loop iterations and the PISO algorithm iterations allows the use of a larger CFL number and can be seen from Fig. 8.3 & Fig. 8.4 to displays a significant reduction in the oscillations for all levels of grid refinement. There is also decrease in the sharpness of the discontinuity for each respective level of refinement in comparison to the PISO results; however, the smooth results with minimal over and under shoots are much more desirable.

Now after seeing the benefits from using the PIMPLE algorithm, we decided to check to see the affect lowering the CFL number has on the results. This was done to see if the reduced time step size would affect the solution. The results are given by Fig. 8.5 & Fig. 8.6. Fig. 8.5 & Fig. 8.6 gives the numerical results using a fixed grid size of 500 cells, the PIMPLE loop and varying the CFL number. As you can see from inspecting the figures the use of the outer loop of the PIMPLE algorithm is only beneficial in terms of reducing the oscillations in the solution with the use of a higher CFL number for this problem. This is thought to be the case due to the reduction of time step size causing a reduction in numerical diffusion (which is a problem without viscous affects for segragated solvers) that causes oscillations in the solution. However, the size of the oscillations in comparison to just using the PISO algorithm is reduced and is especially easy to see in the velocity comparison in Fig. 8.6.

Now in order to see a direct comparison between the PISO algorithm results using

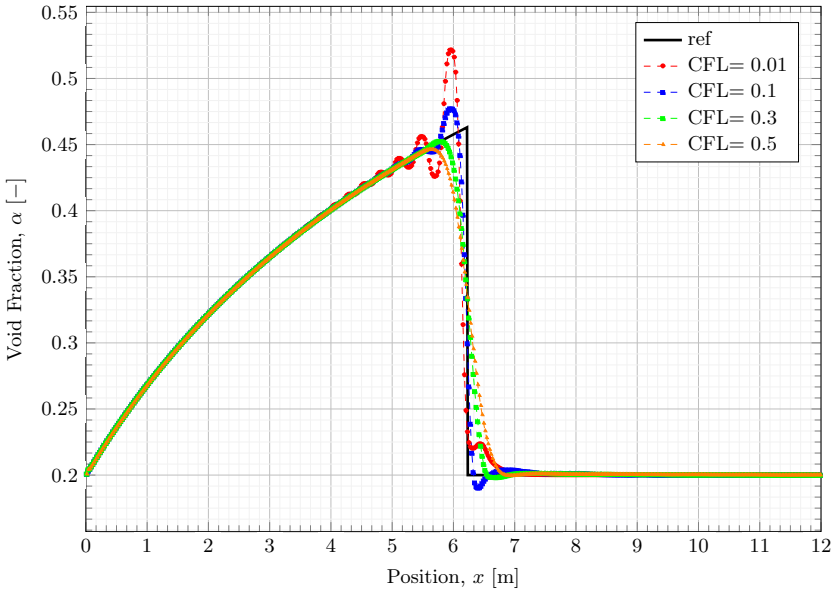

Figure 8.5 Ransom's Faucet Problem PIMPLE Algorithm CFL Refinement - Void Fraction Comparison

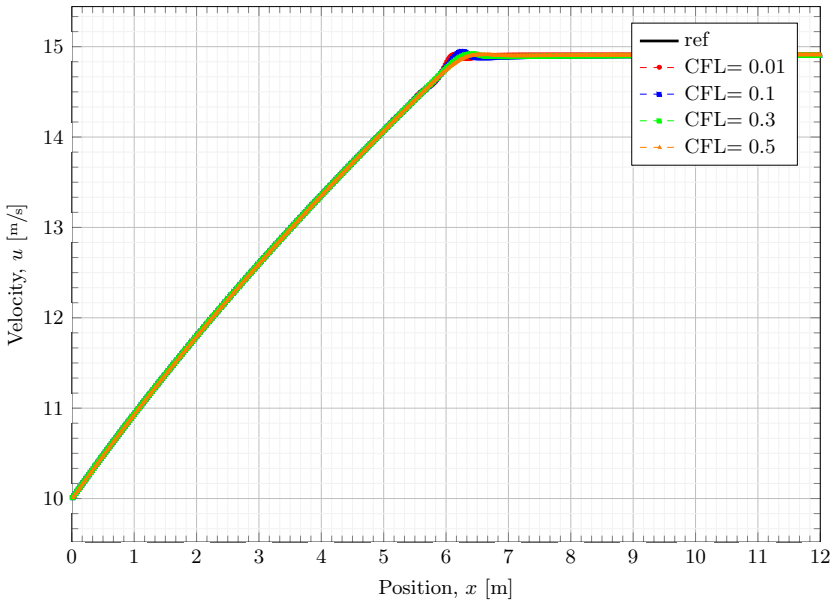

Figure 8.6 Ransom's Faucet Problem PIMPLE Algorithm CFL Refinement - Velocity Comparison

a CFL = 0.1 and the PIMPLE algorithm results using a CFL = 0.3 with a grid of $N = 500$ cells in terms of sharpness of the interface. The results given for the direct comparison are displayed in Fig. 8.7 & Fig. 8.8. As can be seen by a direct comparison of PISO algorithm

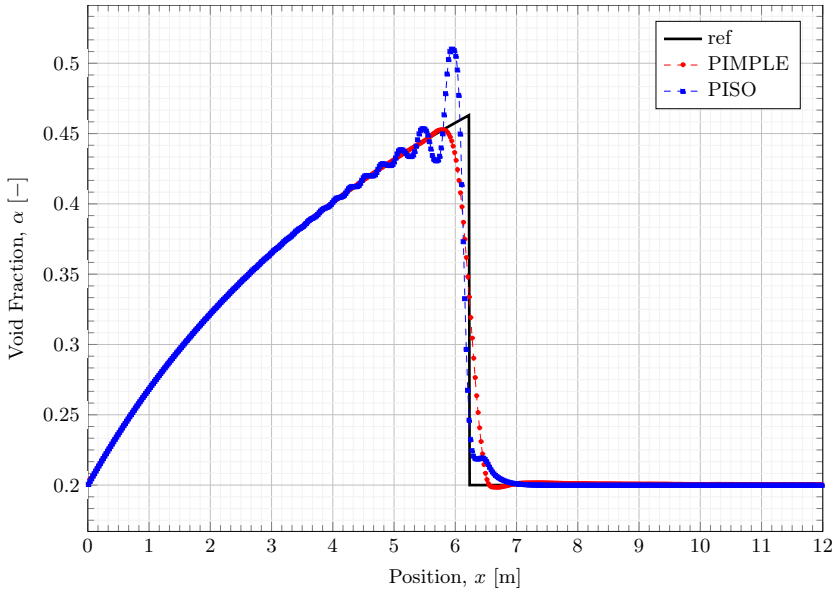

Figure 8.7 Ransom's Faucet Problem PIMPLE & PISO Algorithm - Void Fraction Comparison

results, using a small CFL to ensure time accuracy, and the PIMPLE algorithm results with a large CFL to ensure the dampening of oscillations on the same grid there is a slight loss in sharpness of the discontinuity with the removal of the oscillations in the void fraction near the discontinuity. This clearly displays the added benefit of using the PIMPLE algorithm even though the computational cost is increased. As can be seen from the velocity comparison in Fig. 8.8 the PISO algorithm & PIMPLE algorithm results are very close to each other. Now, finally for this test case we wanted to compare the performance of our solver to a commerical CFD package, and also to a fully coupled density based method that is being developed by other members of our group. The commerical CFD software Star-CCM+ was chosen as the package to compare our results to. The results in Fig. 8.9 were achieved by running the same setup on all three solvers. The figure gives a comparison of the numerical results for this test case between our solver, a fully coupled density based algorithm developed in our group, and Star-CCM+. It can be seen that our solver performs extremely well in comparison to both through the use of the PIMPLE algorithm.

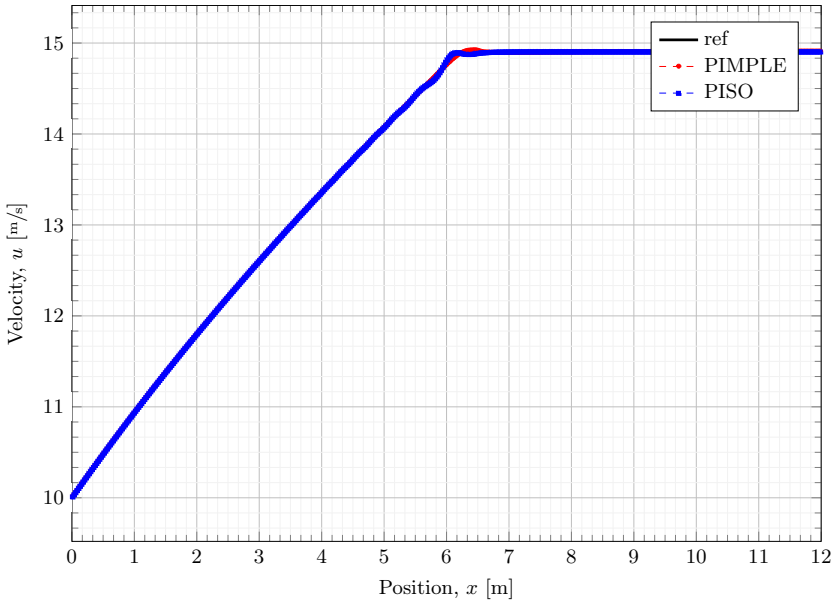

Figure 8.8 Ransom's Faucet Problem PIMPLE & PISO Algorithm - Velocity Comparison

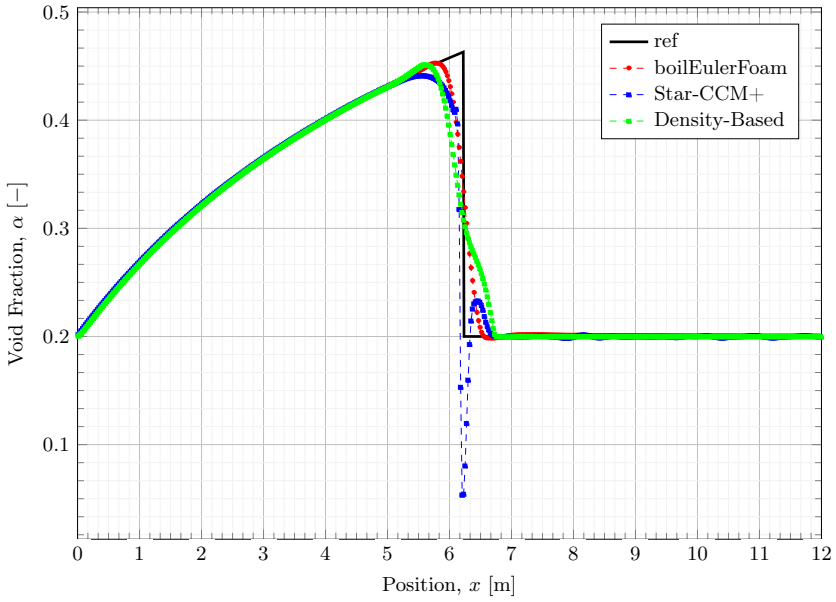

Figure 8.9 Ransom's Faucet Problem PIMPLE Algorithm Comparison - Void Fraction

8.2 Air-to-Water Shocktube Problem

This test case is again a academic type problem and will test the ability of our solver to capture the physics of shocks, highly compressible inviscid flows, pressure / material discontinuities and other phenomena with two fluids of different equations of state. This numerical test case is the air-to-water shock-tube problem. This is a transient one-dimensional problem of a stationary column of air and water with a contact and pressure discontinuity in the center of the column located at $x = 5$ m. This one-dimensional problem has the initial conditions given in Table 8.2 for the left (e.g. $x < 5$ m) and right (e.g. $x > 5$ m) states. The

Table 8.2 Air-to-Water Shocktube Problem Initial Conditions

Parameter	**Variable**	**Left State** ($x < 5\,\mathbf{m}$)	**Right State** ($x > 5\,\mathbf{m}$)
Pressure	p	10^9 Pa	10^5 Pa
Gas Void Fraction[1]	α_1	$1-\varepsilon$	ε
Liquid Void Fraction[1]	α_2	ε	$1-\varepsilon$
Gas Velocity	$\mathbf{U}_1$	$0\,\frac{\mathrm{m}}{\mathrm{s}}$	$0\,\frac{\mathrm{m}}{\mathrm{s}}$
Liquid Velocity	$\mathbf{U}_2$	$0\,\frac{\mathrm{m}}{\mathrm{s}}$	$0\,\frac{\mathrm{m}}{\mathrm{s}}$
Gas Temperature	T_1	308.15 K°	308.15 K°
Liquid Temperature	T_2	308.15 K°	308.15 K°

[1]- ε has a range of values of $\left[10^{-8}, 10^{-4}\right]$

thermo-physical model used for this problem is the stiffened ideal gas equation of state (e.g. $p = \rho\,(R\,T) - p_0$ where $p_0 = 0$ and $R = 287$ for air, and $p_0 = 8.913 \times 10^8$ and $R = 3000$ for water). For this problem, the boundary conditions at the inlet and outlet are all extrapolated from the interior cells and there are no interfacial forces, wall heat transfer, phase change or turbulence modeled in this problem. Now lets move onto the results achieved. It is important to note that all the results achieved with our solver were performed using the same time and space discretization schemes in OpenFOAM, the same initial conditions and boundary conditions, and the only things that differ between the cases are those which are stated. The first set of cases that were executed were a grid refinement of the PIMPLE algorithm, the

PISO algorithm alone was found after many attempts to be unable to successfully simulate this problem accurately. This was done to see the affect that progressively refining the grid has on numerical dissipation, the presence of oscillations in the solution, the ability to capture the discontinuities in the various fields and their sharpness, and the time accuracy of the PIMPLE algorithm. The results are given in Fig. 8.10. Fig. 8.10 gives the numerical

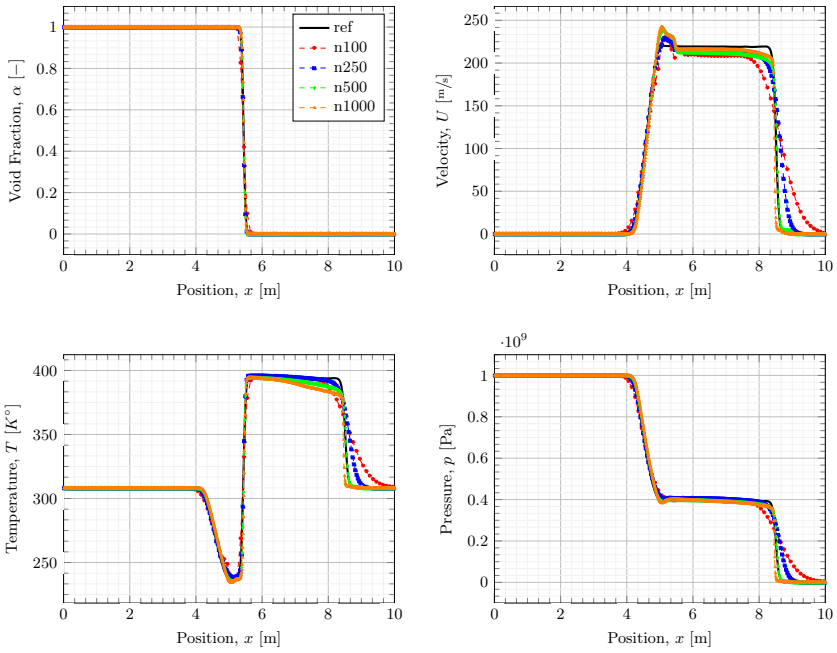

Figure 8.10 Air-to-Water Shocktube CFL = 0.5 Grid Refinement

results using the PIMPLE algorithm, a CFL = 0.5, and various grid refinements. As can be seen in the figures, the increase in grid refinement yields a better approximation when compared to the reference solution that is provided by the density based method developed in our group. The slight inaccuracies in the temperature and velocity profiles could likely be due to the absence of the mechanical work terms in the energy equations for our solver. Fig. 8.11 gives the numerical results for the PIMPLE algorithm with a fixed grid of 100 cells and varying CFL numbers. As you can see again, the use of the PIMPLE algorithm is again only beneficial with the increase in CFL number as oscillations appear in the solution for the small CFL numbers.

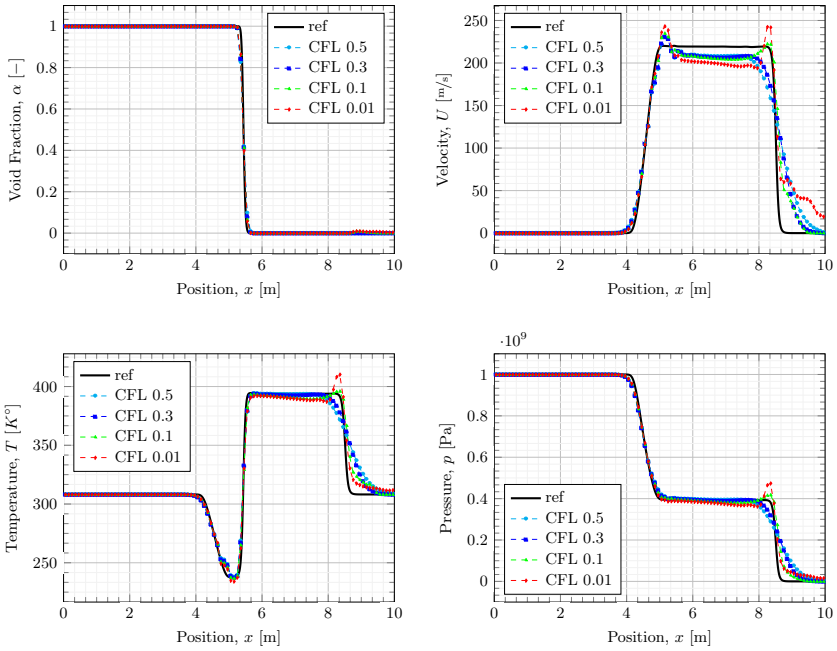

Figure 8.11 Air-to-Water Shocktube 100 cells with varying CFL Comparison

8.3 Blasius Flat Plate Problem

This problem is chosen because computational simulation is only as good as long as it accurately reflects the real world. This makes benchmarking an important step for the development, verification & validation of our solver. One option for benchmarking studies is to use analytical solutions, where available. One such solution exists that describes both velocity and temperature in a laminar boundary layer. However, currently we are only using a adiabatic situation to simplify the problem even more. This numerical test case is the blasius flat plate problem, which is a two dimensional steady state problem of flow past a flat plate. There is no acceleration by gravity, phase change, or turbulence modeled for this problem. This problem tests our solver's ability to capture a single-phase laminar boundary layer. The following table gives the inital, boundary and thermo-physical conditions. The thermo-physical model used for this problem is the stiffened ideal gas equation of state (e.g. $p = \rho\,(R\,T) - p_0$ where $p_0 = 0$ and $R = 287$ for air, and $p_0 = 8.913 \times 10^8$ and $R = 3000$ for water). For this problem, the same values of velocity (see Table 8.3) are applied as fixed value boundary conditions at the inlet & top (far-field boundary) of the domain, extrapolated from the interior cell at the symmetric boundary & outlet boundary and set to a fixed value

Table 8.3 Blasius Flat Plate Problem Setup

Parameter	**Variable**	**Value**
Pressure	p	101,300 Pa
Air Properties		
Void Fraction	α_1	0.98 [—]
Velocity	$\mathbf{U}_1$	$10\left[\frac{\text{m}}{\text{s}}\right]$
Temperature	T_1	298 [K°]
Dynamic Viscosity	μ_1	$1.7898 \times 10^{-4}\left[\frac{\text{kg}}{\text{m·s}}\right]$
Specific Heat	$C_{p,1}$	$1004.5\left[\frac{\text{J}}{\text{kg·K}}\right]$
Prandlt Number	Pr_1	0.7 [—]
Water Properties		
Void Fraction	α_2	0.02 [—]
Velocity	$\mathbf{U}_2$	$10\left[\frac{\text{m}}{\text{s}}\right]$
Temperature	T_2	298 [K°]
Dynamic Viscosity	μ_2	$8.9313 \times 10^{-3}\left[\frac{\text{kg}}{\text{m·s}}\right]$
Specific Heat	$C_{p,2}$	$4186.0\left[\frac{\text{J}}{\text{kg·K}}\right]$
Prandlt Number	Pr_2	6.15305 [—]

of (0 0 0) at the wall. Temperature follows a similar scheme, except that it is set to the fixed value of 298 at the wall. The pressure is set to the value from the table above at the outlet, and extrapolated from the interior cell at all other boundaries. The rest of the values are set to the values from the table above at the inlet and top (far-field) boundaries, and extrapolated from the interior cell values everywhere else along the boundary. For this test case we have a similarity solution for fully developed laminar boundary layer flow of the water velocity. As can be seen from Fig. 8.10 & Fig. 8.11, our solver performs well for the single-phase water results for the x-direction velocity and also fairly well for the y-direction velocity at the outlet in comparison to the similarity solution provided by theory. The two-phase results are there just to show that for a 98% air flow with a constant drag coefficient, the mixture behaves similar to that expected from the single-phase problem. The two-phase problem does not have a comparable blasius solution due to a gradient of void fraction across the boundary layer, but it's general behavior is in agreement to what was expected.

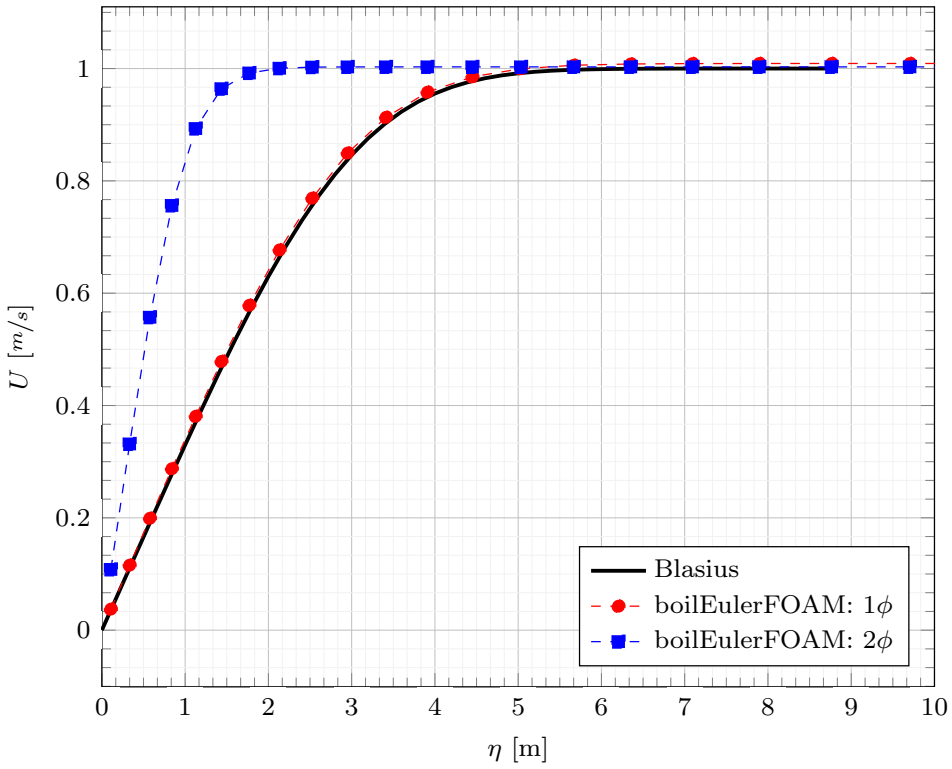

Figure 8.12 Blasius Flat Plate x-direction Velocity Comparison

8.4 Laminar Flow in a Pipe Problem

This numerical test case was used to make sure that our solver could indeed capture the laminar profile of flow in a pipe. This can be simplified to be a two dimensional steady state problem of flow through a 25.4 mm diameter pipe of 4 meters in length. There is no acceleration by gravity, phase change, interfacial forces or turbulence modeled for this problem. Table 8.4 gives the inital, boundary and thermo-physical conditions. As can be seen from Fig. 8.14 it obviously does a good job of doing this. The thermo-physical model used for this problem is the stiffened ideal gas equation of state (e.g. $p = \rho\,(R\,T) - p_0$ where $p_0 = 8.913 \times 10^8$ and $R = 3000$ for water). For this problem, the same value of velocity is applied as fixed value boundary conditions at the inlet of the domain, extrapolated from the interior cell at the outlet boundary and set to a fixed value of 0 (e.g. no slip BC) at the wall. The pressure is set to the value from the table above at the outlet, and extrapolated from the interior cell at all other boundaries. The rest of the values are set to the values

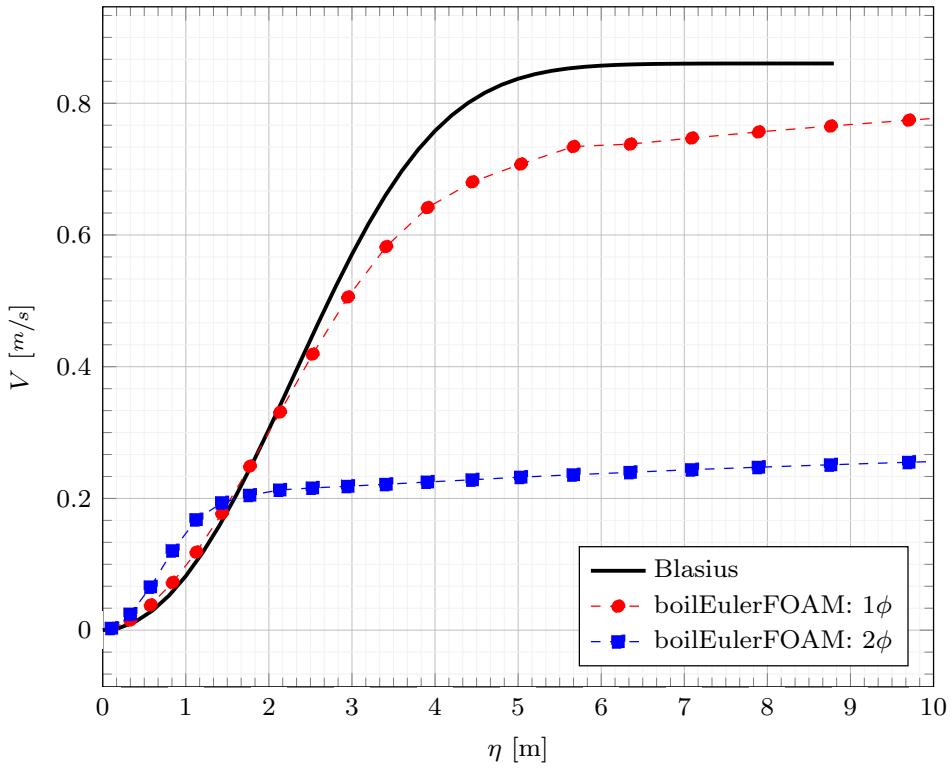

Figure 8.13 Blasius Flat Plate y-direction Velocity Comparison

Table 8.4 Laminar Flow in a Pipe Problem Setup

Parameter	**Variable**	**Value**
Pressure	p	101,300 Pa
Void Fraction	α_2	1.0 [–]
Reynolds Number	Re_2	100 [–]
Velocity	$\mathbf{U}_2$	0.0034988 $\left[\frac{\mathrm{m}}{\mathrm{s}}\right]$
Temperature	T_2	298 [K°]
Dynamic Viscosity	μ_2	8.9313×10^{-3} $\left[\frac{\mathrm{kg}}{\mathrm{m \cdot s}}\right]$
Specific Heat	$C_{p,2}$	4186.0 $\left[\frac{\mathrm{J}}{\mathrm{kg \cdot K}}\right]$
Prandlt Number	Pr_2	6.15305 [–]

from the table above at the inlet boundaries, and extrapolated from the interior cell values everywhere else along the boundary. The results are given in Fig. 8.14. As can be seen from the figure our solver perfoms very well in matching up with the theoretical laminar profile.

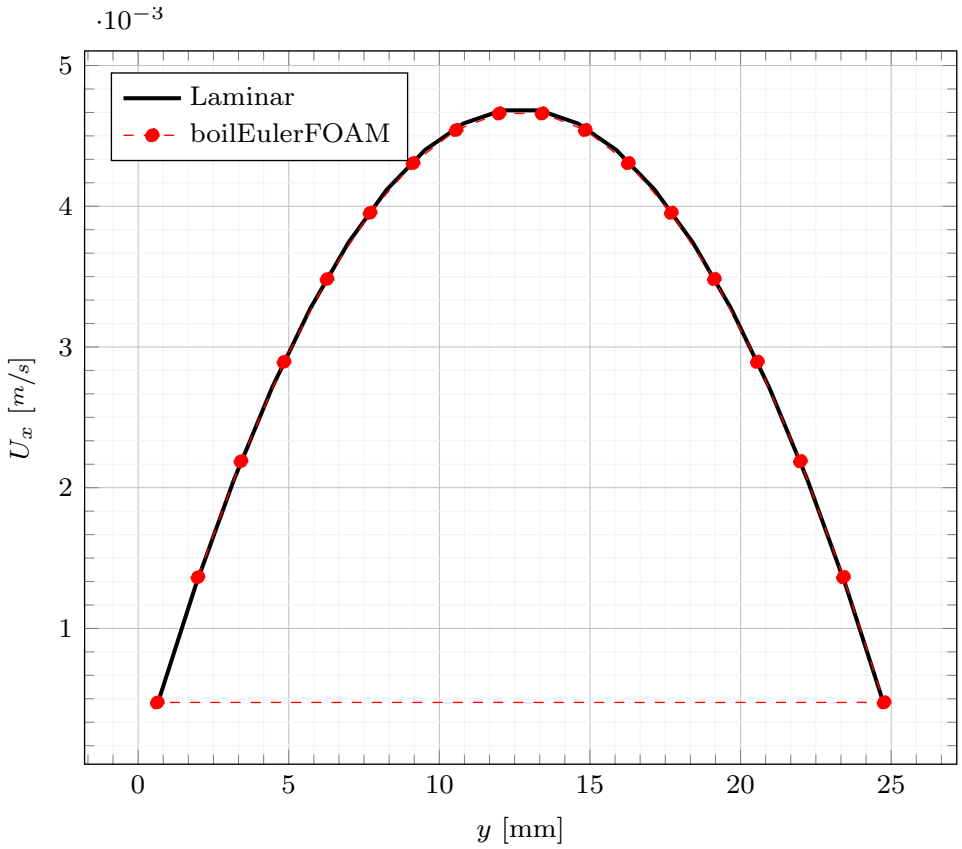

Figure 8.14 Laminar Flow in a Pipe Comparison

This results was also achieved with a fully three-dimensional simulation.

8.5 Purdue Experiments

The following discussion will cover work performed based on the experimental results from Purdue University reported in [37]. The aim of using this study was to assess models for interfacial area concentration and inter-phase momentum transfer and address some preliminary improvements that could be implemented. These experiments help determine the performance of the modeling of the interfacial forces, bulk diameter, and interfacial area concentration in our solver without the added complications introduced from modeling phase change and heat transfer closure terms. Also, the benefit of these adiabatic experiments is the smaller pipe diameter which is on the order of the hydraulic diameters

found in a PWR fuel bundle.

The experiments, in general, can be described as adiabatic water-air upward bubbly/slug flow in vertical pipes at atmospheric pressure and temperature of 25 °C. The vertical pipe was made of what is generally referred to as plexiglass (mostly due to its transparency) and was 3.75 meters long with an inner diameter of 25.4 mm (e.g. 1 inch). The interest in this test case, is that it is an adiabatic test case with a pipe of a smaller diameter, specifically, in comparison to most adiabatic experiments found in literature (e.g. say the MT-Loop experiments). Its use can be justified by the fact that standard hydraulic diameters in fuel bundles of PWR's are typically around this value, if not even smaller. The three-dimensional

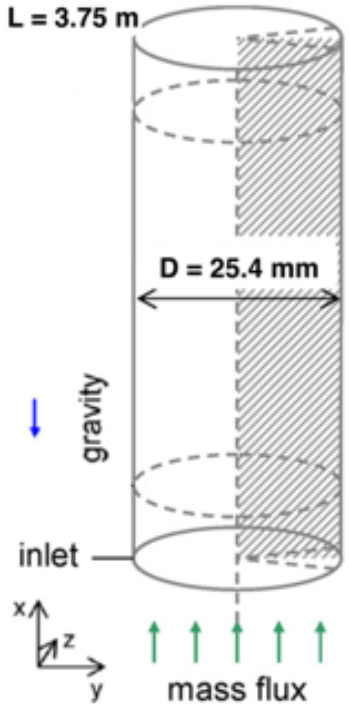

Figure 8.15 Purdue Experiment Geometry

pipe geometry (displayed in Fig. 8.15) was converted to a quasi-two-dimensional geometry by using axis-symmetry and modeling a wedge of the pipe in order to reduce the size of this computational problem. Table 8.5 gives a more general breakdown of the experimental geometry, a general idea of the meshing used, and locations of experimental data extraction for this scientific test cases. To get an idea of the experimental data that can be used to

Table 8.5 Purdue Experiments - Brief Experimental Setup

Property	**Value**
Pipe Diameter	25.4 [mm]
Pipe Length	3.75 [m]
Axial Direction # of Cells	$100-350$ cells
Radial Direction # of Cells	$10-70$ cells
Measurement Locations $\left(\frac{L}{D}\right)$	12, 62, 112

compare our numerical results with, Table 8.6 & Table 8.7 both give a short summary of all the experimental results that were given for two of the studies provided in the thesis [37]. where f_b represents the number of bubbles per second or bubble frequency, L_b is the

Table 8.6 Purdue Experiments - Flow Structure Development Study

Parameter	**Values**
Test Section Inner Diameter (mm)	25.4
Superficial Liquid Velocity, $j_2\left(\frac{\text{m}}{\text{s}}\right)$	0.3, 0.62, 1.1, 2 and 3
Superficial Gas Velocity, $j_1\left(\frac{\text{m}}{\text{s}}\right)$	0.09, 0.16, 0.29, 0.48, 0.69, 0.96 and 1.35
Average Max Void Fraction, α_1	$10\%-50\%$
Axial Position $\frac{L}{D}$ of measurement ports	12, 62, and 112
Instrumentation	Double-sensor Probe
Measurement parameters	$\alpha_1, A_{i,1}, f_b, \mathbf{U}_1$, and D_{sm}
Liquid Reynolds Number, Re_2	$7,600$ to $76,000$

Taylor bubble length, L_u is the slug unit length and δ_{film} is the film thickness at stem of slug bubble. Since our solver is designed for bubbly flow conditions, we need to see the set of experiments in a flow pattern map. According to Taitel el al. [3] the transition line from

Table 8.7 Purdue Experiments - Fully Developed Flow Study

Parameter	Values
Test Section Inner Diameter (mm)	25.4
Superficial Liquid Velocity, $j_2\left(\frac{\text{m}}{\text{s}}\right)$	0.0, 0.1, 0.3, 0.62 and 1.1
Superficial Gas Velocity, $j_1\left(\frac{\text{m}}{\text{s}}\right)$	0.1, 0.2, 0.4, 1.0, 1.4, 2.0 and 3.5
Average Max Void Fraction, α_1	5% − 45%
Axial Position $\frac{L}{D}$ of measurement ports	120
Instrumentation	Thin film, 2 & 4 sensor probe and gamma densiometer
Measurement parameters	α_1, $A_{i,1}$, f_b, $\mathbf{U}_1$, L_b, L_u and δ_{film}
Liquid Reynolds Number, Re_2	0 to 25,000

bubbly flow to slug flow can be represented with the following expression.

$$j_2 = 3.0\, j_1 - 1.15\left[\frac{g\left(\rho_2-\rho_1\right)}{\rho_2^2}\sigma\right]^{\frac{1}{4}} \tag{8.3}$$

So using this relationship, and the superficial velocities we can visualize the flow pattern map given by Fig. 8.16. As can be seen that we have several choices for experiments that are

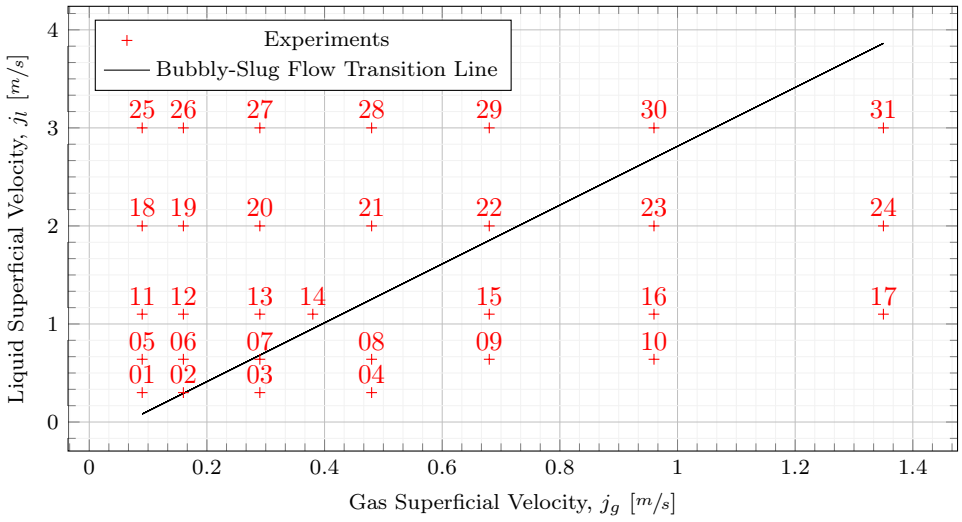

Figure 8.16 Purdue Experiments - Flow Pattern Map

present above the transition line. Currently, we have not simulated many of the experiments that were presented in [37], first for brevity's sake we chose a smaller test matrix of the experiments, these test cases also coincided with those chosen in Ghione's thesis [21] in order to provide us with some examples of numerical results that can be obtained through simulation using similar methods to those employed in our own. Table 8.8 gives a break down of all the experiments that were tested; however, only a single case will be presented in this of work so as to not be overly repetitive and because so far only one case was studied in-depth. The term j is superficial velocity and not actual velocity. The actual physical

Table 8.8 Purdue Experiments - Selected Experiments

Test	$j_2\left(\frac{\mathbf{m}}{\mathbf{s}}\right)$	$j_1\left(\frac{\mathbf{m}}{\mathbf{s}}\right)$	$\max(\langle\alpha\rangle)$
PU01	0.30	0.09	0.25
PU05	0.64	0.09	0.15
PU06	0.64	0.16	0.30
PU11	1.10	0.09	0.17
PU12	1.10	0.16	0.24
PU19	2.00	0.16	0.16

velocities can be deduced from the superficial velocities but using the following relationship,

$$\mathbf{U}_k = j_k \frac{R}{\int_0^R \alpha_k \, d\, r} \tag{8.4}$$

where R is the radius of the pipe. The inlet for this testcase is moved to the axial location of $\frac{L}{D} = 12$ in order to coincide with the experimental data. The trapezoid rule was us used along the pipe radius to get the average inlet values for use in the boundary conditions. Table 8.9 gives the thermo-physical properties for the air and water simulated for this case. For the purposes of these experiments we run the solver with constant properties; however, the density of the dispersed phase (e.g. the air) can be a variable quantity and can be calculated using a constant compressibility constant such that,

$$\rho_1 = \Psi_1 p \tag{8.5}$$

Table 8.9 Purdue Experiments - Thermo-physical Properties

Parameter	**Variable**	**Value**
Pressure	p	$101,300$ [Pa]
Surface Tension	σ	$0.0727 \left[\frac{\mathrm{N}}{\mathrm{m}}\right]$
Air Properties		
Density	ρ_1	$1.1845 \left[\frac{\mathrm{kg}}{\mathrm{m}^3}\right]$
Thermal Conductivity	κ_1	$0.0257 \left[\frac{\mathrm{W}}{\mathrm{m}\cdot\mathrm{K}}\right]$
Dynamic Viscosity	μ_1	$1.7898 \times 10^{-4} \left[\frac{\mathrm{kg}}{\mathrm{m}\cdot\mathrm{s}}\right]$
Specific Heat	$C_{p,1}$	$1004.7 \left[\frac{\mathrm{J}}{\mathrm{kg}\cdot\mathrm{K}}\right]$
Prandlt Number	Pr_1	0.6997 [—]
Water Properties		
Density	ρ_2	$998.21 \left[\frac{\mathrm{kg}}{\mathrm{m}^3}\right]$
Thermal Conductivity	κ_2	$0.5995 \left[\frac{\mathrm{W}}{\mathrm{m}\cdot\mathrm{K}}\right]$
Dynamic Viscosity	μ_2	$1.0012 \times 10^{-3} \left[\frac{\mathrm{kg}}{\mathrm{m}\cdot\mathrm{s}}\right]$
Specific Heat	$C_{p,2}$	$4148.8 \left[\frac{\mathrm{J}}{\mathrm{kg}\cdot\mathrm{K}}\right]$
Prandlt Number	Pr_2	6.9287 [—]

where $\Psi_1 = \frac{1}{\mathrm{R}T} = 1.1693 \times 10^{-5} \left[\mathrm{s}^2 \cdot \mathrm{m}^{-2}\right]$. The density can also be calculated using ideal gas law, stiffened ideal gas law, and various other methods. The low speed flow of this problem means that compressibility effects of the continuous or liquid phase (e.g. the water) do not need to be taken into account. The boundary conditions for the experiments we have chosen are given in Table 8.10. The uniform fixed inlet values and initial conditions for void fraction, interfacial area concentration, bubble diameter, velocity, turbulent kinetic energy, and turbulent energy dissipation rate are found by using the $\frac{L}{D} = 12$ value of the experimental data. The constant value for the turbulent kinetic energy and the turbulent energy dissipation are calculated with approximate formulation for rounds pipes taken from [21]. The inlet value for the turbulent kinetic energy is given by the following formulation,

$$k_2 = \frac{3}{2}(\mathbf{U}_2 I)^2 \tag{8.6}$$

Table 8.10 Purdue Experiments - Boundary Conditions

Parameter	Inlet	Outlet	Wall
Temperature	∘	×	×
Velocity	×	∘	×
Pressure	∘	×	∘
Void Fraction	∘	×	×

∘ - Dirichlet Condition

× - Neumann Condition

where the turbulence intensity is given by,

$$I = 0.16\mathrm{Re}_{D_h}^{-\frac{1}{8}} \tag{8.7}$$

where the Reynolds number for the hydraulic diameter (taken to be the pipe diameter in this case) is given by,

$$\mathrm{Re}_{D_h} = \frac{\rho_2 \mathbf{U}_2 D_h}{\mu_2} \tag{8.8}$$

The inlet value for turbulent energy dissipation is set by using the following formulation,

$$\epsilon_2 = C_\mu \frac{k_2^{\frac{3}{2}}}{L} \tag{8.9}$$

where the turbulent length scale for fully developed flow in a pipe is given by the following definition,

$$L = 0.038 D_h \tag{8.10}$$

The radial distributions of gas phase velocity, void fraction, interfacial area concentration, and bubble diameter experimental data are going to be used to assess the accuracy and performance of our solver. On top of the experimental data, the commercial solver Star-CCM+ will be used as a reference comparison tool as well. The modeling setups used in the Star-CCM+ solver runs are typically not the most accurate or generally very good at matching the experimental results; however, we are employing Star-CCM+ and those model setups to make sure that when our solver is run with a matching (fairly close typically but not identical as we do not have some of the models that Star-CCM+ employs and vice versa)

we get similar results and behavior which leads to an increase in the confidence of our solver's performance.

For this set of experiments we have some Star-CCM+ data so it is necessary to give the Star-CCM+ setup that was used to obtain that data. The Star-CCM+ setup is given by Table 8.11. Just to reiterate, the results obtained from Star-CCM+ were not done with the

Table 8.11 Purdue Experiments - Star-CCM+ Closure Modeling Summary

Closure Model	**Option**	**Details**
Diameter Model	S-Gamma	$D_{b,1} = \frac{6\alpha_1\alpha_2}{A_{i,1}}$
Drag Model	Tomiyama	–
Lift Model	Constant	$C_l = 0.01$
Wall Lubrication Model	Antal	$C_{w1} = -0.01$ and $C_{w2} = 0.05$
Turbulence Dispersion Model	Default	$C_{td} = 1.0$
Virtual Mass Model	Constant	$C_{vm} = 0.5$
Turbulence Model	$k-\epsilon$ Equations	$C_t = 1.0$, $\mathrm{Pr}_2^t = 0.9$, $C_b = 1.2$ and $C_\mu = 0.09$
Equation of State	Constant	–

aim to get good agreement with the experimental data, but more in order to be able to replicate the results with our solver and again, there are a few models in Star-CCM+ that we do not have coded into our solver. The first of these models is the use of what Star-CCM calls the "S-Gamma" interfacial area concentration model. We have only the Interfacial Area Concentration equation developed by Hibiki & Ishii [27] with a few options on the modeling of the interfacial area concentration break-up and coalescence source terms. Another difference is in the modeling of the turbulence dispersion interfacial momentum force term; our solver has a correlation similar to the default method in Star-CCM, this method employs farve averaging of the drag coefficient much like the Star-CCM+ method and was developed by Burns [57]. The rest of the basic / pertinent settings are given Table 8.11 for Star-CCM+. The reference setup for our solver is given in Table 8.12. Now lets first review the direct comparison between our results, Star-CCM+ and the experimental results for the PU01 experimental conditions at the axial location of $\frac{L}{D} = 62$ displayed in Fig. 8.17. An

Table 8.12 Purdue Experiments - Reference Closure Model Summary

Closure Model	**Option**	**Details**
Diameter Model	IAC	$D_{b,1} = \frac{6\alpha_1}{A_{i,1}}$
Coalescence Model	Hibiki & Ishii	$K_C = 1.29$, $\alpha_{\max} = 0.74$ and Γ_C (adjustable)
Break-up Model	Hibiki & Ishii	$K_B = 1.59$, $\alpha_{\max} = 0.74$ and Γ_B (adjustable)
Drag Model	Tomiyama	–
Lift Model	Constant	$C_l = 0.01$
Wall Lubrication Model	Antal	$C_{w1} = -0.01$ and $C_{w2} = 0.05$
Turbulence Dispersion Model	Burns	$C_{td} = 1.0$ and $\sigma_t = 1.0$
Virtual Mass Model	Constant	$C_{vm} = 0.5$
Turbulence Model	$k-\epsilon$ Equations	$C_t = 1.0$, $\mathrm{Pr}_2^t = 0.9$, $C_b = 1.2$ and $C_\mu = 0.09$
Equation of State	Constant	–

inspection of the figure shows similar trends and fairly good agreement between our solver and the commercial CFD package Star-CCM+, especially with regard to the gas velocity (the top right figure). The differences in the interfacial area concentration (the lower left figure) are thought to be due to a symmetric relation being used by default in Star-CCM+ and one which is not in our solver, this difference would affect the calculated bubble diameter and thus the void distribution due to differences in the interfacial force terms. It is important to note that the setups chosen for this case are not to produce the best comparison with the experimental data (the black lines in the figures), but to provide the best comparison of the baseline functionality with Star-CCM+. Now lets move onto some different investigations into the performance of our solver using a similar setup. First we will look at the results of a radial grid refinement study. We ran the exact same setup for three values of grid refinement in the radial direction (e.g. 10, 20 and 40 cells uniformly distributed across the radius of the quasi two-dimensional computational domain). Fig. 8.18 displays the results of the comparison. As can be seen from an inspection of the figure, the void distributions (top left) remain very similar to each other, except for small deviations along the wall (e.g. the right hand side of the graph). These deviations are likely due to the grid dependency of the Antal wall lubrication model and the non-symmetric nature of the interfacial area

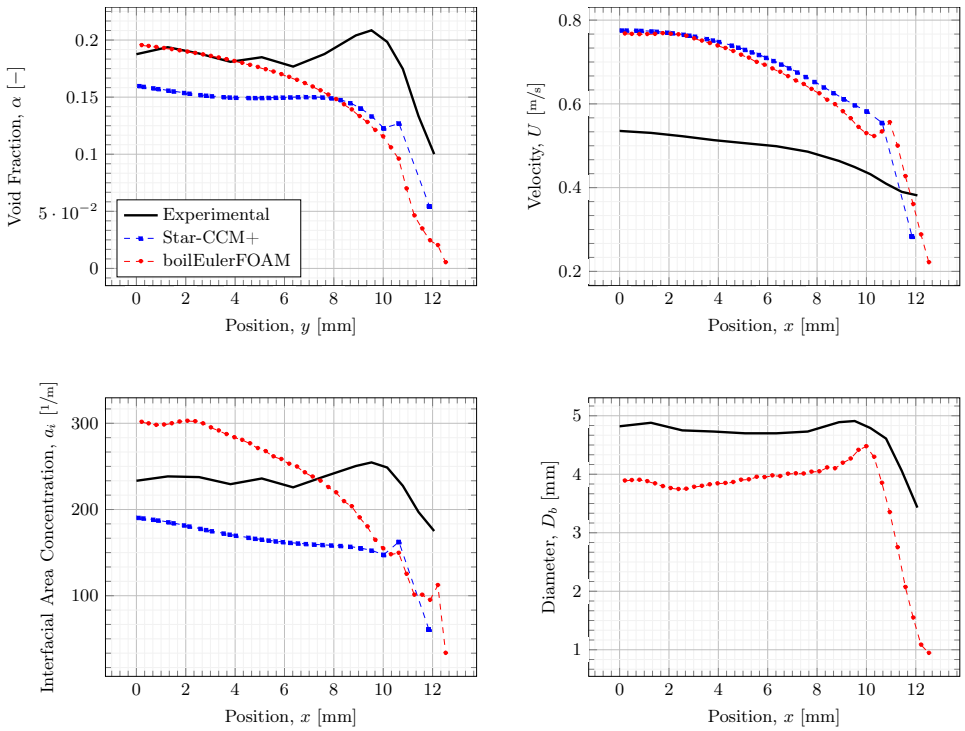

Figure 8.17 Purdue Experiments - PU01 Star-CCM+ Comparison

concentration diameter model used in our solver. It can be seen that the bubble diameter for the lowest refined case does not decrease when approaching the walls, this is likely due to the refinement not being great enough to capture the interfacial model behavior along the wall. Ghione and Rusche [21, 49] discussed the benefits of the implementation of a Rhie-chow like interfacial lift force treatment and the moving of the evaluation of the turbulence dispersion force and lift force to the pressure equation inside the PISO loop to remove checker-boarding in the radial distributions. We implemented both the standard approach and the approach discuss by Ghione and Rusche [21, 49]. As can be seen from an inspection of Fig. 8.19 and Fig. 8.20 the implementation of the new treatment significantly smooths out both the void fraction radial distribution in Fig. 8.19 and the interfacial area concentration radial distribution in Fig. 8.20. Due to the fact that Ghione [21] gave the direct coding performed for the implementation of this method into a similar version of OpenFOAM, the addition of this method was fairly straight forward; however, there were some difficulties initially due to the original coding misrepresenting some quantities. Further examples of the benefits and drawbacks of the implementation and details regarding the reasoning

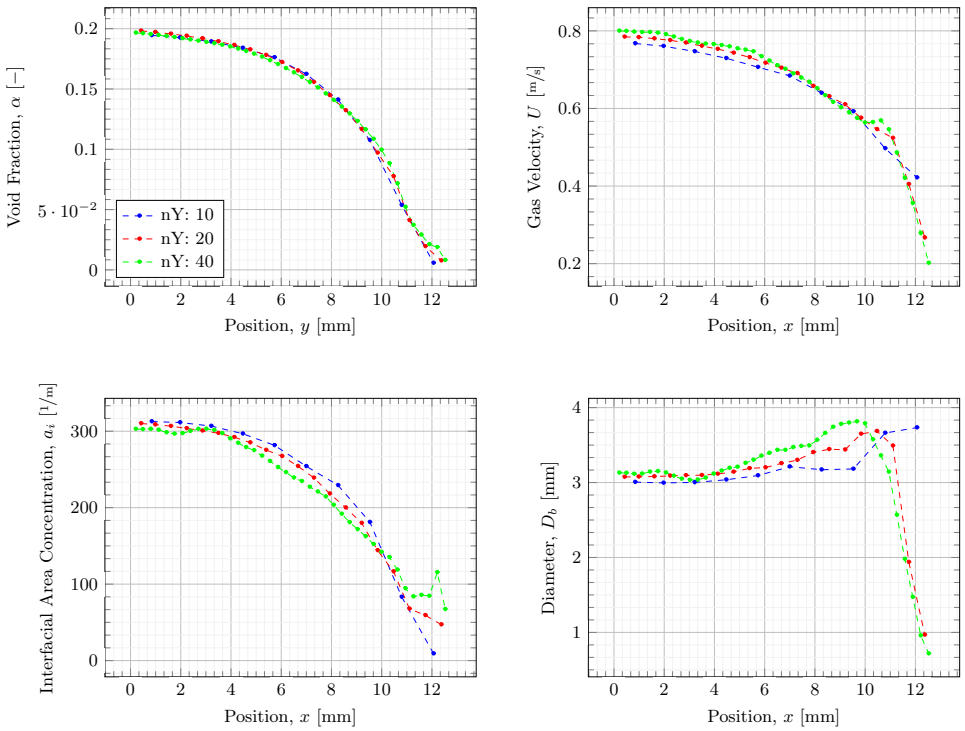

Figure 8.18 Purdue Experiments - PU01 Grid Refinement

behind the implementation of this method Ghione and Rusche do a remarkable job [21, 49].

8.6 MT-Loop Experiments

The following will cover the general description of the MT-Loop testing facility and the experimental testcases that were performed in [45]. The aim of using this study, much like the Purdue experiments, was to assess models for interfacial area concentration and inter-phase momentum transfer and address some preliminary improvements that could be implemented. These experiments help determine the performance of the modeling of the interfacial forces, bulk diameter, and interfacial area concentration in our solver without the added complications introduced from modeling phase change and heat transfer closure terms. Also, the benefit of these adiabatic experiments is the different pipe diameter from the Purdue experiments which helps an investigation if the larger pipe (e.g. approximate twice as large) diameter affects the performance of the solver.

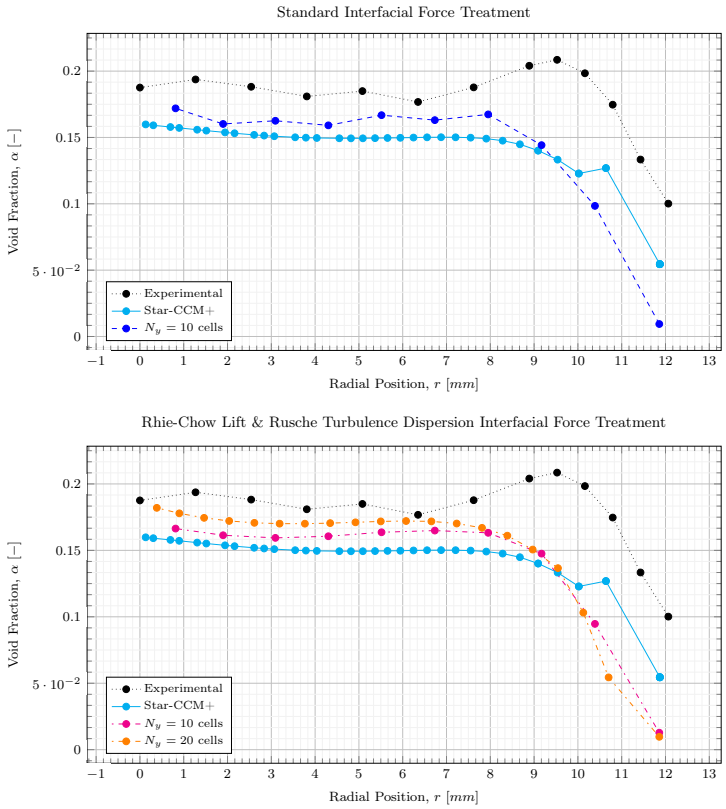

Figure 8.19 Purdue Experiments - PU01 Void Fraction Comparison

The experiments, in general, can be described as adiabatic water-air upward bubbly/slug flow in vertical pipes at essentially atmospheric pressure and temperature. The vertical pipe was 3.5 meters long with an inner diameter of 51.2 mm (e.g. approximately 2 inches). The interest in this test case, is that it is an adiabatic test case with a pipe of a larger diameter, specifically, in comparison to previously discussed adiabatic experiments. The pipe that the experiment takes place in is vertical and the flow is from bottom towards the tops so that gravity and bouyancy effects play an important role. The three-dimensional pipe geometry (displayed in Table 8.21) was converted to a quasi-two-dimensional geometry by using axis-symmetry and modeling a wedge of the pipe in order to reduce the size of this computational problem. Table 8.13 gives a more general breakdown of the experimental geometry, a general idea of the meshing used, and locations of experimental data extraction for this scientific test cases. There are a large number of different experimental conditions available in the literature. The measured set of the superficial velocity combinations for

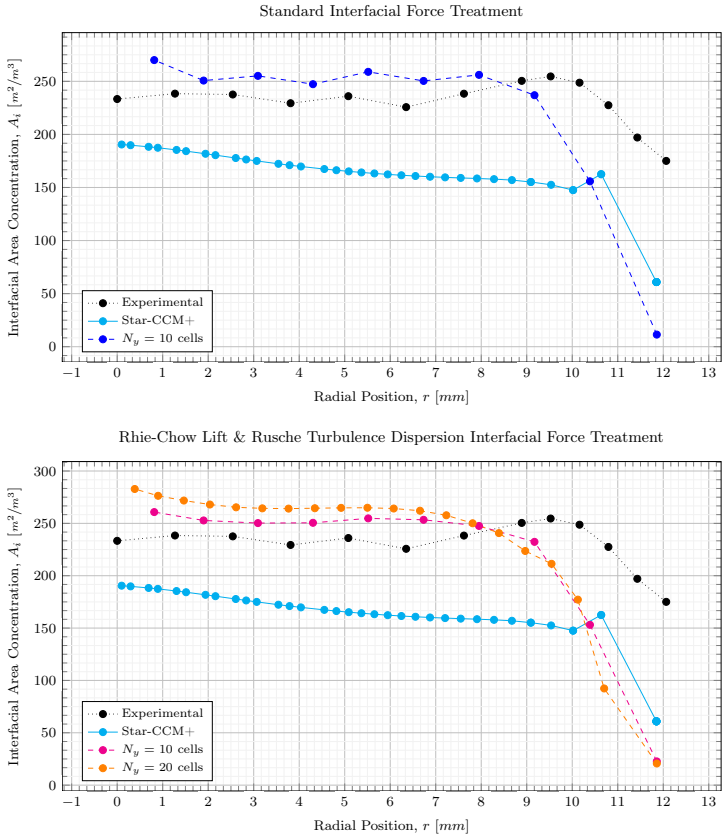

Figure 8.20 Purdue Experiments - PU01 Interfacial Area Conc. Comparison

Table 8.13 MT-Loop Experiments - Brief Experimental Setup

Property	**Value**
Pipe Diameter	51.2 [mm]
Pipe Length	3.5 [m]
Axial Direction # of Cells	100 − 350 cells
Radial Direction # of Cells	10 − 70 cells
Measurement Locations $\left(\frac{L}{D}\right)$	59.2

both the gas and liquid phases and the assignment of groups of cappilaries used for gas injection for this experiment can be seen in Fig. 8.22. The corresponding measured flow pattern map at the upper end of the pipe $\left(\frac{L}{D} = 59.2\right)$ for the fully developed profile of the multiphase flow for each of the experiments can be seen in Fig. 8.23. As is evident there are

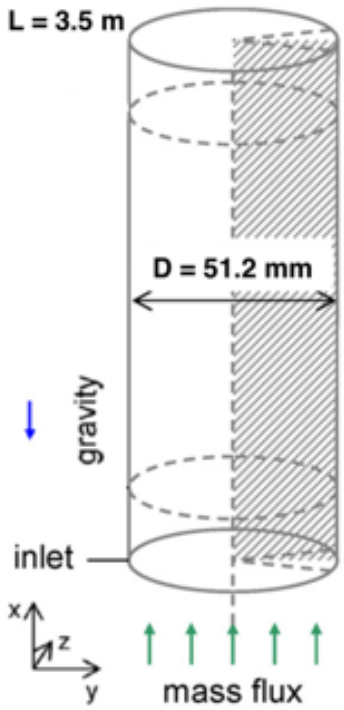

Figure 8.21 MT-Loop Experiments - Test Section Geometry

Water Superficial Velocity	Air Superficial Velocity												
	J / m/s	0.0025	0.0040	0.0062	0.0096	0.0151	0.0235	0.0368	0.0574	0.0898	0.140	0.219	0.342	0.534
	4.047	11	22	33	44	55	66	77	88	99	110	121	132	143
	2.554	10	21	32	43	54	65	76	87	98	109	120	131	142
	1.611	9	20	31	42	53	64	75	86	97	108	119	130	141
	1.017	8	19	30	41	52	63	74	85	96	107	118	129	140
	0.641	7	18	29	40	51	62	73	84	95	106	117	128	139
	0.405	6	17	28	39	50	61	72	83	94	105	116	127	138
	0.255	5	16	27	38	49	60	71	82	93	104	115	126	137
	0.161	4	15	26	37	48	59	70	81	92	103	114	125	136
	0.102	3	14	25	36	47	58	69	80	91	102	113	124	135
	0.0641	2	13	24	35	46	57	68	79	90	101	112	123	134
	0.0405	1	12	23	34	45	56	67	78	89	100	111	122	133
	0	N01	N02	N03	N04	N05	N06	N07	N08	N09	N10	N11	N12	N13

Group of capillaries 1
Group of capillaries 2
Groups of capillaries 1 + 2
Groups of capillaries 2 + 3
Groups of capillaries 1 + 2 + 3
Groups of capillaries 1 +2 + 4
All capillaries

Figure 8.22 MT-Loop Experiments - Matrix of superficial velocities and Capillary Groups [45]

numerious experimental setups from the MT-Loop testing facility that can be used in the validation and verification of the functionality of our solver. Table 8.14 will give a summary of the selected experimental conditions that have been chosen thus far in the validation

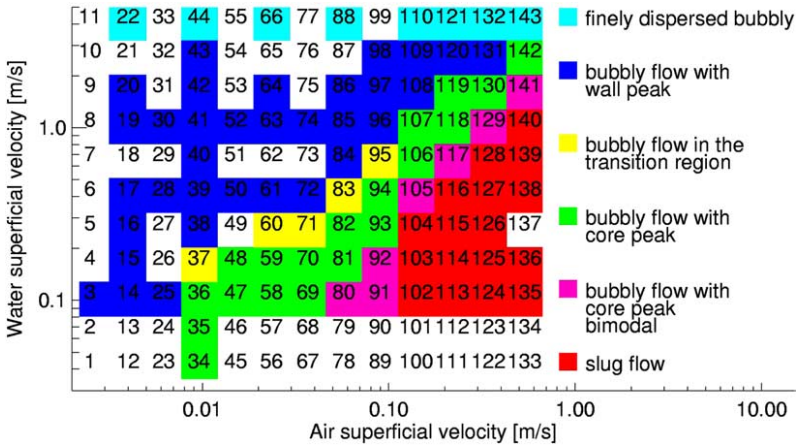

Figure 8.23 MT-Loop Experiments - Flow Pattern Map

for our solver; however, only two experimental testcase will be discuss to avoid repition and because only those two were studied in depth. Again, the term j is superficial velocity

Table 8.14 MT-Loop Experiments - Selected Experiments

Test	$j_2\left(\frac{\mathbf{m}}{\mathbf{s}}\right)$	j_1 (**nominal**)$\left(\frac{\mathbf{m}}{\mathbf{s}}\right)$	j_1 (**adjust.**)$\left(\frac{\mathbf{m}}{\mathbf{s}}\right)$	$\left\langle D_{b,1}\right\rangle$(**mm**)	$\langle\alpha\rangle$(%)
MT017	0.4050	0.0040	0.0033	4.25	0.60
MT019	1.0167	0.0040	0.0429	4.00	0.28
MT039	0.4050	0.0096	0.0111	4.50	1.89
MT041	1.0167	0.0096	0.0115	4.50	1.00
MT061	1.4050	0.0235	0.0309	4.50	5.03
MT063	1.0167	0.0235	0.0316	4.50	2.64

and not actual velocity. The actual physical velocities can be deduced from the superficial velocities but using the following relationship,

$$\mathbf{U}_k = \frac{j_k}{\langle\alpha_k\rangle} \tag{8.11}$$

where $\langle\cdot\rangle$ represents the average across the radius of the pipe. Table 8.15 gives the thermo-

physical properties for the air and water simulated for this case. For the purposes of these

Table 8.15 MT-Loop Experiments - Thermo-physical Properties

Parameter	**Variable**	**Value**
Pressure	p	$101,300$ [Pa]
Surface Tension	σ	$0.0727 \left[\frac{\text{N}}{\text{m}}\right]$
Air Properties		
Density	ρ_1	$1.1845 \left[\frac{\text{kg}}{\text{m}^3}\right]$
Thermal Conductivity	κ_1	$0.0257 \left[\frac{\text{W}}{\text{m}\cdot\text{K}}\right]$
Dynamic Viscosity	μ_1	$1.7898 \times 10^{-4} \left[\frac{\text{kg}}{\text{m}\cdot\text{s}}\right]$
Specific Heat	$C_{p,1}$	$1004.7 \left[\frac{\text{J}}{\text{kg}\cdot\text{K}}\right]$
Prandlt Number	Pr_1	0.6997 [—]
Water Properties		
Density	ρ_2	$998.21 \left[\frac{\text{kg}}{\text{m}^3}\right]$
Thermal Conductivity	κ_2	$0.5995 \left[\frac{\text{W}}{\text{m}\cdot\text{K}}\right]$
Dynamic Viscosity	μ_2	$1.0012 \times 10^{-3} \left[\frac{\text{kg}}{\text{m}\cdot\text{s}}\right]$
Specific Heat	$C_{p,2}$	$4148.8 \left[\frac{\text{J}}{\text{kg}\cdot\text{K}}\right]$
Prandlt Number	Pr_2	6.9287 [—]

experiments we run the solver with constant properties; however, as explained previously, the density of the dispersed phase (e.g. the air) can be a variable quantity and can be calculated using a constant compressibility constant, ideal gas law, stiffened ideal gas law, and various other methods. The low speed flow of these experiments means that compressibility effects of the continuous or liquid phase (e.g. the water) do not need to be taken into account. The boundary conditions for the experiments we have chosen are given in Table 8.16. The uniform fixed inlet values and initial conditions for void fraction, interfacial area concentration, bubble diameter, velocity, turbulent kinetic energy, and turbulent energy dissipation rate are found by using the given experimental data. As explained previously, the constant value for the turbulent kinetic energy and the turbulent energy dissipation are calculated with approximate formulation for rounds pipes taken from [21].

Table 8.16 MT-Loop Experiments - Boundary Conditions

Parameter	Inlet	Outlet	Wall
Temperature	∘	×	×
Velocity	×	∘	×
Pressure	∘	×	∘
Void Fraction	∘	×	×

∘ - Dirichlet Condition

× - Neumann Condition

The inlet value for the turbulent kinetic energy is given by the following formulation,

$$k_2 = \frac{3}{2}(\mathbf{U}_2 I)^2 \tag{8.12}$$

where the turbulence intensity is given by,

$$I = 0.16\mathrm{Re}_{D_h}^{-\frac{1}{8}} \tag{8.13}$$

where the Reynolds number for the hydraulic diameter (taken to be the pipe diameter in this case) is given by,

$$\mathrm{Re}_{D_h} = \frac{\rho_2 \mathbf{U}_2 D_h}{\mu_2} \tag{8.14}$$

The inlet value for turbulent energy dissipation is set by using the following formulation,

$$\epsilon_2 = C_\mu \frac{k_2^{\frac{3}{2}}}{L} \tag{8.15}$$

where the turbulent length scale for fully developed flow in a pipe is given by the following definition,

$$L = 0.038 D_h \tag{8.16}$$

Currently, the only available experimental data that has been used for comparison is the radial void fraction profile at a height of 3.03 m $\left(\frac{L}{D} = 59.2\right)$ from the bottom of the vertical pipe. Thus this will be the sole basis of comparison for all our results for the time being. For this set of experiments we have some Star-CCM+ radial void fraction data so it is necessary

to give the Star-CCM+ setup that was used to obtain that data. The Star-CCM+ setup is given in Table 8.17. Just to reiterate, the results obtained from Star-CCM+ were not done

Table 8.17 MT-Loop Experiments - Star-CCM+ Closure Modeling Summary

Closure Model	**Option**	**Details**
Diameter Model	Constant	$D_{b,1} = \langle D_{b,1} \rangle$
Drag Model	Tomiyama	–
Lift Model	Constant	$C_l = 0.05$
Wall Lubrication Model	Antal	$C_{w1} = -0.01$ and $C_{w2} = 0.05$
Turbulence Dispersion Model	Default	$C_{td} = 1.0$
Virtual Mass Model	Constant	$C_{vm} = 0.5$
Turbulence Model	$k-\epsilon$ Equations	$C_t = 1.0$, $\mathrm{Pr}_2^t = 0.9$, $C_b = 1.2$ and $C_\mu = 0.09$
Equation of State	Constant	–

with the aim to get good agreement with the experimental data, but more in order to be able to replicate the results with our solver and again, there are a few models in Star-CCM+ that we do not have coded into our solver. The first of these models is the use of what Star-CCM calls the "S-Gamma" interfacial area concentration model. We have only the Interfacial Area Concentration equation developed by Hibiki & Ishii [27] with a few options on the modeling of the interfacial area concentration break-up and coalescence source terms. However, in this scientific testcase we used a constant diameter in hopes to see the effect that the use of the S-Gamma model had on the other test cases run. Another difference is still in the modeling of the turbulence dispersion interfacial momentum force term; our solver has a correlation similar to the default method in Star-CCM, this method employs farve averaging of the drag coefficient much like the Star-CCM+ method and was developed by Burns [57]. The rest of the basic / pertinent settings are given Table 8.17 for Star-CCM+. The reference setup for our solver is given in Table 8.18. Two sets of results for the MT017 experimental conditions are given in Fig. 8.24 and Fig. 8.25 with a comparison between our solver results and those achieved using a similar setup in Star-CCM+. The respective differences between the results are in interfacial closure modeling of the wall

Table 8.18 MT-Loop Experiments - Reference Closure Model Summary

Closure Model	Option	Details
Diameter Model	Constant	$D_{b,1} = \langle D_{b,1} \rangle$
Drag Model	Tomiyama	–
Lift Model	Constant	$C_l = 0.05$
Wall Lubrication Model	Antal	$C_{w1} = -0.01$ and $C_{w2} = 0.05$
Turbulence Dispersion Model	Burns	$C_{td} = 1.0$
Virtual Mass Model	Constant	$C_{vm} = 0.5$
Turbulence Model	$k-\epsilon$ Equations	$C_t = 1.0$, $\mathrm{Pr}_2^t = 0.9$, $C_b = 1.2$ and $C_\mu = 0.09$
Equation of State	Constant	–

lubrication force coefficients for the Antal Wall lubrication closure model. Fig. 8.24 results

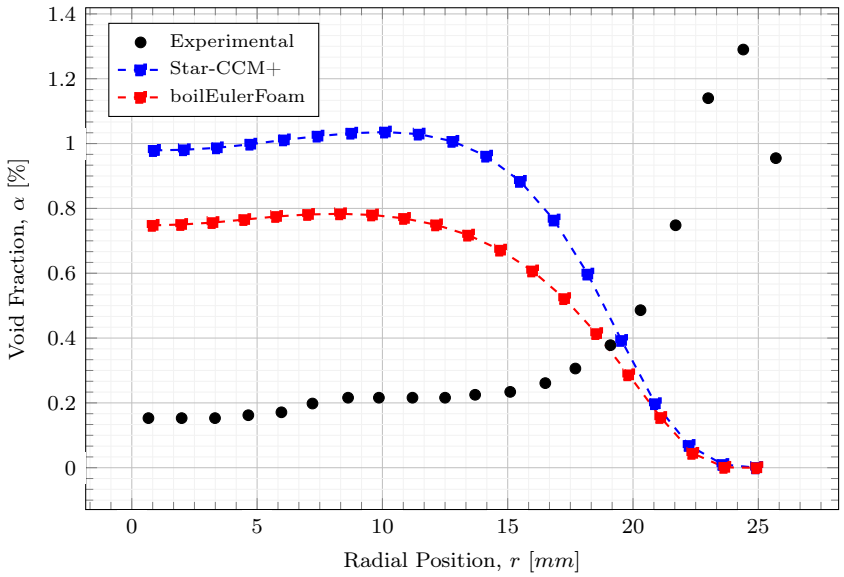

Figure 8.24 MT-Loop Experiments MT017 Comparison - Coefficient Ratio 5

were achieved with the reference coefficients of $C_{w1} = -0.01$ and $C_{w2} = 0.05$ and Fig. 8.25 results were achieved with the coefficients of $C_{w1} = -0.104$ and $C_{w2} = 0.147$. It can be seen

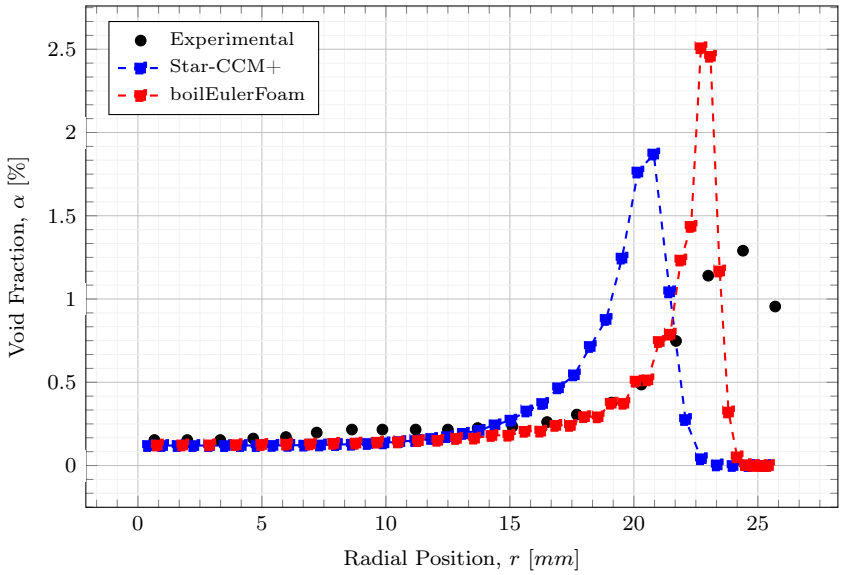

Figure 8.25 MT-Loop Experiments MT017 Comparison - Coefficient Ratio 1.5

from a comparison of the two figures that there is an good agreement in trends between Star-CCM+ and our solver for both setups. These results were given to display the sensitivity of this solution to just a small change in ratio of the wall lubrication force, the first figures coefficients are the typical values used in boiling cases when employing Antal's wall model (a ratio of about 5) and second figures coefficients are those recommended for use in this case (a ratio of about 1.5). As can be seen slight changes in closure modeling of just the wall lubrication force yielded large changes in results, thus, the careful consideration of sensitivity and uncertainty of closure modeling for quantities of interest is a must as these could potentially have large affects on the accuracy and stability of the method.

Now, another set of experimental conditions represented by the description of MT061 are displayed here as well. Fig. 8.26 displays the comparison between our results, Star-CCM+ and the experimental results. It can be seen that there is an excellent agreement between Star-CCM+ and our solver for the MT061 case displayed in Fig. 8.26 with the higher average inlet void fraction. This case also displays one of the short comings of mono-dispersed bubbly flow methods. Due to only employing a single bubble size distribution in the solver it makes it difficult to model radial distributions of void fraction with both near wall peaks and higher center-line void fractions. Poly-dispersed (MUSIG) methods were developed with this capability in mind; however, they require solving a different set of

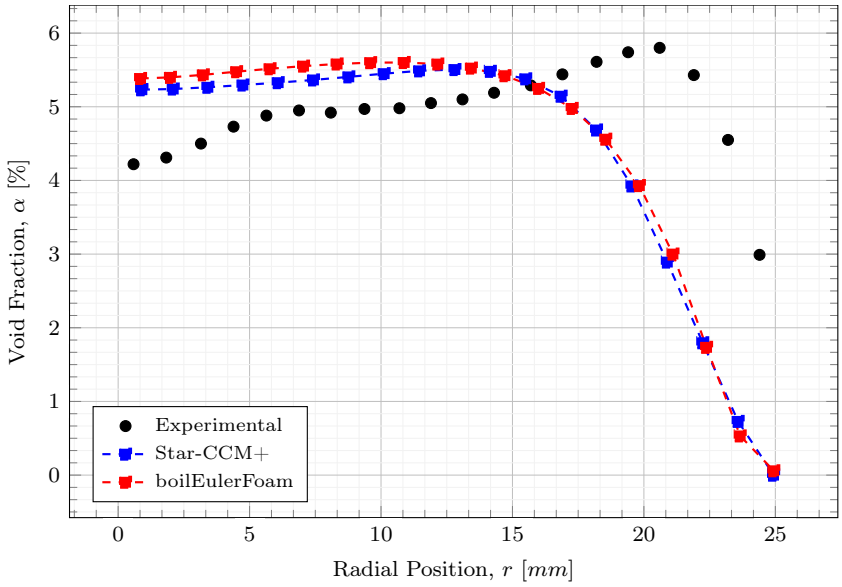

Figure 8.26 MT-Loop Experiments MT061 Void Fraction Comparison

phase momentum conservation equations for each bubble size group and add a significant degree of complexity. Also, for higher pressure boiling flows, the benefits of modeling poly-dispersed bubbly flows is not significant as the bubbles tend to be very small and with most located near the wall. It is also important to note again, that the setups chosen for this case are not to produce the best comparison with the experimental data (given in the figure as the black dots), but the best comparison of functionality with Star-CCM+.

8.7 Bartolomej Experiments

The Bartolomej experiments of a vertical heated pipe with water at high pressure flowing through it from bottom to top. These experiments are sub-cooled boiling flow experiments with relatively high void fraction production. The experimental conditions are fairly close to those that would be modeled in PWR simulations and thus an accurate modeling of these results is the basis for one of the potential end-goals of this work. As previously mentioned, Bartolomej's experiments consist of subcooled water at high pressures flowing up a vertical pipe with a uniform heat flux added to the walls. These types of flow problems give a method to test the functionality of all of the closure models, but especially, the phase change closure modeling methods. The pipe diameter for these experiments is similar to that of a PWR

fuel bundle hydraulic diameter. The geometry description for this problem is given in Fig. 8.27. The three-dimensional pipe geometry was converted to a quasi-two-dimensional

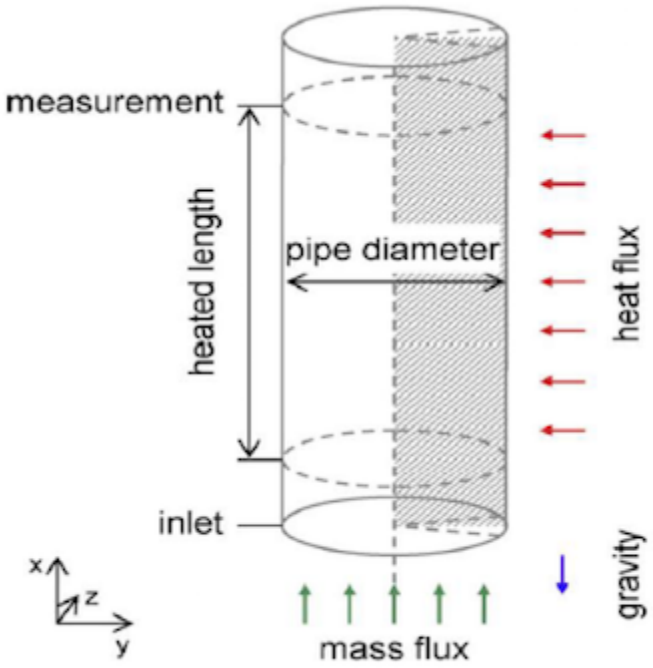

Figure 8.27 Bartolomej Experiments - Test Section Geometry

geometry by using axis-symmetry and modeling a wedge of the pipe in order to reduce the size of this computational problem. There are several sets of experimental conditions in the literature, and a description of the different experimental conditions found in [8, 13] can be seen in Table 8.19. For these experiments there is no radial profile data available for void fraction, interfacial area or bubble diameter, which makes it difficult to assess the correct closure modeling implementation for things like the interfacial forces and interfacial area concentration methods. The experimental data that is currently available and used for validation of the solver, and also that is used as a basis of comparison between our solver in the OpenFOAM framework and commerical packages like Star-CCM+ is given by Table 8.20. There are 7 sets of experimental conditions known for Bartolomej's experiments which display varying degrees of sub-cooling, pressure, mass flux and wall heat flux. Table 8.21 gives the thermo-physical properties needed in order to simulate the BART07 case, which

Table 8.19 Bartolomej Experiments - Selected Experiments

Test	T_{sub} (°**K**)	T_{in} (°**K**)	p (**MPa**)	D_h (**mm**)	$G\left(\frac{\mathbf{kg}}{\mathbf{m}^2\cdot\mathbf{s}}\right)$	$q''_{wall}\left(\frac{\mathbf{kW}}{\mathbf{m}^2}\right)$
BART01	22.6	450.55	1.5	24.0	890	380
BART02	50.9	422.25	1.5	24.0	890	790
BART03	25.0	483.15	3.0	24.0	890	380
BART04	48.1	460.05	3.0	24.0	890	790
BART05	24.0	504.15	4.5	24.0	890	380
BART06	50.0	478.15	4.5	24.0	890	790
BART07	64.5	465.50	4.5	15.4	900	570

Table 8.20 Bartolomej Experiments - Available Experimental Data

Experimental Axial Distribution Data	**Variable**
Cross-sectionally averaged void fraction	α_1
Wall superheat / temperature	T_{sup} or T_{wall}
Cross-sectionally averaged liquid subcooling / temperature	T_{sub} or T_2

is the only case that was examined in detail for this set of experiments. All the values in the table and through-out this work, unless otherwise specified by the description of the experiment, were found on NIST website. It is important to note that when using constant properties for an equation of state the liquid properties can be taken at the saturation condition, at the inlet temperature or an average of the two; however, the velocity must be calculated with the density to ensure the correct mass flux. The heat of formation must be calculated in order to ensure that,

$$h_{sat,k} = C_{p,k} T_{sat} + H_{f,k} \tag{8.17}$$

For the purposes of these experiments we run the solver with constant properties; however, as explained previously, the density of the vapor phase can be a variable quantity and can be calculated using a constant compressibility constant, ideal gas law, stiffened ideal gas law, and various other methods. The initial solver contained an implementation of a

Table 8.21 Bartolomej Experiments - Thermo-physical Properties

Parameter	**Variable**	**Saturation**	**Inlet**
Pressure	p [MPa]	4.5	4.5
Temperature	T [°K]	530.59	465.5
Vapor Properties			
Density	$\rho_1 \left[\frac{\text{kg}}{\text{m}^3}\right]$	22.697	–
Dynamic Viscosity	$\mu_1 \left[\frac{\text{kg}}{\text{m·s}}\right]$	1.7777×10^{-5}	–
Specific Heat	$C_{p,1} \left[\frac{\text{J}}{\text{kg·K}}\right]$	4227.0	–
Prandlt Number	Pr_1 [–]	1.4099	–
Enthalpy	$h_1 \left[\frac{\text{J}}{\text{kg}}\right]$	2.7979×10^6	–
Heat of Formation	$H_{f,1} \left[\frac{\text{J}}{\text{kg}}\right]$	5.5510×10^5	–
Liquid Properties			
Density	$\rho_2 \left[\frac{\text{kg}}{\text{m}^3}\right]$	787.62	875.72
Dynamic Viscosity	$\mu_2 \left[\frac{\text{kg}}{\text{m·s}}\right]$	1.2079×10^{-4}	1.4074×10^{-4}
Specific Heat	$C_{p,2} \left[\frac{\text{J}}{\text{kg·K}}\right]$	4954.1	4441.8
Prandlt Number	Pr_2 [–]	0.83149	0.93275
Enthalpy	$h_2 \left[\frac{\text{J}}{\text{kg}}\right]$	1.1222×10^6	8.1935×10^5
Heat of Formation	$H_{f,2} \left[\frac{\text{J}}{\text{kg}}\right]$	-1.5064×10^6	-1.2483×10^6
Interphase Properties			
Surface Tension	$\sigma \left[\frac{\text{N}}{\text{m}}\right]$	0.024292	–
Latent Heat	$h_{21} \left[\frac{\text{J}}{\text{kg}}\right]$	1.6757×10^6	–

table lookup from the IAPWS free-steam tables to calculate all the needed thermo-physical properties as functions of pressure and temperature; however, it was removed during initial stages of the development process as it affected the OpenFOAM library source code functionality and was extremely slow (approximately taking 10-20 times longer for computation). This was mainly due to the fact that it performed dozens of look-ups and interpolations per iteration in the overall solution process. The functionality will be added back in the future, but with improvements to significantly reduce the computational effort and to not affect the OpenFOAM source code installation. The low speed flow of these experiments means that compressibility effects of the liquid phase (e.g. the water) do not need to be

taken into account; however, changes in temperature will still affect the density but, this is often neglected due to computational effort and the extreme difficulty to reach stable solutions because of the high non-linearity of the problem. The boundary conditions for the experiments we have chosen are given in Table 8.22. The uniform fixed inlet values and

Table 8.22 Bartolomej Experiments - Boundary Conditions

Parameter	**Inlet**	**Outlet**	**Wall**
Temperature	∘	×	×
Velocity	×	∘	×
Pressure	∘	×	∘
Void Fraction	∘	×	×

∘ - Dirichlet Condition
× - Neumann Condition

initial conditions for void fraction, interfacial area concentration, bubble diameter, velocity, turbulent kinetic energy, and turbulent energy dissipation rate are found by using the given experimental data and a basic understanding of the problem. As explained previously, the constant value for the turbulent kinetic energy and the turbulent energy dissipation are calculated with approximate formulation for rounds pipes taken from [21]. The inlet value for the turbulent kinetic energy is given by the following formulation,

$$k_2 = \frac{3}{2}(\mathbf{U}_2 I)^2 \tag{8.18}$$

where the turbulence intensity is given by,

$$I = 0.16\mathrm{Re}_{D_h}^{-\frac{1}{8}} \tag{8.19}$$

where the Reynolds number for the hydraulic diameter (taken to be the pipe diameter in this case) is given by,

$$\mathrm{Re}_{D_h} = \frac{\rho_2 \mathbf{U}_2 D_h}{\mu_2} \tag{8.20}$$

The inlet value for turbulent energy dissipation is set by using the following formulation,

$$\epsilon_2 = C_\mu \frac{k_2^{\frac{3}{2}}}{L} \tag{8.21}$$

where the turbulent length scale for fully developed flow in a pipe is given by the following definition,

$$L = 0.038 D_h \tag{8.22}$$

For this experiment we have Star-CCM+ data so it is necessary to give the Star-CCM+ setup that was used to obtain that data. However, the Star-CCM+ setup does not very significantly to the one employed in our solver which is given in Table 8.23. Just to reiterate, the results obtained from Star-CCM+ were not done with the particular aim to get good agreement with the experimental data, but more in order to be able to replicate the results with our solver and also with the aim of employing a fairly stable method. As one can notice, there are essentially no interfacial forces, just the turbulence dispersion force to spread the void fraction away from the wall and the virtual mass force is there for stability reasons. Again, there are a few models in Star-CCM+ that we do not have coded into our solver but, for the most part we have matched the functionality with Star-CCM+ as close as we can without a look at the source code to check exact implementation, which is not a possibility. The turbulence disperision model employed in Star-CCM+ is not exactly the Burns [57] model, but, as previously stated, it is similar. For this set of results we kept the bubble diameter constant as well. This was done because of the differences in results seen from the adiabatic testcases when using the interfacial area concentration equation in comparison to Star-CCM+'s "S-Gamma" model. Again in an effort to keep the problem simple we chose to set the thermo-physical properties to a constant value with both phases being defined using the properties at saturation conditions.

The first set of results to be displayed in this section will be those results achieved given the previously mentioned setups and given in Fig. 8.28, Fig. 8.29 and Fig. 8.30. As can be seen in the above figures, our results for the axial distribution of cross-sectionally averaged void fraction in Fig. 8.30, the axial distribution of cross-sectionally averaged liquid subcooling in Fig. 8.29 and the axial distribution of wall superheat in Fig. 8.28 have a fairly good agreement with those results found from Star-CCM+.

Upon inspection, it is easy to see a slight over-prediction of void fraction and a slight undershoot of wall superheat in the figures, which is likely due to a unfortunate difference

Table 8.23 Bartolomej Experiments - BART07 Setup Summary

Closure Model	**Option**	**Details**
Mesh	$115 \times 20 \times 1$	$N_x \times N_y \times N_z$ [cells]
Equation of State	Constant	@ T_{sat}
Interfacial Models		
Diameter Model	Constant	$D_{b,1} = \langle D_{b,1} \rangle$
Drag Model	Ishii & Zuber	$\alpha_{max} = 0.74048$
Lift Model	–	$C_l = 0.0$
Wall Lubrication Model	–	$C_w = 0.0$
Turbulence Dispersion Model	Burns	$C_{td} = 1.0$
Virtual Mass Model	Constant	$C_{vm} = 0.5$
Turbulence Models		
Liquid Phase Turbulence	$k-\epsilon$ Equations	$C_\mu = 0.09$ and $\mathrm{Pr}_2^t = 0.9$
Vapor Phase Turbulence	Response Coefficient	$C_t = 1.0$
Bubble Induced Turbulence	Sato & Sekoguchi	$C_b = 0.0$
Phase Change Models		
Nucleation Site Density	Lemmert & Chawla	$m = 185.0$, $p = 1.805$
Wall Area Fraction	Limited	$\min\left(\frac{a\pi D_{b,w}^2}{4} N_a'', 1\right)$
Heat Transfer Coefficient Models		
Interfacial	Ranz & Marshall	–
Single-phase Convection	Wall Function	$y^+ = 250$
Two-phase Quenching	DeValle & Kenning	–
Bubble Models		
Departure Diameter	Tolubinksy & Kostanchuk	$\Delta T_{sub,0} = 45$ [°K]
		$D_{b,0} = 0.6$ [mm]
		$D_{b,\max} = 1.4$ [mm]
Departure Frequency	Cole	–
Wait Time Coefficient	$C_{tw} = 0.8$	$t_w = \frac{C_{tw}}{f_b}$
Area Influence Factor	$a = 4$	–

between the number of cells in the axial direction being modeled which affects the grid sensitive volumetric source terms in the conservation equations.

The difference in agreement for boiling cases can also be due to a myriad of other

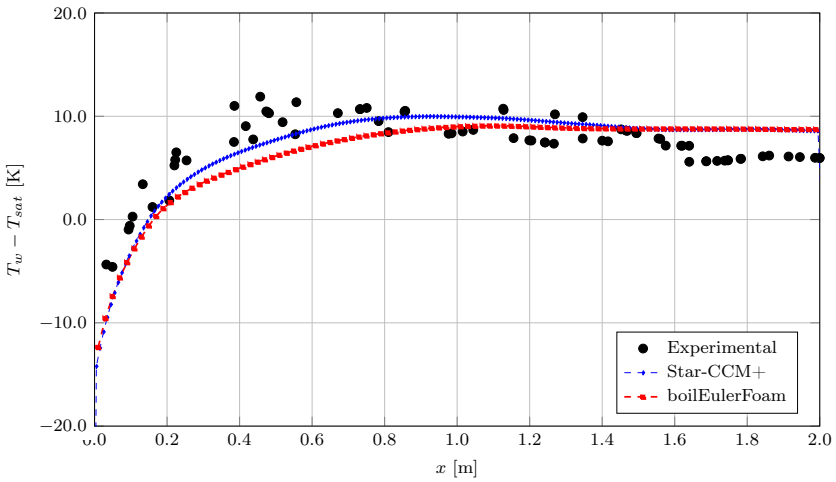

Figure 8.28 Bartolomej Experiments - BART07 Wall Superheat Comparison

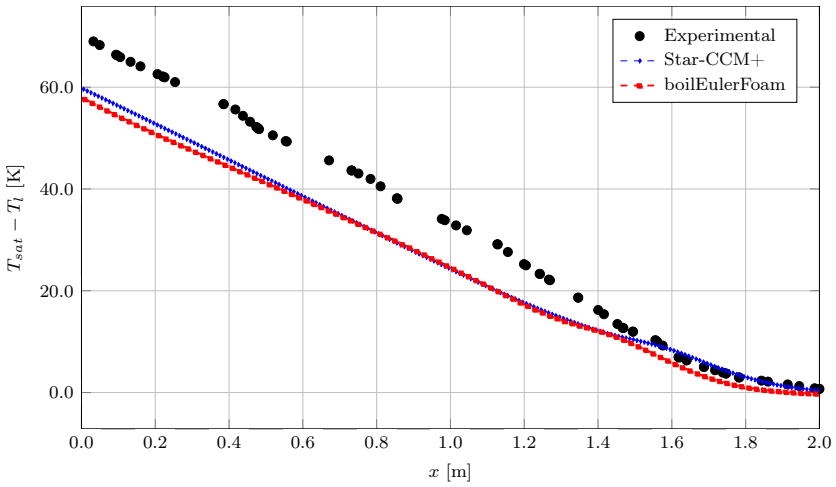

Figure 8.29 Bartolomej Experiments - BART07 Liquid Subcooling Comparison

reasons, for example, exact implementation differences of boiling closure models, interfacial closure models, and governing equations. The lack of detailed information on the exact implementation of the various closure models in Star-CCM+ and the large number of models makes it very difficult to figure out the sources of the differences between our results. A systematic approach being employed to test to see which combination yields the best agreement could potentially be very time consuming and also a not particularly helpful avenue of work, as there may prove to be various ways to achieve good agreement and a difficulty in assessing which is the correct way.

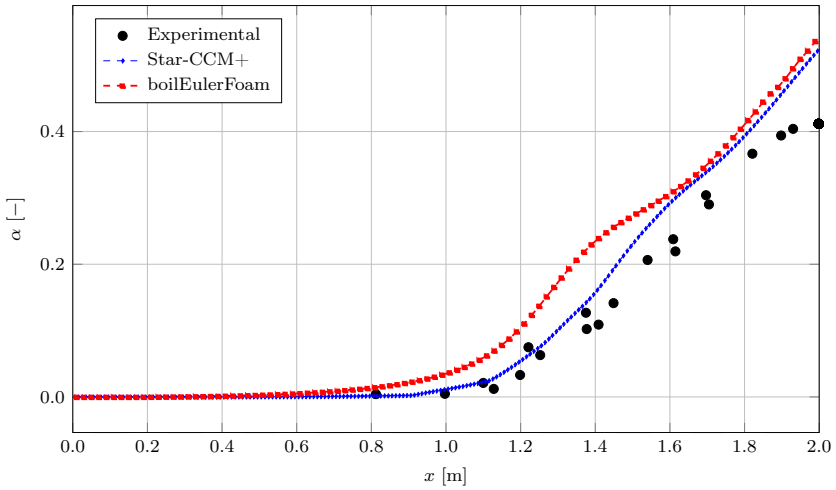

Figure 8.30 Bartolomej Experiments - BART07 Void Fraction Comparison

A preliminary grid refinement study was performed on the BART07 testcase with the previously discussed closure modeling and problem description. The refinement study employed four different radial refinements of 5, 10, 20 and 40 cells to see the effect. Fig. 8.31, Fig. 8.32 and Fig. 8.34 show the results achieved. As can be seen from an inspection of the

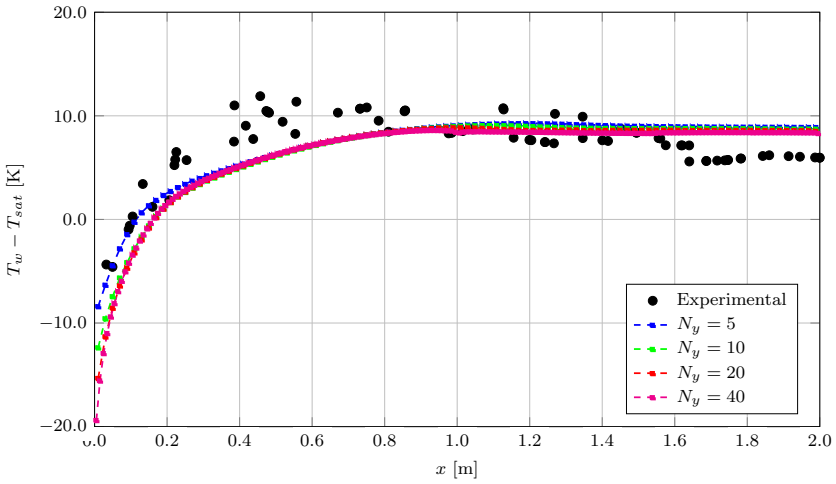

Figure 8.31 Bartolomej Experiments - BART07 Wall Superheat Grid Refinement Comparison

figures for the axial distribution of wall superheat in Fig. 8.31 through most of the channel

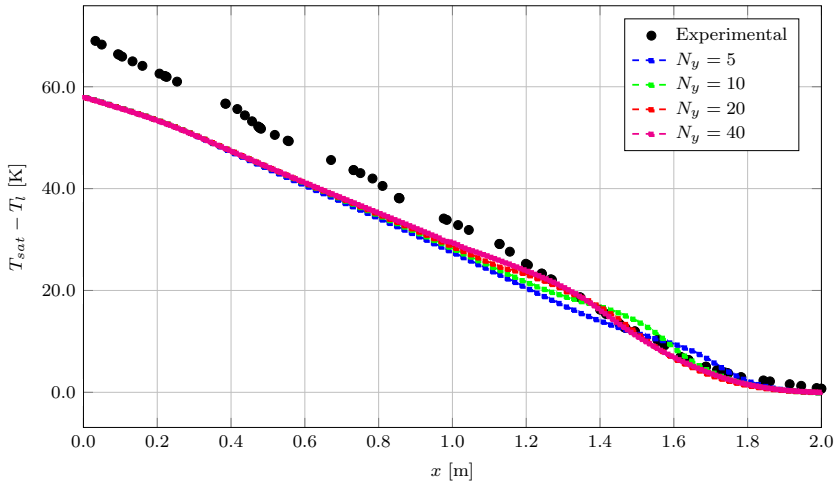

Figure 8.32 Bartolomej Experiments - BART07 Liquid Subcooling Grid Refinement Comparison

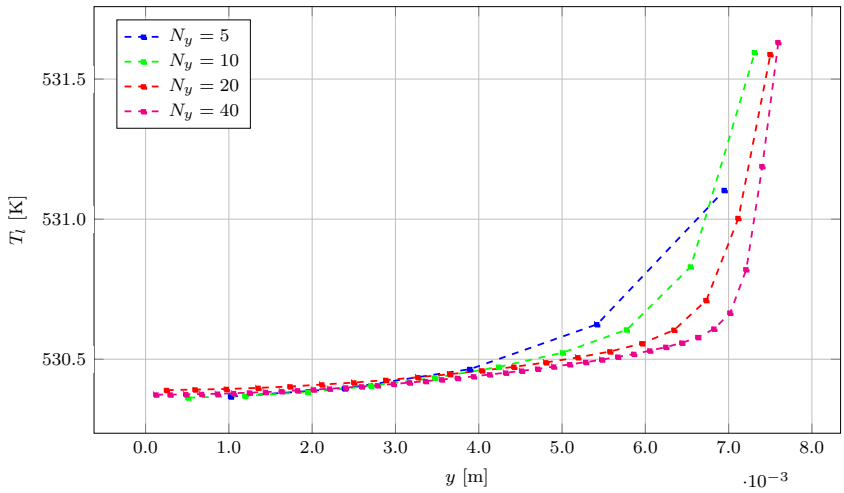

Figure 8.33 Bartolomej Experiments - BART07 Radial Liquid Subcooling Grid Refinement Comparison at Outlet

there is very little difference in the solution as a function of grid refinement. At the begining of the channel there is a decrease in superheat with a respective increase in grid refinement.

The axial distribution of the cross-sectionally averaged liquid subcooling in Fig. 8.32 in the beginning sections of the heated channel shows a similarity in the solutions regardless of grid refinement; however, further down the channel when boiling begins there exist significant differences in the cross-sectionally average liquid temperature distributions. This can be further displayed by Fig. 8.33.

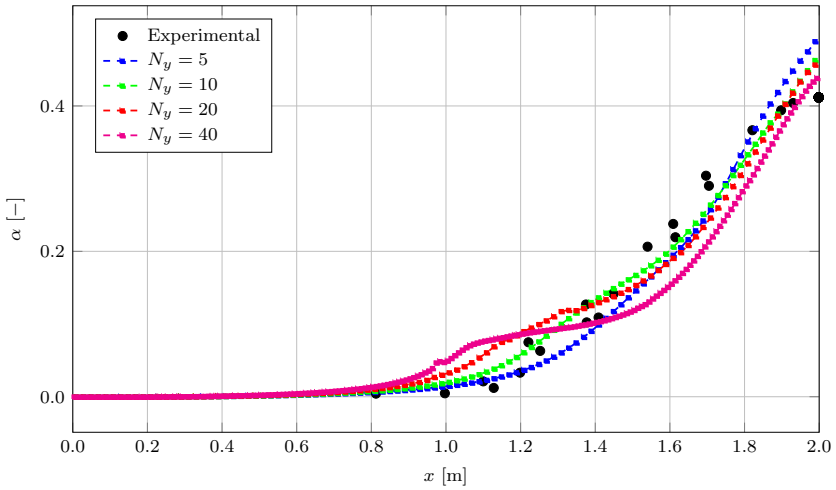

Figure 8.34 Bartolomej Experiments - BART07 Void Fraction Grid Refinement Comparison

It can be seen by inspecting the radial distributions of the liquid subcooling at the outlet of the heated section that the profiles vary significantly in both the shape as well as the amount of superheat. The axial distribution of the cross-sectionally average void fraction in Fig. 8.34 in the beginning sections of the heated channel shows a similarity in the solutions regardless of grid refinement. However, further down the channel when boiling begins and void actually begins to appear in the channel there exist significant differences. These differences present themselves in not only the axial distributions shape but, in the point along the channel when boiling begins. These differences could be occuring due to multiple reasons. One such reason could be due to the formulations employed to convert the various heat flux contributions to the phases found in the wall heat flux partitioning scheme, mentioned previously, to the volumetric source terms present in the governing equations being grid dependent. That is, if the grid refinement study was performed with a uniform increase in grid resolution, as opposed to just refining the radial component, perhaps the results would not vary as significantly.

Fig. 8.35 displays the radial void fraction distribution at the outlet of the heated section for the grid refinement. As can be seen from inspecting the figure the lowest refinement and the rest of the higher refinement resulting profiles vary fairly significantly; however, between the three highest refinements there is not a significant difference. It is currently unclear as to what the reasons for the differences in the distributions for the grid refinement, further investigation is needed in order to accurately assess the causes.

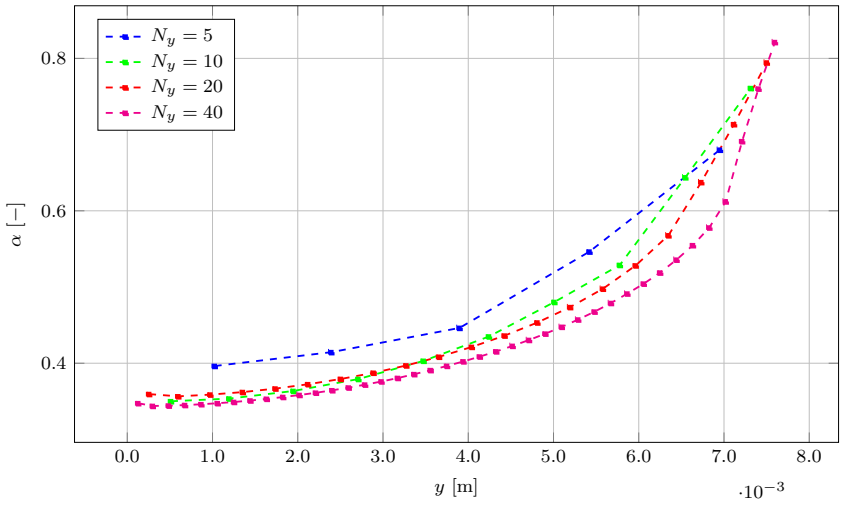

Figure 8.35 Bartolomej Experiments - BART07 Radial Void Fraction Grid Refinement Comparison at Outlet

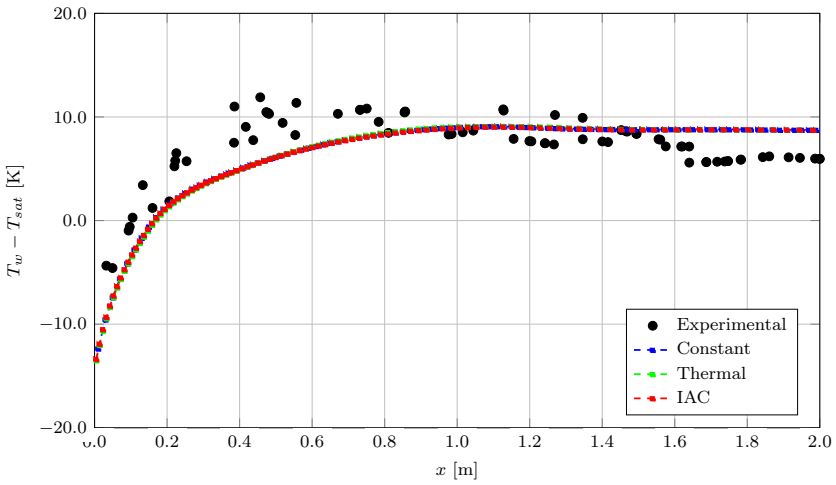

Figure 8.36 Bartolomej Experiments - BART07 Interfacial Bubble Diameter Closure Wall Superheat Comparison

Lastly, for the BART07 experimental conditions and using the previously discussed setup, a preliminary examination of the effects of the closure modeling of the interfacial bulk bubble diameter has on the solution was performed. Three methods were employed in this examination. The first being the setting of the interfacial bulk bubble diamter to a constant value of 1 mm which is the reference setup given previously in this section.

The second method employed is through the use of the thermal model for the interfacial

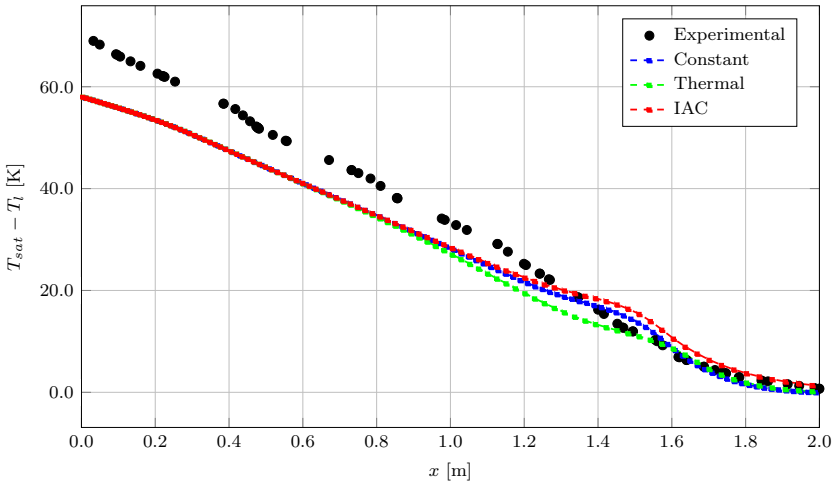

Figure 8.37 Bartolomej Experiments - BART07 Interfacial Bubble Diameter Closure Liquid Subcooling Comparison

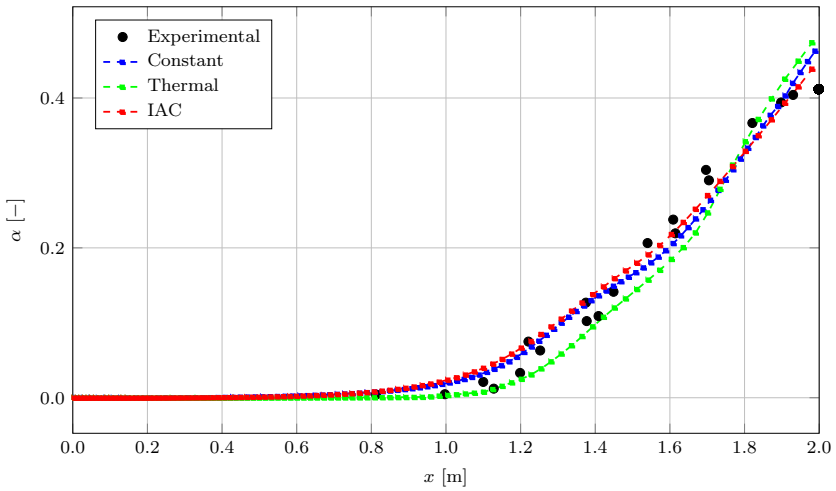

Figure 8.38 Bartolomej Experiments - BART07 Interfacial Bubble Diameter Closure Void Fraction Comparison

bulk bubble diameter. The model is employed with the coefficients of $D_{b,0} = 0.01$ mm, $D_{b,1} = 2.0$ mm, $T_{sub,0} = 13.5\,^{\circ}$K and $T_{sub,1} = -5.0\,^{\circ}$K. The third and final method employed is the use of the interfacial area concentration (IAC) equation to estimate the interfacial bulk bubble diameter distribution. The break-up and coalescence terms were modeled using Yao & Morel models.

The set of results achieved with this comparison are displayed in Fig. 8.36, Fig. 8.37 and Fig. 8.38. As can be seen in the figures, our results for the axial distribution of cross-

sectionally averaged void fraction in Fig. 8.38, the axial distribution of cross-sectionally averaged liquid subcooling in Fig. 8.37 and the axial distribution of wall superheat in Fig. 8.36 have a fairly good agreement between methods for interfacial bulk bubble diameter closure modeling. Especially, those found for the axial distribution of the wall superheat in Fig. 8.36. There is very little deviation between the results. The deviations that do occur are likely due to both the affect that the different bubble diameters have on the interfacial force distribution (although the effect is rather mild because of the simplistic interfacial closure modeling for this testcase) and the affect the different interfacial bubble diameters (and consequently the interfacial area) have on the interfacial heat transfer terms.

The last analysis for this testcase using the BART07 set of experimental conditions was an efficieny study. This study was performed in order to assess the difference in computational time it took to get steady state solution, using the reference setup given previously in this section, between Star-CCM+ and our solver. The results were both achieved on the same computer run in serial and are given in Table 8.24. As can be seen from the table, our solver

Table 8.24 Bartolomej Experiments - Efficiency Study

Solver	**Time** [**min**]
Star-CCM+	8.0
boilEulerFOAM (OpenFOAM)	13.0

(boilEulerFOAM) is not as efficient as the Star-CCM+; however, this could potentially be changed with some coding changes because our solver is current designed to be more functional than efficient.

8.8 DEBORA Experiments

This numerical testcase is from a set of experiments commonly referred to as the DEBORA Experiments. These numerical testcases consist of a steady state simulation of subcooled boiling pipe flow with a constant wall heat flux at high pressures with R12 refrigerant being the fluid. These experiments are sub-cooled boiling flow experiments with relatively high

void fraction production. The experimental conditions are fairly close to those that would be modeled in PWR CFD simulations and thus an accurate modeling of these results is oen of the end-goals of this project. The pipe that the experiment takes place in is vertical and the flow is from bottom towards the tops so that gravity and bouyancy effects play an important role. The three-dimensional pipe geometry (displayed in Table 8.39) was converted to a quasi-two-dimensional geometry by using axis-symmetry and modeling a wedge of the pipe in order to reduce the size of this computational problem.

Table 8.25 gives a more detailed description of the experimental geometry and a general idea of the meshing used for this scientific testcase. Again, these types of flow problems

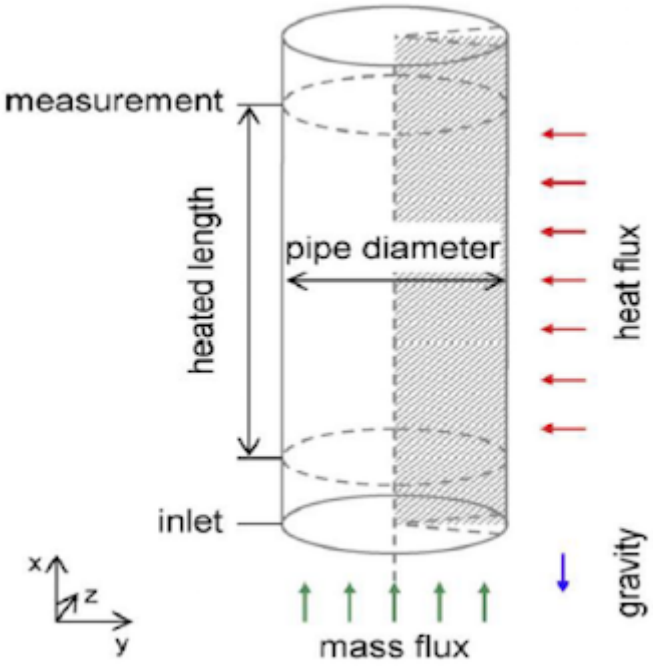

Figure 8.39 DEBORA Experiments - Test Section Geometry (Krepper and Rzehak, 2011) [33]

give a method to test the functionality of all of the closure models, and especially, the phase change closure modeling methods. The pipe diameter for these experiments is similar slightly larger than that of the Bartolomej Experiments but still on the order of a PWR fuel bundle hydraulic diameter. The use of this experiment is that it helps to test the functionality of the phase change closure models for a different fluid. This is interesting; however, it also

Table 8.25 DEBORA Experiments - Brief Experimental Setup

Property	**Value**
Pipe Diameter	19.2 [mm]
Pipe Length	3.5 [m]
Axial Direction # of Cells	$100-350$ cells
Radial Direction # of Cells	$10-70$ cells

can be problematic as all the closure models for phase change were originally designed for one dimensional volume averaged correlations and typically based on experiments for water. Thus, their applicability is questionable.

There are several sets of experimental conditions in the literature, and a description of the different experimental conditions found in [33] can be seen in Table 8.26. For these

Table 8.26 DEBORA Experiments - Selected Experiments

Test	p [**MPa**]	$G\left[\frac{\mathbf{kg}}{\mathbf{m^2 \cdot s}}\right]$	$q''_{wall}\left[\frac{\mathbf{kW}}{\mathbf{m^2}}\right]$	T_{in} [°**K**]	T_{sat} [°**K**]
DEB01	2.62	1986	73.89	341.67	359.79
DEB02	2.62	1985	73.89	343.68	359.79
DEB03	2.62	2981	109.42	342.35	359.79
DEB04	1.46	2028	76.19	308.75	331.3
DEB05	1.46	2023	76.26	312.82	331.3

experiments we currently only have access to radial profile data at the outlet of the heated section for void fraction, α_1, liquid temperature, T_2, and the vapor phase bubble diameter, D_b, which makes it difficult to assess the correct closure modeling implementation for phase change closure models. This is because we only have values for the "end result" and there may be many setups to achieve this result, but due to the complexity of the problem figuring out the "correct" method remains very challenging. From the 5 sets of experimental conditions for which we have experimental data only one setup was studied in-depth (e.g.

DEB01) and will be displayed in this section.

Table 8.27 gives the thermo-physical properties needed in order to simulate the DEB01 case, which again is the only case that was examined in detail for this set of experiments. All the values in the table and through-out this work, unless otherwise specified by the

Table 8.27 DEBORA Experiments - Thermo-physical Properties

Parameter	**Variable**	**Saturation**	**Inlet**
Pressure	p [MPa]	2.62	2.62
Temperature	T [°K]	359.98	341.67
Vapor Properties			
Density	$\rho_1 \left[\frac{\text{kg}}{\text{m}^3}\right]$	172.51	–
Dynamic Viscosity	$\mu_1 \left[\frac{\text{kg}}{\text{m·s}}\right]$	1.6390×10^{-5}	–
Specific Heat	$C_{p,1} \left[\frac{\text{J}}{\text{kg·K}}\right]$	1294.0	–
Prandlt Number	Pr_1 [–]	1.19364	–
Enthalpy	$h_1 \left[\frac{\text{J}}{\text{kg}}\right]$	3.7859×10^5	–
Liquid Properties			
Density	$\rho_2 \left[\frac{\text{kg}}{\text{m}^3}\right]$	1016.4	1138.8
Dynamic Viscosity	$\mu_2 \left[\frac{\text{kg}}{\text{m·s}}\right]$	8.9402×10^{-5}	1.1974×10^{-4}
Specific Heat	$C_{p,2} \left[\frac{\text{J}}{\text{kg·K}}\right]$	1422.0	1146.9
Prandlt Number	Pr_2 [–]	2.78360	2.57940
Enthalpy	$h_2 \left[\frac{\text{J}}{\text{kg}}\right]$	2.9267×10^5	2.6974×10^5
Interphase Properties			
Surface Tension	$\sigma \left[\frac{\text{N}}{\text{m}}\right]$	0.0017657	–
Latent Heat	$h_{21} \left[\frac{\text{J}}{\text{kg}}\right]$	8.5920×10^4	–

description of the experiment, were found on NIST website. It is important to note that when using constant properties for an equation of state the liquid properties can be taken at the saturation condition, at the inlet temperature or an average of the two; however, the velocity must be calculated with the density to ensure the correct mass flux. The heat of

formation must be calculated in order to ensure that,

$$h_{sat,k} = C_{p,k} T_{sat} + H_{f,k} \tag{8.23}$$

For the purposes of these experiments we run the solver with constant properties; however, as explained previously, the density of the vapor phase can be a variable quantity and can be calculated using a constant compressibility constant, ideal gas law, stiffened ideal gas law, and various other methods. The low speed flow of these experiments means that compressibility effects of the liquid phase do not need to be taken into account; however, changes in temperature will still affect the density but, this is often neglected due to computational effort and the extreme difficulty to reach stable solutions because of the high non-linearity of the problem. The boundary conditions for the experiments we have chosen are given in Table 8.28. The uniform fixed inlet values and initial conditions for

Table 8.28 DEBORA Experiments - Boundary Conditions

Parameter	**Inlet**	**Outlet**	**Wall**
Temperature	∘	×	×
Velocity	×	∘	×
Pressure	∘	×	∘
Void Fraction	∘	×	×

∘ - Dirichlet Condition

× - Neumann Condition

void fraction, interfacial area concentration, bubble diameter, velocity, turbulent kinetic energy, and turbulent energy dissipation rate are found by using the given experimental data and a basic understanding of the problem. As explained previously, the constant value for the turbulent kinetic energy and the turbulent energy dissipation are calculated with approximate formulation for rounds pipes taken from [21]. The inlet value for the turbulent kinetic energy is given by the following formulation,

$$k_2 = \frac{3}{2}(\mathbf{U}_2 I)^2 \tag{8.24}$$

where the turbulence intensity is given by,

$$I = 0.16\mathrm{Re}_{D_h}^{-\frac{1}{8}} \tag{8.25}$$

where the Reynolds number for the hydraulic diameter (taken to be the pipe diameter in this case) is given by,

$$\mathrm{Re}_{D_h} = \frac{\rho_2 \mathbf{U}_2 D_h}{\mu_2} \tag{8.26}$$

The inlet value for turbulent energy dissipation is set by using the following formulation,

$$\epsilon_2 = C_\mu \frac{k_2^{\frac{3}{2}}}{L} \tag{8.27}$$

where the turbulent length scale for fully developed flow in a pipe is given by the following definition,

$$L = 0.038 D_h \tag{8.28}$$

For this experiment we have Star-CCM+ data so it is necessary to give the Star-CCM+ setup that was used to obtain that data. However, the Star-CCM+ setup does not very significantly to the one employed in our solver which is given in Table 8.29. Just to reiterate, the results obtained from Star-CCM+ were not done with the particular aim to get good agreement with the experimental data, but more in order to be able to replicate the results with our solver and also with the aim of employing a fairly stable method. Again, there are a few models in Star-CCM+ that we do not have coded into our solver but, for the most part we have matched the functionality with Star-CCM+ as close as we can without a look at the source code to check exact implementation, which is not a possibility. For this set of results we used the thermal bubble diameter because we could extrapolate approximate values from the experimental data to reproduce the bubble diameter. This was also done because of the differences in results seen from the adiabatic testcases when using the interfacial area concentration equation in comparison to Star-CCM+'s "S-Gamma" model. Again in an effort to keep the problem simple we chose to set the thermo-physical properties to a constant value with vapor phase being defined using the properties at saturation conditions and the liquid phase being defined using the properties at the average temperature between the inlet and saturation conditions.

The results to be displayed in this section will be those results achieved given the

Table 8.29 DEBORA Experiments - BART07 Setup Summary

Closure Model	**Option**	**Details**
Mesh	$115 \times 20 \times 1$	$N_x \times N_y \times N_z$ [cells]
Equation of State	Constant	@ T_{ave}
Interfacial Models		
Diameter Model	Thermal	$D_{b,0} = 0.01$ mm, $D_{b,1} = 2.0$ mm, $T_{sub,0} = 13.5\,^{\circ}$K and $T_{sub,1} = -5.0\,^{\circ}$K
Drag Model	Schiller & Naumann	$\alpha_{max} = 0.74048$
Lift Model	–	$C_l = 0.0$
Wall Lubrication Model	Antal	$C_{w1} = -0.01$ and $C_{w2} = 0.05$
Turbulence Dispersion Model	Burns	$C_{td} = 1.0$
Virtual Mass Model	Constant	$C_{vm} = 0.5$
Turbulence Models		
Liquid Phase Turbulence	$k-\epsilon$ Equations	$C_\mu = 0.09$ and $\mathrm{Pr}_2^t = 0.9$
Vapor Phase Turbulence	Response Coefficient	$C_t = 1.0$
Bubble Induced Turbulence	Sato & Sekoguchi	$C_b = 0.0$
Phase Change Models		
Nucleation Site Density	Lemmert & Chawla	$m = 185.0$, $p = 1.805$
Wall Area Fraction	Limited	$\min\left(\frac{a\pi D_{b,w}^2}{4} N_a'', 1\right)$
Heat Transfer Coefficient Models		
Interfacial	Ranz & Marshall	–
Single-phase Convection	Wall Function	$y^+ = 250$
Two-phase Quenching	DeValle & Kenning	–
Bubble Models		
Departure Diameter	Tolubinksy & Kostanchuk	$\Delta T_{sub,0} = 45$ [°K] $D_{b,0} = 0.6$ [mm] $D_{b,\max} = 1.4$ [mm]
Departure Frequency	Cole	–
Wait Time Coefficient	$C_{tw} = 0.8$	$t_w = \frac{C_{tw}}{f_b}$
Area Influence Factor	$a = 4$	–

previously mentioned setups and given in Fig. 8.40, Fig. 8.41 and Fig. 8.42. As can be seen from the figures, there is a large discrepancy between the results achieved with our solver

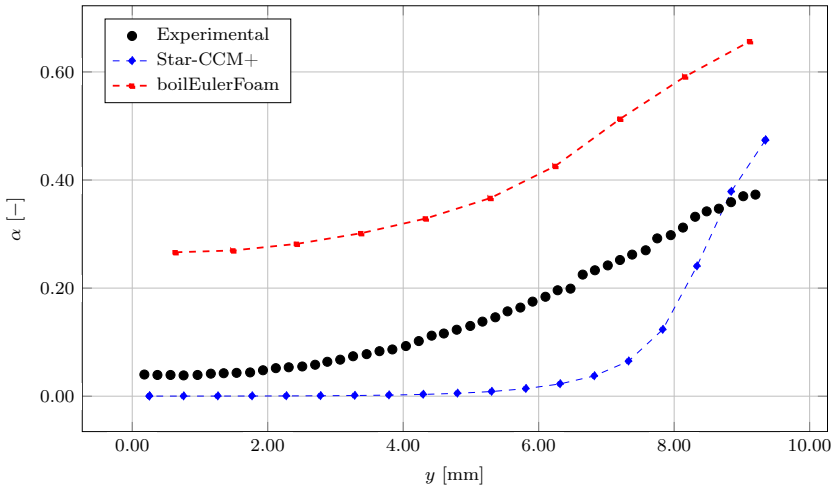

Figure 8.40 DEBORA Experiments - DEB01 Void Fraction Comparison

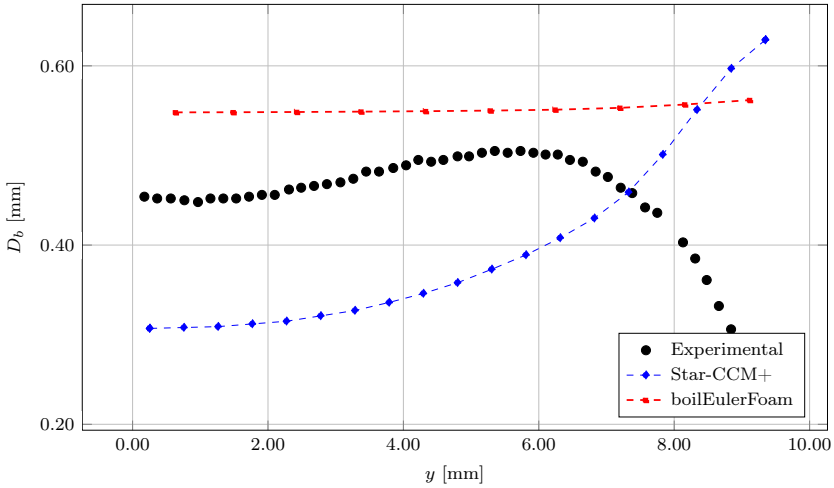

Figure 8.41 DEBORA Experiments - DEB01 Bubble Diameter Comparison

and those found with Star-CCM+. This discrepancy could be due to a number of reasons and it is currently unclear as to the source. One potential source is that there is a difference in the energy equation formulation between our solver and Star-CCM+. According to the documentation, Star-CCM+ does not account for the kinetic energy. Also, the viscous heating term is split between the molecular & turbulent components with the molecular component being estimated with temperature instead of enthalpy. There may also be a difference in the application of the mass transfer terms & wall temperatures. Currently our solver employs volumetric heat & mass transfer source terms; however, Star-CCM+ may

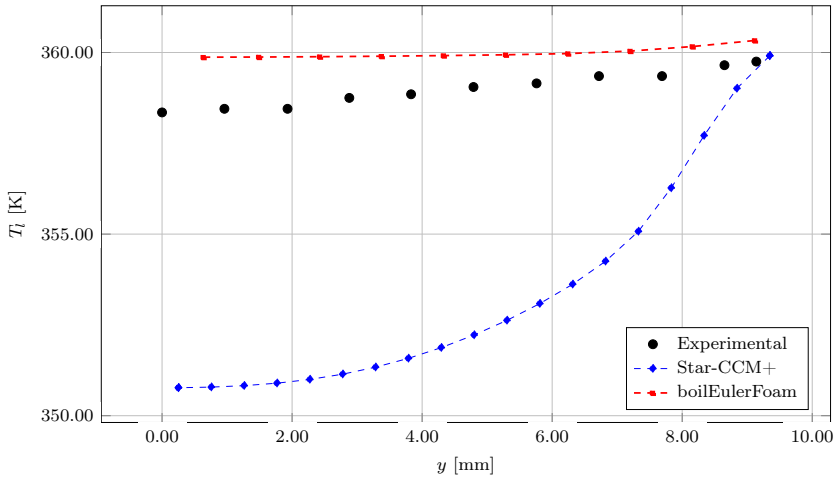

Figure 8.42 DEBORA Experiments - DEB01 Liquid Temperature Comparison

employ boundary conditions as the volumetric source terms can lead to grid dependent solutions. The Star-CCM+ results also seem to employ a grading in the direction normal to the wall that reduces the effectiveness of the wall lubrication model. Lastly, there may also be some differences in the thermo-physical modeling approach between our solver and Star-CCM+ that could cause some of the differences displayed.

8.9 MIT Boiling Test Facility Experiments

This test case is an avenue for both collaboration with another, very prominent and top-notch, university (e.g. namely Massachusetts Institute of Technology) as well as a chance to test our solver on more recent scientific experiments in the area of multiphase flows. This test case will allow more fine tuning for our models and methods in the future because of the abundance of experimental data available, as well as, validation of the capabilities of our solver. One of the main aims of this collaborative effort with students at MIT is to co-develop and validate some new boiling correlations that they are developing and testing using the user-defined functionality of Star-CCM+. Of course, the benefit of our solver is it being an open source program so this gives us the freedom to change anything in our code to suit our purposes. On top of some boiling correlation implementation with the people at MIT, this test case will also possibly allow us to work with them on some turbulence modeling improvements and interfacial momentum force modeling improvements that

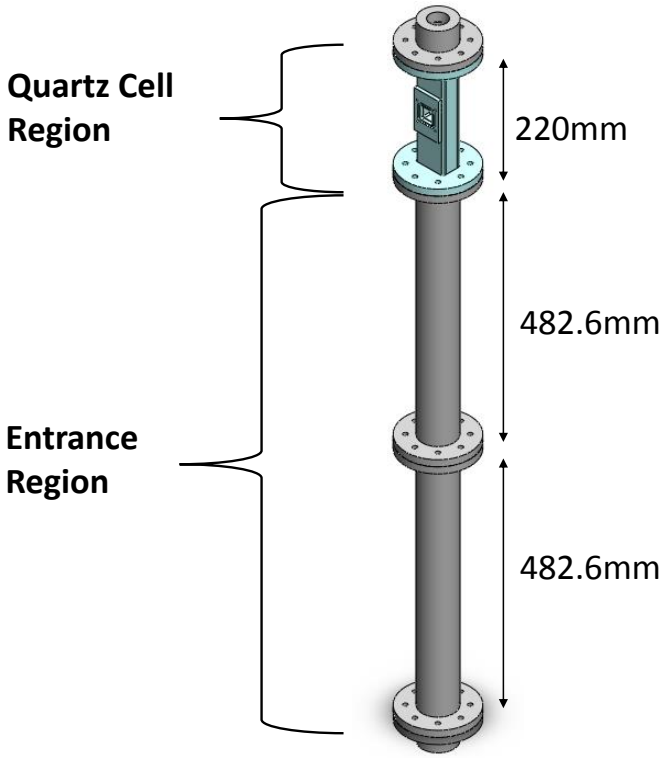

Figure 8.43 MIT Experiments - Experimental Geometry [24]

are also currently being developed by their group.

This section will cover the discussion of general experimental setup, operating conditions, geometry descriptions, available experimental data used for comparison, and range of operational capabilities for MIT's flow boiling facility [24]. The general description of MIT's flow boiling test facility and all of the run specific descriptions that were employed in the numerical modeling of the experiment with our solver are also discussed in this section. The flow boiling facility at MIT uses non-intrusive techniques (e.g. high speed video and infrared thermography) to capture new and unique subcooled flow boiling data on multiple parameters simultaneously. The quantities measure at the facility are given in Table 8.30. The basic experimental setup is displayed in Fig. 8.43 and Fig. 8.44. It consists of an entrance region of two channel sections; each with an internal rectangular flow area of 30 mm × 10 mm (e.g. 300 mm^2) and 482.6 mm in length. This results in a total entrance region prior to a quartz (e.g. the section where the heat transfer occurs) of 965.2 mm. The quartz region has a total length of 220 mm and maintans the same rectangular geometry

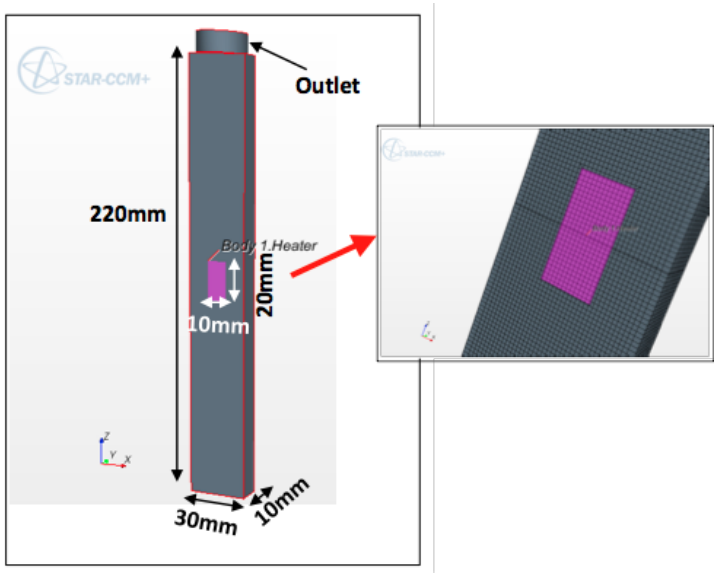

Figure 8.44 MIT Experiments - Heated Quartz Section Geometry [24]

Table 8.30 MIT Experiments - Available Experimental Data

Parameter	Variable
Bubble Departure Diameter	$D_{b,w}$
Wall Superheat (local)	T_{sup} or T_{wall}
Wall Superheat (surface-averaged)	$\langle T_{sup} \rangle$ or $\langle T_{wall} \rangle$
Heat Transfer Coefficients	$h^{(f)}_{c,1\phi}$, $h^{(f)}_{c,2\phi}$, $h_{c,fg}$
Active Nucleation Site Density	N''_a
Bubble Growth Time	t_g
Bubble Wait Time	t_w

and flow area as the entrance region. The heated area is centered in the quartz region and has dimensions of 10 mm × 20 mm. The heater has a thickness of 0.7 mm and is a resistively heated layer of Indium-Tin-Oxide (ITO) using graphite electrodes deposited over a sapphire substrate (1 mm thick). The heater is flush with the quartz so as to not provide any obstruction of flow. Table 8.31 gives a breakdown of some of the basic experimental dimensions for these testcases. Table 8.32 all of the potential experimental condition ranges for each value that is able to be modified in the MIT flow boiling facility. Only a single case was studied in detail out of the experimental conditions; however, the experimental setups

Table 8.31 MIT Experiments - Test Facility Dimensions and Properties

Parameter	**Value**
Channel Length (x-direction, total)	1,185.2 [mm]
Channel Length (x-direction, entrance)	965.2 [mm]
Channel Length (x-direction, quartz)	220 [mm]
Channel Height (y-direction)	10 [mm]
Channel Width (z-direction)	30 [mm]
Heater Size (Δx, Δy, Δz)	(20, 0, 10) [mm]

Table 8.32 MIT Experiments - Potential Operating Conditions

Parameter	**Range**
Inlet Water Velocity	$0-2\left[\frac{\mathrm{m}}{\mathrm{s}}\right]$
Mass Flux	$0-1800\left[\frac{\mathrm{kg}}{\mathrm{m}^2\cdot\mathrm{s}}\right]$
Temperature	$25-250$ [°C]
Pressure	$0.1-0.4$ [MPa]
Subcooling	$0-75$ [°C]
Heat Flux	$0-2\left[\frac{\mathrm{MW}}{\mathrm{m}^2}\right]$

that we recieved Star-CCM+ data for, could all be used for validation of our solver. For this experiment, the cases described in Table 8.33 were used (or could be used in the future) as a basis of comparison between our solver in the OpenFOAM framework and the commerical package Star-CCM+. Table 8.34 gives a breakdown of the steam & water thermodynamic and transport properties at the given pressure for both saturation and inlet temperature (inlet temperatures only for the water properties in order to average between the two states, if necessary). All the values in the table and through-out this work unless specified by the description of the experiment were found on NIST website. It is important to note that the liquid properties can be taken at the saturation condition, at the inlet temperature or an average of the two; however, the velocity must be calculated with the density to ensure the correct mass flux. The heat of formation must be calculated in order to ensure that,

$$h_{sat,k} = C_{p,k} T_{sat} + H_{f,k} \tag{8.29}$$

Table 8.33 MIT Experiments - Summary of Experiments

Parameter	**MIT01**	**MIT02**	**MIT03**	**MIT04**	**MIT05**	**MIT06**
Pressure, [MPa]	0.105	0.105	0.150	0.150	0.20	0.20
Mass Flux, $\left[\frac{\text{kg}}{\text{m}^2\cdot\text{s}}\right]$	500	1000	500	1000	500	1000
Subcooling, [°C]	10	10	10	10	10	10
Heat Flux, $\left[\frac{\text{MW}}{\text{m}^2}\right]$	1.4	1.4	1.4	1.4	1.4	1.4

Table 8.34 MIT Experiments - MIT03 Thermo-physical Properties

Parameter	**Variable**	**Saturation**	**Inlet**
Pressure	p [MPa]	0.150	0.150
Temperature	T [°K]	384.5	374.5
Vapor Properties			
Density	$\rho_1 \left[\frac{\text{kg}}{\text{m}^3}\right]$	0.86260	—
Dynamic Viscosity	$\mu_1 \left[\frac{\text{kg}}{\text{m}\cdot\text{s}}\right]$	1.2658×10^{-5}	—
Specific Heat	$C_{p,1} \left[\frac{\text{J}}{\text{kg}\cdot\text{K}}\right]$	2131.0	—
Thermal Conductivity	$\kappa_1 \left[\frac{\text{W}}{\text{m}\cdot\text{K}}\right]$	0.026405	—
Enthalpy	$h_1 \left[\frac{\text{J}}{\text{kg}}\right]$	2.7979×10^6	—
Liquid Properties			
Density	$\rho_2 \left[\frac{\text{kg}}{\text{m}^3}\right]$	949.92	957.4
Dynamic Viscosity	$\mu_2 \left[\frac{\text{kg}}{\text{m}\cdot\text{s}}\right]$	2.5141×10^{-4}	2.7781×10^{-4}
Specific Heat	$C_{p,2} \left[\frac{\text{J}}{\text{kg}\cdot\text{K}}\right]$	4230.2	4217.1
Thermal Conductivity	$\kappa_2 \left[\frac{\text{W}}{\text{m}\cdot\text{K}}\right]$	0.68195	0.67954
Enthalpy	$h_2 \left[\frac{\text{J}}{\text{kg}}\right]$	4.6713×10^5	4.2489×10^5
Interphase Properties			
Surface Tension	$\sigma \left[\frac{\text{N}}{\text{m}}\right]$	0.056695	—
Latent Heat	$h_{21} \left[\frac{\text{J}}{\text{kg}}\right]$	2.22597×10^6	—

For the purposes of these experiments we run the solver with constant properties; however, as explained previously, the density of the vapor phase can be a variable quantity and can be calculated using a constant compressibility constant, ideal gas law, stiffened ideal gas

law, and various other methods. The low speed flow of these experiments means that compressibility effects of the liquid phase (e.g. the water) do not need to be taken into account; however, changes in temperature will still affect the density but, this is often neglected due to computational effort and the extreme difficulty to reach stable solutions because of the high non-linearity of the problem. The boundary conditions for the experiments we have chosen are given in Table 8.35. The uniform fixed inlet values and initial conditions for

Table 8.35 MIT Experiments - Boundary Conditions

Parameter	**Inlet**	**Outlet**	**Wall**
Temperature	∘	×	×
Velocity	×	∘	×
Pressure	∘	×	∘
Void Fraction	∘	×	×

∘ - Dirichlet Condition

× - Neumann Condition

void fraction, interfacial area concentration, bubble diameter, velocity, turbulent kinetic energy, and turbulent energy dissipation rate are found by using the given experimental data, running the problem in the first two unheated sections of the experimental geometry in order to get the fully-developed profile at the inlet of the quartz section of the geometry where the heater is located. This was done in order to reduce the computational effort involved in simulating this case. As explained previously, the constant value for the turbulent kinetic energy and the turbulent energy dissipation are calculated with approximate formulation for rounds pipes taken from [21], with the only change being in the calculation of the hydraulic diameter, D_h, as it is no longer equivalent to the pipe diameter. The inlet value for the turbulent kinetic energy is given by the following formulation,

$$k_2 = \frac{3}{2}(\mathbf{U}_2 I)^2 \tag{8.30}$$

where the turbulence intensity is given by,

$$I = 0.16\mathrm{Re}_{D_h}^{-\frac{1}{8}} \tag{8.31}$$

where the Reynolds number for the hydraulic diameter (taken to be the pipe diameter in this case) is given by,

$$\mathrm{Re}_{D_h} = \frac{\rho_2 \mathbf{U}_2 D_h}{\mu_2} \tag{8.32}$$

The inlet value for turbulent energy dissipation is set by using the following formulation,

$$\epsilon_2 = C_\mu \frac{k_2^{\frac{3}{2}}}{L} \tag{8.33}$$

where the turbulent length scale for fully developed flow in a pipe is given by the following definition,

$$L = 0.038 D_h \tag{8.34}$$

Table 8.36 will give a breakdown of the reference setup employed for our solver and this setup is fairly close to the original RPI boiling model, with the use of a few improved models and employment of wall functions in order to estimate bulk values (e.g. to account for some of the correlations use of bulk temperatures and velocities) and, as previously stated, will be considered the reference setup for this set of experimental conditions on the MIT Boiling Test Facility apparatus. For this experiment we have Star-CCM+ data so it is necessary to give the Star-CCM+ setup that was used to obtain that data. However, the Star-CCM+ setup does not very significantly to the one employed in our solver which is given in Table 8.36. The StarCCM+ set is basically identical to the reference setup for this test case excepting those models discussed in previous section that are different (i.e. the turbulence dispersion interfacial force model). As mentioned previously, the first run was done in order to model the whole geometry. Then the inlet profiles were taken at the inlet to the heated quartz section which will allow a much reduced domain to allow the quicker computation and analysis of results. The results for this set of experimental conditions in comparison to those achieved by Star-CCM+ can be seen in Fig. 8.45, Fig. 8.46, Fig. 8.47, Fig. 8.48 and Fig. 8.49. Fig. 8.45 shows a very close correlation of the area averaged wall superheat at the heated section of wall over the various power levels between the results from the two solvers and the experimental results. Now for the rest of the experimental data is currently

Table 8.36 MIT Experiments - MIT03 Setup Summary

Closure Model	**Option**	**Details**
Mesh	$110 \times 10 \times 30$	$N_x \times N_y \times N_z$ [cells]
Equation of State	Constant	@ T_{sat}
Interfacial Models		
Diameter Model	Constant	$D_{b,1} = 1.0$
Drag Model	Tomiyama	$\alpha_{max} = 0.74048$
Lift Model	Constant	$C_l = 0.025$
Wall Lubrication Model	Antal	$C_{w1} = -0.01$, $C_{w2} = 0.05$
Turbulence Dispersion Model	Burns	$C_{td} = 1.0$
Virtual Mass Model	Constant	$C_{vm} = 0.5$
Turbulence Models		
Liquid Phase Turbulence	$k-\epsilon$ Equations	$C_\mu = 0.09$ and $\mathrm{Pr}_2^t = 0.9$
Vapor Phase Turbulence	Response Coefficient	$C_t = 1.0$
Bubble Induced Turbulence	Sato & Sekoguchi	$C_b = 1.2$
Phase Change Models		
Nucleation Site Density	Hibiki & Ishii	$m = 185.0$, $p = 1.805$
Wall Area Fraction	Limited	$\min\left(\frac{a\pi D_{b,w}^2}{4} N_a'', 1\right)$
Heat Transfer Coefficient Models		
Interfacial	Chen & Mayiner	–
Single-phase Convection	Wall Function	$y^+ = 250$
Two-phase Quenching	DeValle & Kenning	–
Bubble Models		
Departure Diameter	Tolubinksy & Kostanchuk	$\Delta T_{sub,0} = 45$ [°K] $D_b\,(0, \max) = (0.6, 1.4)$ [mm]
Departure Frequency	Cole	–
Wait Time Coefficient	$C_{tw} = 0.8$	$t_w = \frac{C_{tw}}{f_b}$
Area Influence Factor	$a = 4$	–

missing as the experiments have yet to be finished. The result of the figures contain soley a between Star-CCM+ and our solver. Fig. 8.46 shows a significant deviation for the area averaged void production at the heated wall over the power levels. It starts extremely close; however, the deviation occurs very early on in the power ramping of the solution. There is

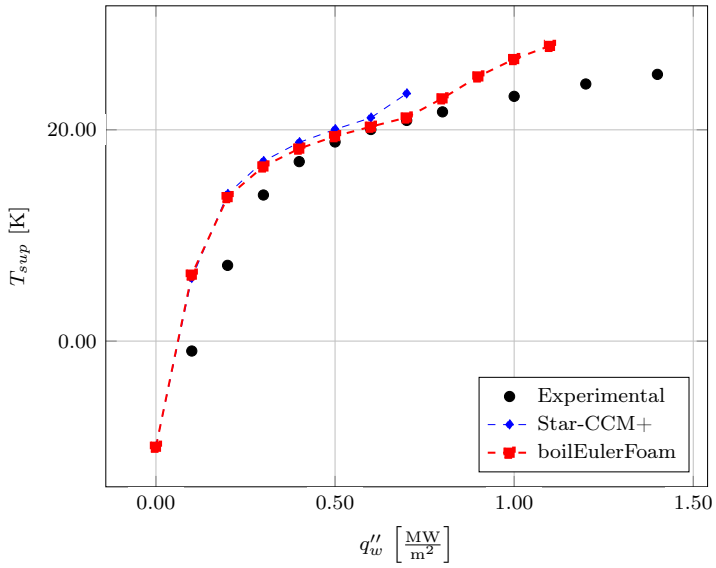

Figure 8.45 MIT Experiments - MIT03 Area Averaged Wall Superheat vs Power at Heated Section

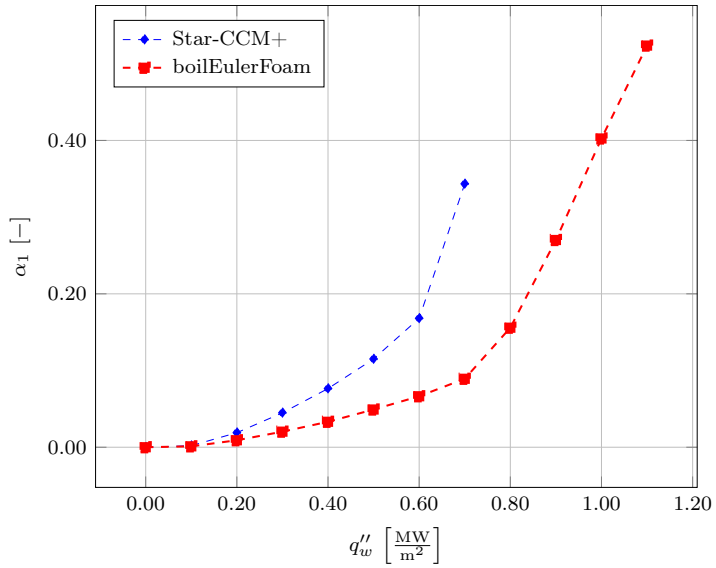

Figure 8.46 MIT Experiments - MIT03 Area Averaged Void Fraction vs Power at Heated Section

also a deviation in the area averaged nucleation site density at the heated section of the wall which can be seen in Fig. 8.47. The last two figures, Fig. 8.48 and Fig. 8.49, display that there is a fairly close correlation of the area averaged quantities of bubble departure frequency and bubble departure diameter at the heated section of wall between the results from the two solvers; however, there is still a significant devation in the results. The causes of the

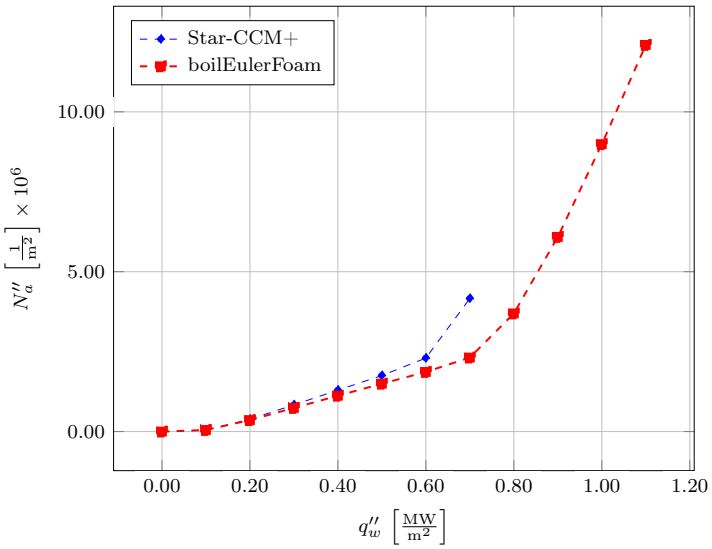

Figure 8.47 MIT Experiments - MIT03 Area Averaged Nucleation Site Density vs Power at Heated Section

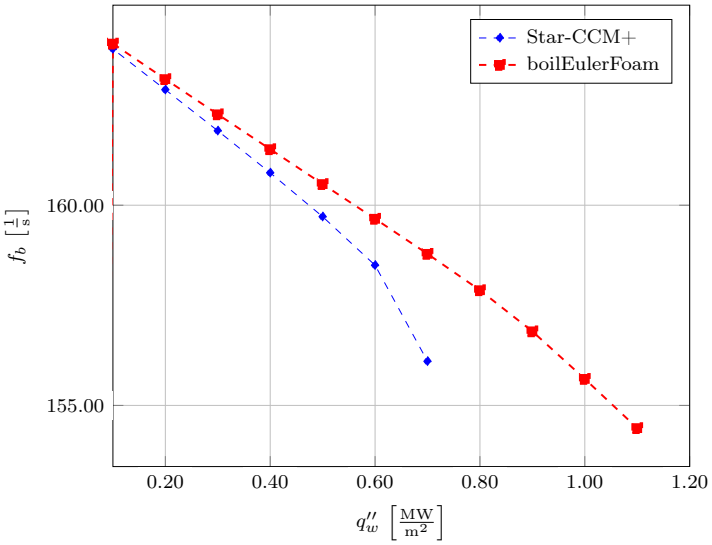

Figure 8.48 MIT Experiments - MIT03 Area Averaged Bubble Departure Frequency vs Power at Heated Section

deviations in the results is very difficult to determine. The complexity of the number of closure models, the lack of information on the specific implementations of Star-CCM+'s closure modeling, a potential miscommunication between MIT's group members and our own, and the difficulty in recognizing quasi-stable un-physical numerical solutions are all

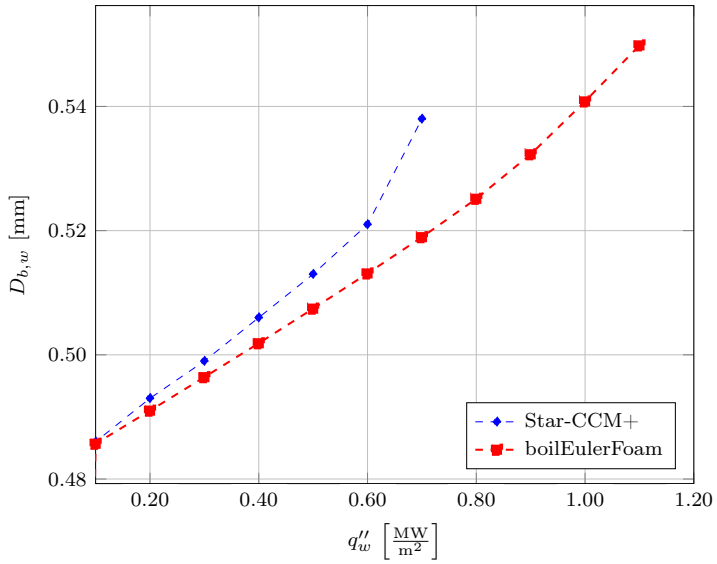

Figure 8.49 MIT Experiments - MIT03 Area Averaged Bubble Departure Diameter vs Power at Heated Section

potential sources of error. The investigation into the performance of our solver still needs significant further investigation.

Chapter 9

CONCLUSIONS

So to summarize some of the challenges we have addressed successfully and some we have yet to address. The finalized design of the modular testing platform and the user-definable functionality works correctly. It was developed so that it is easy to implement with some basic knowledge of C++. The use of the testing platform has allowed the implementation of some improvements in the numerical method. One such improvement being the removal of the checker-boarding that occurs on coarse grids with large gradients (near-wall peaked) void fraction distributions by adding the Turbulence Dispersion & Lift interfacial momentum terms into the PISO Algorithm (pressure equation solution) and by implementing a Rhie-Chow like treatment of lift force. Another such improvement is that it allowed the improvement of the energy equation performance in the Air-to-water Shock-tube test case by the tweaking of the formulation of pressure work term to better capture temperature changes due to changes in density and pressure.

We still have yet to address issues with grid dependence of boiling situations due to the presence of the volumetric source terms, the fact that we can get fairly stable results but it generally requires a very conservative setup that sacrifices efficiency and we have yet to tackle problems with complex geometry such as fuel bundles. In terms of the current performance of the solver, it performs well on most academic and adiabatic numerical test cases and comparisons with Star-CCM+ show good agreement. Boiling numerical test cases can perform well in comparison to both experimental results and Star-CCM+; however, they do not agree consistently. The difficulty in finding the reasons they do not agree are that Star-CCM+ is a “black box” and it is difficult to find out actual implemented forms for the equations, models, forces, etc. and whether or not there are some built-in

"fixes" that happen for various reasons in the code. Also, the complexity and non-linear coupled nature of the problem makes it difficult to ascertain the origin of the differences.

Avenues for future work involving the testing platform could involve adding the ability for the user to adjust the solution algorithm ordering or functionality. The big potential is boilEulerFoam's readiness to perform preliminary DNB simulations and start the process of resolving any issues that are shown to crop up.

BIBLIOGRAPHY

[1] al., Q. W. et. "One-group interfacial area transport in vertical bubbly flow". *International Journal of Heat and Mass Transfer* **45**.8-9 (1998), pp. 1103–1112.

[2] al., R. W. et. "Shapes of liquid drops moving in liquid media". *AIChE Journal* **12** (1966), pp. 854–862.

[3] al., Y. T. et. "Modeling flow pattern transitions for steady upward gas-liquid flow in vertical tubes". *AIChE Journal* **26**.3 (1980), pp. 345–354.

[4] Alali, A. "Development and Validation of a new solver based on the interfacial area transport equation for the numerical simulation of sub-cooled boiling with OpenFOAM CFD Code for Nuclear Safety Applications". PhD thesis. Technische Universität München, 2014.

[5] Anglart, H. *Thermal-hydraulics in nuclear systems*. 2011.

[6] *ANSYS CFX-Solver Theory Guide*. 12.1. Inc. ANSYS. 2009.

[7] Antal, S. P. et al. "Analysis of phase distribution in fully developed laminar bubble two-phase flow". *Int. J. Multiphase Flow* **7**.635 (1991).

[8] Bartolomej, C. & Chanturiya, V. "Experimental study of true void fraction when subcooled water in vertical tubes". *Thermal Engng.* **14** (1967), pp. 123–128.

[9] Bertodano, M. L. de. "Turbulent bubble two-phase flow in a triangular duct". PhD thesis. Rensselaer Polytechnic Institute, Troy, NY, 1992.

[10] Ceumern-Lindenstjerna, W. "Bubble departure diameter and release frequencies during nucleate pool boiling of water and aqueous nacl solutions". *Heat Transfer in Boiling*. 1977.

[11] Chen, Y. & Mayinger, F. "Measurement of heat transfer at the phase interface of condensing bubbles," *International Journal of Multiphase Flow* **18**.6 (1992), pp. 877–890.

[12] Cole, R. "A Photographic Study of Pool Boiling in the Region of the Critical Heat Flux". *AIChE J.* **6** (1960), pp. 533–542.

[13] Degha, A. & Chaker, A. "Numerical study of subcooled boiling in vertical tubes using Relap5 / Mod 3.2". *Journal of Electron Devices* **7** (2010), pp. 240–245.

[14] Delvalle, M. & Kenning, D. “Subcooled flow boiling at high heat flux”. *International Journal of Heat and Mass Transfer* **28** (1985), pp. 1907–1920.

[15] Egorov, Y. & Menter, F. *Experimental implementation of the RPI wall boiling model in CFX-5.6*. Tech. rep. ANSYS, 2004.

[16] Enwald, H. et al. “Eulerian two-phase flow theory applied to fluidization”. *Int. J. of Multiphase Flow* **22** (1996), pp. 21–66.

[17] Ergun, S. “Fluid flow through packed columns”. *Chem. Engng. Progr.* **48** (1952), pp. 89–94.

[18] Frank, T. “Advances in computational fluid dynamics (CFD) of 3-dimensional gas-liquid multiphase flows”. *In NAFEMS Seminar "Simulation of Complex Flows (CFD)"*. Wiesbaden, Germany, 2005, page 1.

[19] Fu, K. *Implementation and validation of two-phase boiling flow models in OpenFOAM*. Tech. rep. KTH, 2012.

[20] Garside, J. & Al-Dibouni, M. R. “Velocity-voidage relationships for fluidization and sedimentation”. *I & EC Proc. Des. Dev.* **16** (1977), pp. 206–214.

[21] Ghione, A. “Development and Validation of a two-phase CFD model using OpenFOAM”. MA thesis. Royal Institute of Technology, Stockholm, Sweden, 2012.

[22] Gibilaro, L. G. et al. “Generalized friction factor and drag coefficient for fluid particle interactions”. *Chem. Engng. Sci.* **40** (1985), pp. 1817–1823.

[23] Gidaspow, D. “Hydrodynamics of fluidization and heat transfer: supercomputer modeling”. *Appl. Mech. Rev.* **Rev 39** (1986), pp. 1–22.

[24] Gilman, L. A. “Development of a General Purpose Subgrid Wall Boiling Model from Improved Physical Understanding for Use in Computational Fluid Dynamics”. PhD thesis. Massachusetts Institue of Technology, 2014.

[25] Gosman, A. D. et al. “Multidimensional modeling of turbulent two-phase flow in stirred vessels”. *AIChE J.* **38**.1946 (1992).

[26] Hawkes, J. “The simulation and study of conditions leading to axial offset anomaly in pressurized water reactors”. MA thesis. Georgia Institute of Technology, 2004.

[27] Hibiki, T. & Ishii, M. “Development of one-group interfacial area transport equation in bubbly flow systems”. *Int. J. Heat Mass Transfer* **45**.2351 (2002).

[28] Hibiki, T. & Ishii, M. “Active nucleation site density in boiling systems”. *International Journal of Heat and Mass Transfer* **46**.14 (2003), pp. 2587–2601.

[29] Hosokawa, S. et al. “Lateral migration of single bubbles due to the prescence of wall”. *ASME Conference Proceedings* **2002**.36150 (2002).

[30] Ishii, M. & Zuber, N. “Drag coefficient and relative velocity in bubbly, droplet, or particulate flows”. *AIChE J.* **25**.843 (1979).

[31] Kader, B. “Temperature and concentration profiles in fully turbulent boundary layers”. *International Journal of Heat and Mass Transfer* **24** (1981), pp. 1541–1544.

[32] Kolev, N. “How accurately can we predict nucleate boiling?” *Experimental Thermal and Fluid Science* **10**.3 (1995), pp. 370–378.

[33] Krepper, E. & Rzehak, R. “CFD for subcooled flow boiling : Simulation of DEBORA experiments”. *Nuclear Eng. Des.* **241** (2011), pp. 3851–3866.

[34] Krepper, E. et al. “CFD modelling of subcooled boiling - concept, validation and application to fuel assembly design”. *Nucl. Eng. and Design* **237**.7 (2007), pp. 716–731.

[35] Kurul, N. & Podowski, M. “On the modeling of multidimensional effects in boiling channels”. *Proceedings of 27th National Heat Transfer Conference*. 1991.

[36] Lemmert, M. & Chawla, J. “Influence of flow velocity on surface boiling heat transfer coefficient”. *Heat Transfer in Boiling*. 1977, pp. 237–247.

[37] Leung, W.-H. “Modeling of Interfacial area concentration and interfacial momentum transfer : Theoretical and Experimental Study”. PhD thesis. Purdue University, 1997.

[38] Limited, O. *OpenFOAM Programmers Guide*. 2017.

[39] Limited, O. *OpenFOAM User Guide*. 2017.

[40] Lucas, D. & Tomiyama, A. “On the role of the lateral lift force in poly-dispersed bubble flows”. *International Journal of Multiphase Flow* (2011).

[41] Michta, E. “Modeling of Subcooled Nucleate Boiling with OpenFOAM”. MA thesis. Royal Institute of Technology, Stockholm, Sweden, 2011.

[42] Mikic, B. & Rohsenow, W. “A new correlation of pool-boiling data including the fact of heating surface characteristics”. *ASME Journal of Heat Transfer* **91** (1969), pp. 245–250.

[43] Nguyen, V. et al. “Modeling of bubble coalescence and break-up considering turbulent suppression phenomena in bubbly two-phase flow”. *Chemical Engineering Science* **54** (2013), pp. 31–42.

[44] Pope, S. *Turbulent Flows*. Cambridge Press, 2010.

[45] Prasser, H. et al. “Development of co-current air-water flow in vertical pipe”. *Int. J. Multiphase Flow* **31** (2005), pp. 1304–1328.

[46] Ransom, V. *Summary of research on numerical methods for two-fluid modeling of two-phase flow*. Tech. rep. V. H. Ransom Consulting and Information Systems Laboratories, 2000.

[47] Ranz, W. E. & Jr., W. R. M. “Evaporation from Drops, Part 2”. *Chem. Eng. Prog.* **48**.4 (1952), pp. 173–180.

[48] Ranz, W. E. & Jr., W. R. M. “Evaporation from Drops, Part I”. *Chem. Eng. Prog.* **48**.3 (1952), pp. 141–146.

[49] Rusche, H. “Computational Fluid Dynamics of dispersed two-phase flows at high phase fractions”. PhD thesis. Imperial College, London, England, 2002.

[50] Rzehak, R. et al. “Comparitive Study of wall force models for the simulation of bubble flows”. *Nuclear Engineering and Design* (2012).

[51] Sato, Y. & Sekoguchi, K. “Liquid velocity distribution in two-phase bubble flow”. *Int. J. Multiphase Flow* **2**.79 (1975).

[52] Schiller, L. & Naumann, Z. “A drag coefficient correlation”. *Z. Ver. Deutsch. Ing.* **77**.318 (1935).

[53] Syamlal, M. & O’Brien, T. J. “Simulation of granular layer inversion in liquid fluidized beds”. *J. Multiphase flows* **14** (1988), pp. 473–481.

[54] Syamlal, M. & O'Brien, T. J. "Computer simulation of bubbles in fluidized bed". *AIChE Symp.* **85** (1989), pp. 21–31.

[55] Syamlal, M. & O'Brien, T. J. "Particle cluster effects in the numerical simulation of a circulating fluidized bed". *4th Int. Conf. on CFB*. Pre-print Volume. Somerset, USA, 1993, pp. 430–435.

[56] Syamlal, M. et al. *MFIX documentation Theory Guide*. Technical Note DOE/METC-94/1004. Morgantown, West Virginia, USA, 1993.

[57] *The favre averaged Drag Model for Turbulent Dispersion in Eulerian Multi-phase flows*. 2004.

[58] Tolubinsky, V. & Kostanchuk, D. "Vapor bubble growth rate and heat transfer intensity at subcooled water boiling". *In 4th International Heat Transfer Conference*. 1970.

[59] Tomiyama, A. "Struggle with computational bubble dynamics". *In Third International Conference on Multiphase Flow* **18** (1998).

[60] Tomiyama, A. et al. "Drag coefficients of single bubble under normal and micro gravity conditions". *JSME International Journal, Series B* **42** (1998), pp. 472–479.

[61] Tomiyama, A. et al. "Transverse migration of single bubbles in simple shear flows". *Chemical Engineering Science* **57**.11 (2002), pp. 1849–1858.

[62] Valle, J. M. D. *Micrometrics*. Pitman, London, 1948.

[63] Wang, X. "Simulations of two-phase flows using interfacial area transport equation". PhD thesis. Ohio State University, 2010.

[64] Weller, H. *Derivation, Modelling and Solution of Conditionally Averaged Two-phase flow equations.* Tech. rep. OpenCFD, 2005.

[65] Wen, C. Y. & Yu, Y. H. "Mechanics of fluidization". *Chemical Engineering Process Symposium Series* **62**.100 (1966).

[66] Wolfert, K. "Non-equilibrium mass transfer between liquid and vapor phases during depressurization processes in transient two-phase flow". *2nd CSNI Specialists meeting*. Vol. 2. 1978, pp. 1377–1387.

[67] Yao, W. & Morel, C. “Volumetric interfacial area prediction in upwards bubbly two-phase flow”. *International Journal of Heat and Mass Transfer* **47** (2004), pp. 307–328.

APPENDIX

Appendix A

OpenFOAM Spatial & Temporal Discretization

This appendix contains the input files for OpenFOAM that dictate the spatial and temporal discretization used for all runs of our solver.

A.1 fvSchemes

```
/*--------------------------------*- C++ -*----------------------*\
| =========                 |                                     |
| \\      /  F ield         | OpenFOAM: The Open Source CFD Toolbox |
|  \\    /   O peration     | Version:  2.2.0                     |
|   \\  /    A nd           | Web:      www.OpenFOAM.org          |
|    \\/     M anipulation  |                                     |
\*---------------------------------------------------------------*/
FoamFile
{
    version     2.0;
    format      ascii;
    class       dictionary;
    location    "system";
    object      fvSchemes;
}
```

```
// * * * * * * * * * * * * * * * * * * * * * * * * * * * * * * * * * * * * //

ddtSchemes
{
    default Euler;
}

gradSchemes
{
    default Gauss linear;
}

divSchemes
{
    default none;

    /*-------------------- Continuity Equations -------------------*/
    div(phi,alpha1)  Gauss vanLeer;
    div(phir,alpha1) Gauss vanLeer;

    div(phi,alpha2)  Gauss vanLeer;
    div(phir,alpha2) Gauss vanLeer;

    /*------------------------ IAC Equation ------------------------*/
    div(phi1,Ai1)      Gauss limitedLinear 1;
    div(alphaPhi1,Ai1) Gauss limitedLinear 1;

    /*--------------------- k-Epsilon Equations --------------------*/
    div(alphaPhi2,k2)       Gauss limitedLinear 1;
    div(alphaPhi2,epsilon2) Gauss limitedLinear 1;

    /*---------------------- Momentum Equations --------------------*/
    div(phi1,U1) Gauss limitedLinearV 1;
```

```
    div(phi2,U2) Gauss limitedLinearV 1;

    div((alpha1*Rc1)) Gauss linear;
    div((alpha2*Rc2)) Gauss linear;

    div(alphaPhi1,U1) Gauss limitedLinearV 1;
    div(alphaPhi2,U2) Gauss limitedLinearV 1;

    /*---------------------- Pressure Equations --------------------*/
    div(phi,rho)   Gauss vanLeer;
    div(phi1,rho1) Gauss vanLeer;
    div(phi2,rho2) Gauss vanLeer;

    div(phid1,p) Gauss upwind;
    div(phid2,p) Gauss upwind;

    /*----------------------- Energy Equations ---------------------*/
    div(alphaPhi1,h1) Gauss limitedLinear 1;
    div(alphaPhi2,h2) Gauss limitedLinear 1;

    div(alphaPhi1,ke1) Gauss limitedLinear 1;
    div(alphaPhi2,ke2) Gauss limitedLinear 1;

    div(alphaPhi1,p) Gauss upwind;
    div(alphaPhi2,p) Gauss upwind;

}

laplacianSchemes
{
    default  none;

    /*--------------------- k-Epsilon Equations --------------------*/
```

```
    laplacian(DepsilonEff2,epsilon2) Gauss linear corrected;
    laplacian(DkEff2,k2)             Gauss linear corrected;

    /*---------------------- Momentum Equations --------------------*/
    laplacian((alpha1*nuEff1),U1) Gauss linear corrected;
    laplacian((alpha2*nuEff2),U2) Gauss linear corrected;

    /*---------------------- Pressure Equations --------------------*/
    laplacian(Dp,p) Gauss linear corrected;

    /*----------------------- Energy Equations ---------------------*/
    laplacian(qEff1,h1) Gauss linear corrected;
    laplacian(qEff2,h2) Gauss linear corrected;
}

interpolationSchemes
{
    default linear;
}

snGradSchemes
{
    default corrected;
}

fluxRequired
{
    default no;
    p;
    alpha1;
    alpha2;
}
```

```
// ********************************************************** //
```